

# **Acoustic and phononic metamaterials for surface waves**

Submitted by Vasiliki (Vicky) Kyrimi to the University of Exeter  
as a thesis for the degree of  
Doctor of Philosophy in Physics/Engineering (CDT)  
In February 2021

This thesis is available for Library use on the understanding that it is  
copyright material and that no quotation from the thesis may be  
published without proper acknowledgement.

I certify that all material in this thesis which is not my own work has  
been identified and that no material has previously been submitted  
and approved for the award of a degree by this or any other  
University.

**Signature:**

A handwritten signature in black ink, appearing to read 'V. Kyrimi', written in a cursive style.

## Abstract

The research in this work is along two main themes. The first involves the generation of acoustic surface waves in aluminium plates with lattices of periodic sub-wavelength perforations, the experimental characterisation of the bound modes supported by the honeycomb and hexagonal lattices, and the verification of results through numerical modelling. The energy is driven into the system via a point source positioned over a hole in the centre of the sample and a needle-tip probe microphone positioned on the opposite side of the sample measures local pressure field. The full band-structure of bound modes is obtained via Fourier transformations of the acoustic signal in time and space, and agrees well with the numerically obtained dispersion relations, with one exception; for the honeycomb sample the upper branch of the Dirac cone in the  $\Gamma$ - $K$  direction is present in the model, but is not observed experimentally in the first Brillouin zone. Conversely, the existence of the upper branch is shown in the  $M$ - $K$  direction for the honeycomb sample. Although losses increase monotonically as the mode travels through the  $K$  point at the Dirac frequency on the honeycomb lattice we have been able to measure pressure fields at distance 116 mm from the source.

The second theme studied in this work involves using periodic arrays of spiral resonators to produce bandgaps for Rayleigh surface acoustic waves propagating on a piezoelectric substrate, lithium niobate, which is a solid crystal. In this numerical study, the surface acoustic wave source is an interdigital transducer and the frequency of the generated Rayleigh wave is dependent on the distance between the transducer's metallic fingers. Dispersion relations and transmission spectrums were obtained using the COMSOL® eigenfrequency and frequency domain models respectively. Dispersion relationships for arrays of such resonators showed that they can be used to produce bandgaps for Rayleigh waves, but at lower frequencies than those achieved for other phononic crystals with the same unit cell size. In addition, negative slopes in the dispersion curve of the spiral structure indicate that a square array of spiral resonators, supports negative group velocity SAW modes. Transmission analysis has shown that the bandgap attenuation is large (~25 dB) at both high and low frequencies and displacement field profiles highlight confinement of the acoustic energy throughout the height of the oscillators. Considering the small size of the proposed device and the aforementioned propagation characteristics, we stress that the spiral metamaterial shows very good potential for sound manipulation and filtering in a plethora of lab-on-chip applications.



# *Acknowledgements*

This research was conducted thanks to funding by EPSRC Centre for Doctoral Training in Metamaterials Grant No. EP/L015331/1. Completing this thesis was not an easy journey. The journey started on 2015, was stopped on winter 2017 and restarted on the spring of 2018; *it restarted thanks to the following academics to whom I would like to express my deepest acknowledgements.*

Prof. Gino Hrkac, you have been such an exemplary mentor, thank you for the time you have put into helping me to deal with the academic letters..The fact that academics like you, who try to make things operate in a better way, exist, truly inspired me.

Prof. Peter Vukusic, thank you for making the decision to extend my scholarship and for giving me the opportunity to continue my research under the supervision of Prof. Geoff Nash and Dr Ana Neves.

Prof. Geoff Nash, thank you for your guidance and support over the past 3 years. It was such a pleasure working with you. Except for sharing your knowledge, problem solving strategies, and experience with me, you have taught me how to think out of the box which has sped up my research. You have always had good answers for every question I asked, *and I will never forget your kindness.* You are the greatest role model and I learned so many remarkable qualities from observing how you conduct research, how you keep encouraging all your students and make them willing to strive to fulfil their true potential. I have also observed that people working with you seem so happy, which is a leadership skill I look up to.

Dr Ana Neves, thank you for accepting to be my second supervisor. Your excellent advice whenever I asked for it and the conversations we had when I was indecisive about which career path to follow, have brought to my attention so many valuable points that I would never have thought about. I feel so lucky to have met you and I am so grateful for your guidance.

Next, I would like to thank my colleagues for creating such a lovely working atmosphere.

Yulia Dautova, thank you for all the times you have helped me and motivated me and for the mind-blowing conversations about Dirac points! Your enthusiasm when you were explaining your thoughts and ideas to me, your sense of humour and kind-heartedness made me look forward to coming to the office. I also feel lucky to have met your wonderful family.

Natalie Whitehead, thank you for being you! You have been such a friendly face in the office. I was always amazed on how you managed to accomplish successfully all PhD related tasks, do outreach activities, maintain a lovely garden, have lots of hobbies and interests, is there anything you can't do? Not only you are a curious, creative mind but you are such an empathetic person. I could write many pages on how much you have helped me every time I was in a perplexing situation, thank you for your friendship. I am sure you know my doors are always open for you anytime you decide to visit Greece.

Martha Vardaki, I feel so lucky that I have met you in the first year of my PhD in Exeter. You are a one-of-a-kind, kind of person. Wishing you a lot of success in whatever you do.

Prarthana Gowda, thank you for everything you did for me, you are younger than me but you always provided sage advice, you are such a wise person and we have had great fun. I felt like I was travelling to India through your stories and through the amazing food you cooked.

My compatriots, Ioannis Leontis and Konstantinos Anastasiou, thank you for being around in the office in Physics building. Your good sense of humour restored days of stress.

Caroline Pouya, Cheng Chi, Jess Brown and Milli Owens thank you for welcoming me in the office in Harrison building. I really enjoyed chatting with you in the tea (or ice cream) breaks.

Huanling Zou, you have spread so many colour around my life. Countless times, you have proved that friendship goes beyond words and encompasses actions. Thank you, my dear friend.

Ben Ash, thank you for making your point with clarity, each time I asked you to explain difficult concepts and for sharing your ideas with me.

Gareth Ward and Joseph Beadle, thank you for helping me to set up my first experiments and for trying to answer the same question over and over. It took me some time to get used to your Welsh and British accents and I really appreciate your kindness.

Tim Starkey, thank you for your editing work on my first draft manuscript.

Next, I would like to thank Prof. Sir Roy Sambles, for visiting me both in the acoustics laboratory and in the office and giving me advice when I faced difficulties with either the experiment or the simulations.

Sophia Athanasopoulou, physicist and graphics designer, thank you for your 18 years of friendship and for the splendid graphics you created for page 11 of this Thesis. I admire you

for the fact that you have obtained a second degree and I know that you are a wonderful mother, so your success is even more important. Thank you for letting me blow my steam off each time I called you and was in bad mood. Your advice has been invaluable.

My sister Konstantina, I have missed you so much from my life and I know you have missed me from your life too. I brag about you all the time and I wish I was able to visit you more often whilst I was living in the UK. Thank you for making my life brighter, you are such a great sister!

Finally, I would like to thank my parents who gave the world to me and the freedom to explore it. Thank you for being proud of me. Mother, thank you for putting your professional career behind, in order to bring me up and help me develop such a personality, so that it never crossed my mind to quit my PhD journey. Thank you for making me believe that any difficulties I face can be overcome. I will always be grateful.

Μητέρα, σε ευχαριστώ που έβαλες την ανατροφή μου πάνω από την επαγγελματική σου καριέρα και με βοήθησες να εξελίξω την προσωπικότητά μου, έτσι ώστε όταν αντιμετώπιζα δυσκολίες, δεν πέρασε ούτε από την άκρη του μυαλού μου η σκέψη να σταματήσω την έρευνα στα πλαίσια του διδακτορικού. Θα είμαι πάντα ευγνώμων.

# Contents

<b>Title page</b> .....	1
<b>Abstract</b> .....	2
<b>Aknowledgements</b> .....	4
<b>Contents</b> .....	7
<b>Chapter 1 Introduction</b> .....	13
<b>Chapter 2 Surface Acoustic Waves (SAWs) - Sound in solids</b> .....	17
<b>2.1 Introduction</b> .....	17
<b>2.2 Substrate and source for Rayleigh SAW wave excitation</b> .....	17
2.2.1 Rayleigh SAW wave.....	17
2.2.2 Piezoelectricity.....	18
2.2.3 Lithium niobate (LiNbO <sub>3</sub> ).....	19
2.2.4 Interdigital transducer (IDT).....	22
2.2.4.1 Rayleigh SAW grating.....	25
2.2.4.2 Excitation signal and response.....	27
<b>2.3 Surface wave solutions in a piezoelectric half space</b> .....	29
2.3.1 Elasticity.....	29
2.3.2 Stress.....	29
2.3.3 Strain.....	31
2.3.4 Generalised Hooke's Law for anisotropic materials.....	31
2.3.5 Equations of motion for bulk elastic waves in anisotropic, non-piezoelectric materials--.....	32
2.3.6 Equations of motion for bulk elastic waves in anisotropic, piezoelectric materials and electroelastic coupling.....	34
2.3.7 The form of solution and the boundary conditions for a piezoelectric half-space.....	35
2.3.8 The system ordinary differential equation and the system matrix.....	37
<b>2.4 Conclusions</b> .....	39
<b>Chapter 3 Acoustic surface waves (ASWs) - Sound in air</b> .....	41
<b>3.1 Introduction</b> .....	41
<b>3.2 Sound generation in air</b> .....	41
<b>3.3 Sound propagation through an unbound gas</b> .....	43

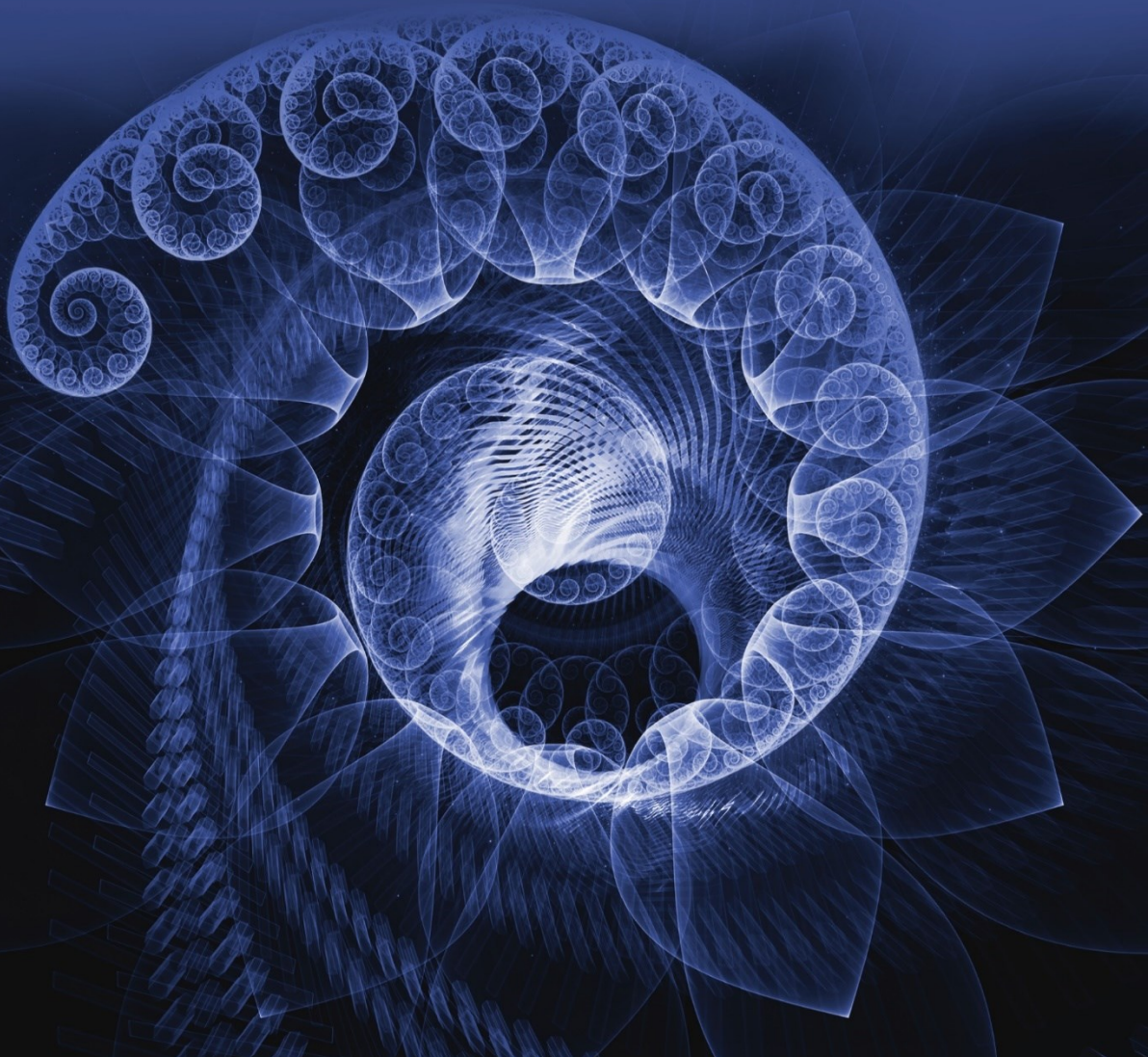
3.3.1 Equation of state for an ideal gas.....	44
3.3.2 Conservation of mass – Continuity equation.....	44
3.3.3 Conservation of momentum.....	45
3.3.4 The acoustic wave equation.....	46
<b>3.4 Sound propagation through a rigid-walled bound gas -Thermoviscous loss effects.....</b>	<b>48</b>
<b>3.5 Sound propagation through a rigid walled cylindrical pipe.....</b>	<b>54</b>
3.5.1 End effects and cut-off frequency.....	57
3.5.2 Reflection coefficient.....	61
<b>3.6 Conclusions.....</b>	<b>62</b>
<b>Chapter 4. Simulations and modelling methods.....</b>	<b>64</b>
<b>4.1 Introduction.....</b>	<b>64</b>
<b>4.2 Discretization.....</b>	<b>64</b>
<b>4.3 The Finite Element Method from the Weak Formulation: Basis Functions and Test Functions.....</b>	<b>66</b>
4.3.1 System matrix and meshing.....	66
<b>4.4 COMSOL®-Module and solver selection.....</b>	<b>71</b>
<b>4.5 Study selection – Frequency domain.....</b>	<b>71</b>
4.5.1 The geometry of model simulating SAW device.....	71
4.5.2 Perfectly matched layers.....	72
4.5.3 Multiphysics settings.....	73
4.5.4 Mesh settings.....	74
<b>4.6 Study selection – Time domain.....</b>	<b>75</b>
<b>4.7 Study selection – Eigenfrequency model for sound in solid.....</b>	<b>75</b>
4.7.1 Mesh settings.....	78
<b>4.8 Study selection – Eigenfrequency model for sound in air.....</b>	<b>79</b>
4.8.1 The geometry of model simulating ASW device.....	79
4.8.2 Multiphysics settings.....	80
4.8.3 Mesh settings.....	80
<b>4.9 Conclusions.....</b>	<b>81</b>
<b>4.10 Appendix.....</b>	<b>81</b>
<b>Chapter 5. ASW and SAW dispersion relations.....</b>	<b>84</b>
<b>5.1 Introduction.....</b>	<b>84</b>
<b>5.2 Acoustic Surface Wave dispersion relation.....</b>	<b>85</b>

5.3 Dirac-cone dispersion relations for Acoustic Surface Waves.....	90
5.4 Applications of Dirac materials.....	97
5.5 Surface Acoustic Wave dispersion relation.....	99
5.6 Dispersion relations for Rayleigh Waves on meta-surfaces.....	101
5.7 SAW applications.....	105
5.8 Conclusions.....	106
<b>Chapter 6. Experimental characterisation and numerical investigation of the bound ASWs supported by honeycomb and hexagonal hole arrays.....</b>	<b>108</b>
6.1 Introduction.....	108
6.2 Honeycomb and hexagonal arrays.....	109
6.3 Experimental set up.....	110
6.4 Signal processing and data analysis techniques.....	111
6.4.1 Overview.....	111
6.4.2 Temporal Fourier analysis-2D pressure field maps.....	114
6.4.3 Spatial Fourier analysis- Full dispersion relation.....	115
6.4.4 Experimental data analysis- Curve fitting.....	119
6.5 Simulation Results.....	120
6.6 Experimental results.....	121
6.7 Conclusions.....	129
<b>Chapter 7. Numerical investigation of metasurfaces comprising spiral shaped local resonators for SAWs.....</b>	<b>131</b>
7.1 Introduction.....	131
7.2 Bragg gaps and locally resonant band gaps.....	132
7.3 Void wall geometry.....	132
7.4 Dispersion analysis.....	134
7.5 Transmission analysis.....	137
7.6 Dispersion/Transmission comparison.....	139
7.7 Negative group velocity.....	140
7.8 Conclusions.....	142
<b>Chapter 8 Conclusions and future directions.....</b>	<b>143</b>
8.1 Six-fold Symmetric Acoustic Surface Wave Metasurface.....	143
8.2 Novel Spiral Annular Hole Elastic Wave Metasurface.....	145
8.3 Outlook.....	148
<b>References.....</b>	<b>149</b>



Mathematical analysis is as extensive as nature itself; it defines all perceptible relations, measures times, spaces, forces, temperatures; this difficult science is formed slowly, but it preserves every principle which it has once acquired; it grows and strengthens itself incessantly in the midst of the many variations and errors of the human mind. Its chief attribute is clearness; it has no marks to express confused notations. It brings together phenomena the most diverse, and discovers the hidden analogies which unite them.

Joseph Fourier (1822)



*To those who serve science mostly  
for the sake of benefiting society...*

# CHAPTER 1

## Introduction

In the present thesis wave-system interactions are investigated. The waves explored can be separated into two types, based in the medium in which they propagate. Acoustic surface wave (ASW) is the type of wave propagating in air and surface acoustic wave (SAW) is the type of wave travelling in a solid. The system interacting with these waves is a metasurface; an array of resonators with constant distance between them which will be referred to as the lattice constant. For the metasurfaces supporting ASWs the lattice constant is fixed to  $\alpha = 8.66$  mm, whereas for the metasurfaces supporting SAWs the lattice constant is fixed to  $\alpha = 10.9$   $\mu\text{m}$ . The interaction of a square configuration of spiral resonators with Rayleigh SAWs has been computationally investigated and a hexagonal as well as a more complicated honeycomb arrangement of holes has been excited by a point source resulting in ASW generation. The ASW metasurfaces have been investigated by both experimental and computational means.

It is worth mentioning that metasurfaces are composite materials. They do not exist in nature and they are mostly known for their negative refraction, curved lens and optical resolution properties. The negative refraction was firstly hypothesized by Victor Veselago in his first paper "*The Electrodynamics of Substances with Simultaneously Negative Values of  $\epsilon$  and  $\mu$* " published in 1967 [1], but it was after the creation of a composite metamaterial by David Smith et al. that Veselago realised that that a composite material can be designed to produce any value for permittivity and permeability. Hence, metamaterials broaden the range of material responses found in nature. The fact that Veselago was nominated for Nobel Prize in 2011 highlights the importance of his discovery. Over the years experimental and modelling techniques became more advanced and researchers working on the field of acoustics have taken inspiration from Veselago lens and have found interesting phenomena to realise for sound waves such as acoustic focusing, confinement and cloaking.

Establishing mathematical analogies such that the same equations can be used to solve problems in both electromagnetics and acoustics was the research objective of many of the great scientists of the past who have studied the theory of wave motion. It was proven that the displacement current introduced by Maxwell into the electromagnetic equations is analogous to elastic displacements. Furthermore, the mass density,  $\rho$ , and bulk modulus  $\beta$ , characterizing

metamaterials treated as elastic solids are analogous to electric permittivity  $\epsilon$ , and magnetic permeability  $\mu$ , respectively. Note, that if  $\rho < 0$ , the acoustic metamaterial expands with compression and when  $\beta < 0$ , it accelerated to the left while being pushed to the right. However, neither negative  $\rho$  or  $\beta$  are found in naturally occurring materials since such unique properties, are usually induced from local resonators contained within each unit cell of engineered metasurfaces. Negative values of the effective mass density have been associated with bandgap formation for Lamb waves [2] and more recently for Rayleigh waves [3]. In the latter study the width of the band gap was related to the region of negative effective density of the resonant metamaterial. This phenomenon is intuitive if we consider Newton's second law; if the mass becomes negative, the acceleration would be to the opposite direction of the applied force, and the response to the incoming driving pressure field would be reduced. It may also be intuitive that at the frequency the effective mass approaches infinity, the metamaterial resonates. Hence, many studies use the effective medium approach to unravel the mechanism of bandgap formation in acoustic metamaterials. For an acoustic metamaterial consisting of a thin plate with periodically attached mass-spring resonators, it has been shown that negative effective mass density can be realized by the resonance of either the mass-spring resonator or the plate matrix [4].

In the present study we use the dispersion relation approach and we aim for creating low-frequency bandgaps for SAWs, which we then compare to transmission results. The approach can be summarized as follows. The differential equations describing our system are solved via COMSOL® software which casts the equations into a matrix form and uses the Bloch theorem to derive dispersion relations, which relate wave vectors to frequencies. The outputs are also the displacement fields in x, y and z directions at a single unit cell, which can in turn be multiplied by a phase factor (according to the Bloch theorem) to yield the displacement fields at every spatial point in the metasurface. The displacement field profiles enable the characterization of the modes displayed in the dispersion relations and help us develop our understanding of the interaction between Rayleigh SAWs and the metasurface. The initial hypothesis about the novel resonator shape that will allow strong interaction with the incoming Rayleigh SAW wave, and hence wider bandgap than the previously reported annular hole structure [5], is based on the fact that the interface area between SAW and the novel resonator is much larger than the SAW-annular hole interface. The fact that the annular hole structure outperforms the pillar structure in terms of bandgap extinction further supports this claim. Indeed, it has been demonstrated [5] that 7 pillars are required to match the equivalent

attenuation of 1 annular hole making the SAW device advantageous for applications which require band gaps.

The key assumption is that the incoming Rayleigh SAW interacts with the resonator and excites it. The SAW energy is not dissipated inside the resonator and it is re-emitted to the substrate. In contrast, the metasurfaces supporting ASWs are lossy and hence viscothermal boundary layers are included in the COMSOL® modelling.

As already mentioned, SAW metasurfaces have been employed to induce low frequency band gaps. ASW metasurfaces, on the other hand, have been employed to induce gapless dispersion curves with a pair of linear crossings at the Brillouin zone border. The so called Dirac point is guaranteed by the  $C_{6v}$  and  $C_{3v}$  point group symmetries of the hole configuration of the honeycomb ASW metasurface according to group theory [6]. The first ASW metasurface exhibiting Dirac cones in its dispersion relation was realised by Torrent et al. [7] and the slowness of ASWs at the proximity of the Dirac point as well as the analogy to graphene were highlighted in that study. However, losses at frequency near the Dirac frequency, which might have deleterious consequences to slow sound applications of the acoustic graphene, were not investigated. In the present work, apart from comparing the dispersion relations (frequency vs momentum) between honeycomb and hexagonal lattices, we measure the acoustic pressure fields across these structured surfaces to test the analogy with graphene and we explore losses for both lattices. Dispersion relations are obtained after performing Fourier transformations to the time series experimental data. The resulting three dimensional data cube in the Fourier (or reciprocal) space has a vertical axis corresponding to frequency and is perpendicular to the momentum plane. In other words, the coordinates of each point in the Fourier space are ( $k_x$ ,  $k_y$ , frequency), where  $k_x$  and  $k_y$  is the momentum (wave vector) along x and y directions in the reciprocal space. Note that these directions are different from the x and y directions of the physical (or real) space. Slices (2D surfaces) perpendicular to the momentum plane are referred to as dispersion relation plots whereas slices parallel to the momentum plane are referred to as isofrequency contour plots.

The outline of this thesis is as follows. In Chapter 2, the relevant background theory of bulk elastic wave propagation in anisotropic, piezoelectric materials is highlighted with particular emphasis on describing the properties of lithium niobate ( $\text{LiNbO}_3$ ), the crystal in which SAWs propagate. It is important to understand how the crystal axis is defined because the SAW velocity changes when the crystal axis' orientation changes and this in turn affects the crystal's

piezoelectric coupling to the wave. SAW generation using interdigital transducers (IDTs) is also explained by plotting the displacement of the substrate for different excitation frequencies of the IDT.

The key focus of Chapter 3 is to describe the interaction of sound with a region of air bounded by a rigid-walled cavity and the Navier-Stokes equation is introduced to account for losses. The afore mentioned honeycomb and hexagonal metasurfaces are in fact comprised of rigid-walled cylindrical pipes and losses will be neglected to simplify the description of bound ASW generation on such sculpted surfaces. It is important to understand that ASWs arise from the interference between localized (evanescent) and propagating fields and hence, the concepts of radiation impedance and end effects will be explained.

In Chapter 4 the discretization methods of partial differential equations (describing arbitrary systems) and the settings used in the FEM (finite element modelling) package, COMSOL® [8] are presented. The computational domains of eignfrequency, frequency domain and time domain models are illustrated and discussed.

The main focus of Chapter 5 is to discuss (ASW) and (SAW) dispersion relations in order to understand the circumstances, under which trapped ASWs and hybridized SAWs are formed. To simplify the analysis, one-dimensional (1D) gratings supporting ASWs and SAWs are illustrated and their dispersion relations are compared. The dispersion relation of the previously reported acoustic graphene [7] is presented and it is shown that the structure's wave function is a series over the reciprocal lattice vectors; the latter need to be expressed in a certain form, for the Bloch theorem to be satisfied. The dispersion relation of the previously reported annular hole structure [5] is also introduced.

Motivated by the fascinating physics and the plethora of Dirac material and SAW device applications highlighted in Chapter 5, we i) design and numerically investigate two ASW metasurfaces (honeycomb and hexagonal) and we ii) numerically investigate many different SAW metasurfaces comprised of spiral shaped local resonators. Finally, we present our results in Chapter 6 and Chapter 7. The conclusions and future directions are summarised in Chapter 8.

## **CHAPTER 2**

### **Surface Acoustic Waves (SAWs) - Sound in solids**

#### **2.1 Introduction**

Sound waves in solids can be classified to two main categories, bulk waves and surface waves. Due to their slower rate of decay surface waves can circle the globe many times following a large earthquake. There are two basic types of surface acoustic waves; Rayleigh waves and Love waves. However, only Rayleigh waves propagate along the free of stresses surface of a homogeneous medium, also called as half-space. Love waves, cannot exist in a homogeneous half space as they require a velocity structure which varies with depth. A qualitative description of Rayleigh SAW properties and the basic equations governing the system are given in this chapter. The system is a homogeneous half-space consisting of lithium niobate, which is a piezoelectric material, with the piezoelectricity resulting from anisotropy. Although there are different ways Rayleigh SAWs can be excited, generation using interdigital transducers is described. The reasons for selecting lithium niobate as a substrate and interdigital transducers as an excitation source are explained and the calculated displacement field arising from Rayleigh SAW excitation is shown along different positions on the surface of the medium.

#### **2.2 Substrate and source for Rayleigh SAW wave excitation**

##### **2.2.1 Rayleigh SAW wave**

A surface acoustic wave (SAW) is a type of wave motion which involves changes to the relative positions of atoms in a solid material. These changes are quantitatively described as strains and induce internal forces, which tend to return the material to its equilibrium, unstrained state. The internal forces, often called stresses will cause strains which in turn generate stresses. The stresses generate further strain at more distant points and in this way the disturbance propagates from point to point in the form of acoustic waves which travel over the whole extent of the solid. The disturbance propagation direction can be parallel to atom displacement, normal to

atom displacement or it can form an angle with respect to the local atom displacement that is neither zero nor ninety degrees at some points in time. The latter is the type of wave motion that we will discuss in the present Thesis and the particle trajectory is indicated by arrows in **Figure 2.1** and it is retrograde elliptical at depth close to the surface, because at the top of the orbit, it is opposite to the direction of propagation. The displacement amplitude decays exponentially away from the surface and the motion of the material is in the sagittal plane, hence there are two displacement components  $u_x$  and  $u_z$ , dependent on depth as shown in the right panel of **Figure 2.1**. The existence of this type of wave motion was shown in 1885 by Lord Rayleigh [9], who pointed out that the wave explained some seismological signals not previously understood.

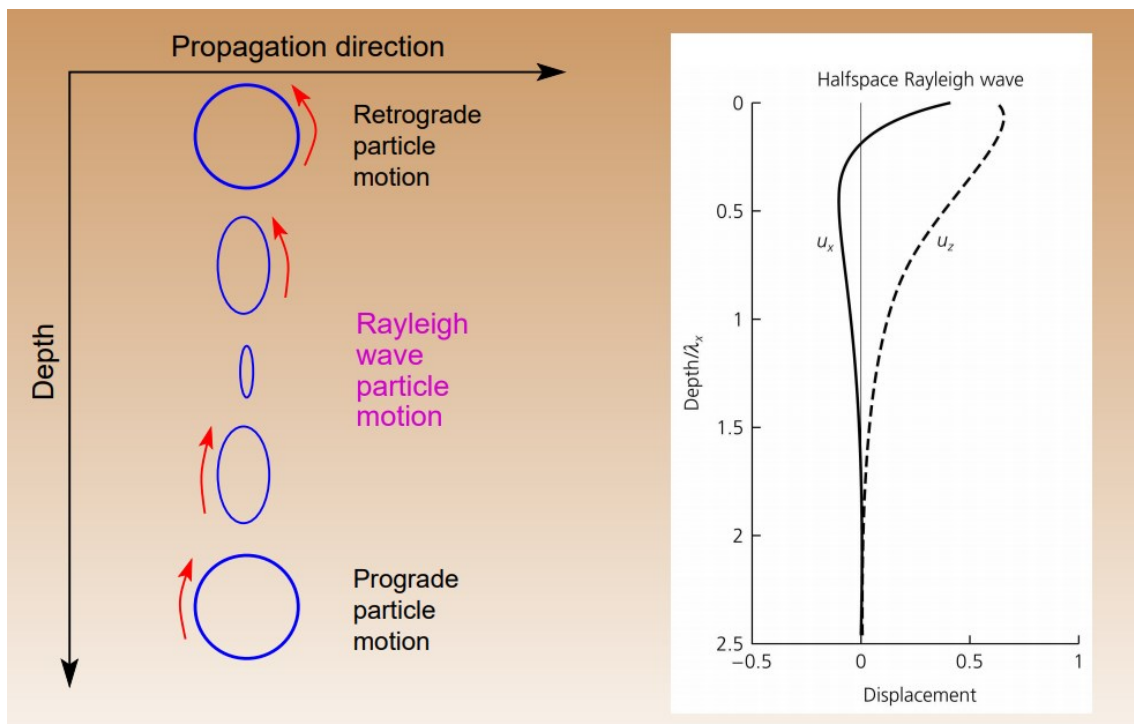


**Figure 2.1** Left panel: Qualitative description of particle motion when a Rayleigh SAW wave propagates in half-space along the direction shown in black arrow. Right panel: Displacement components  $u_x$  and  $u_z$  versus depth normalized by SAW wavelength.

### 2.2.2 Piezoelectricity

The word piezoelectricity means electricity resulting from pressure and it is derived from the Greek word “piezein” which means to squeeze or press, and “ēlektron” which means amber

[10], an ancient source of electric charge. French physicists Jacques and Pierre Curie discovered piezoelectricity in 1880 [11]. The piezoelectric effect is a reversible process, that is, mechanical strain resulting from an applied electric field is also referred to as piezoelectric effect and it is used in this thesis for the production of Rayleigh waves.

The internal structure of a piezoelectric material, lithium niobate, will be discussed in the next section and it will be shown that lithium niobate's internal structure does not have a centre of symmetry. This phenomenon, which is often called anisotropy, favors the generation of elastic waves, which are characterised by particle displacements in more than one direction in space, as it was shown in **Figure 2.1**.

### 2.2.3 Lithium niobate ( $\text{LiNbO}_3$ )

Lithium niobate was first discovered to be ferroelectric in 1949, [12] and the details of its physical properties can be found in [13]. In the ferroelectric phase, the elastic forces of the crystal become dominant and force lithium and niobium atoms into the positions illustrated in **Figure 2.2** The negatively charged oxygen atoms form octahedral cages surrounding lithium or niobium atoms. In this phase the cations are not exactly at the center of the oxygen cages, resulting in a spontaneous polarization, which has the same orientation of the cation's shift. Hence, ferroelectric  $\text{LiNbO}_3$  can be viewed as an intrinsic polar stacking of  $\rightarrow \text{Nb-O}_3\text{-Li}$  [14].

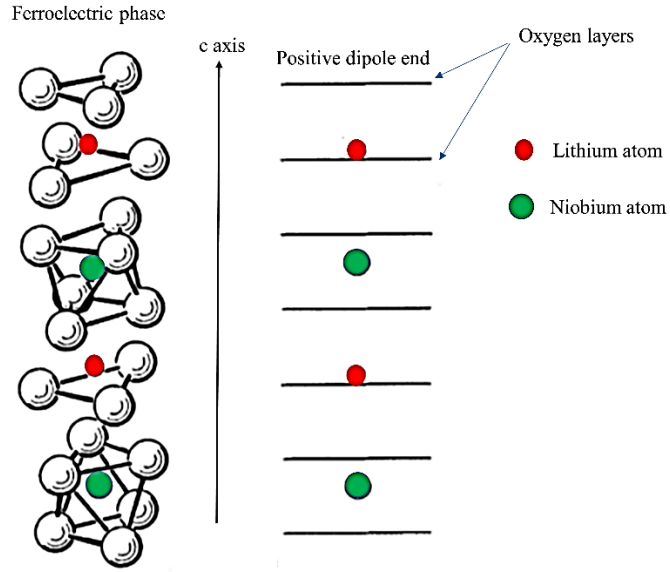


**Figure 2.2** Lithium niobate in the ferroelectric phase. Horizontal lines indicate the positions of the oxygen layers. Lithium and niobium atoms are shown in red and green colors respectively. Modified from [13].

Lithium niobate crystal is a member of the trigonal crystal system as it exhibits three-fold rotation symmetry about its c axis and is described either by a hexagonal, shown in **Figure 2.3** (a) or by a rhombohedral primitive cell. The definition of the crystal axis is of fundamental importance to model and understand anisotropic materials. The standard method of determining the orientation of the +Z principal axis is to compress the crystal in the c axis direction. As a result the net polarization is reduced and the +z face becomes negative. The +Z principal axis is defined as being directed out of the z face that becomes negative upon compression. A cross section of the hexagonal unit cell is shown in **Figure 2.3** (b) where the mirror planes of symmetry are shown in dashed lines. The +X principal axis is chosen to be perpendicular to the mirror plane 2 and the +Y principal axis is chosen such that the system is right handed. It can be observed that the +Y principal axis is parallel to the mirror plane 2. The standard axis orientation is used to describe tensor physical properties in lithium niobate as well as the crystal cut. For example, the notation Y-Z lithium niobate indicates that the surface normal aligns with the crystal Y principal axis and the wave propagates in the crystal Z principal direction. In the present thesis  $128^\circ$  Y-X LiNbO<sub>3</sub> is used, which indicates that the surface normal makes an angle  $128^\circ$  with the crystal Y principal axis. In the case that the surface normal does not make the required angle with the Y principal axis, the crystal cut is

defined using Euler angles, shown in **Figure 2.3** (c). If the principal axes are (X, Y, Z) and the Euler transformed axes are (x,y,z) the desired cut is achieved when  $(\alpha, \beta, \gamma)$  is  $(0, -38^\circ, 0)$ . N is the line of nodes which intersects the planes defined by XY and xy,  $\alpha$  is the angle between the x-axis and the N-axis,  $\beta$  is the angle between the z-axis and the Z-axis and  $\gamma$  is the angle between the N-axis and the X-axis.

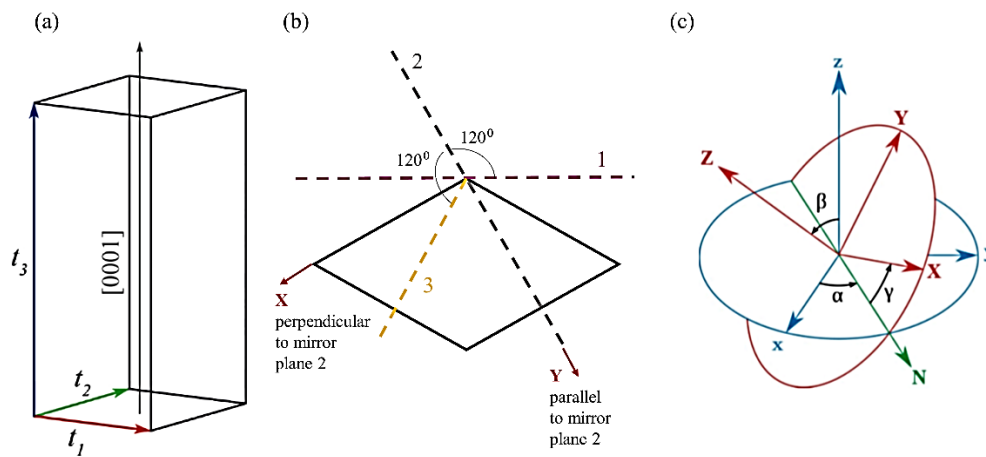


**Figure 2.3** (a) Hexagonal unit cell of ferroelectric LiNbO<sub>3</sub>. The atomic basis is not shown for the sake of clarity. Taken from [14]. (b) Standard convention and a secondary convention for choosing the x and y principal axes within the hexagonal unit cell in LiNbO<sub>3</sub>. (c) Visual representation of an Euler angle transformation. Taken from [15].

It is worth mentioning that when the  $\beta$  angle changes the SAW velocity changes significantly and the lithium niobate's piezoelectric coupling to the wave changes. The piezoelectric coupling,  $K^2$ , is dependent on the fractional difference  $\frac{\Delta v}{v} \equiv \frac{(v_f - v_m)}{v_f} \equiv \frac{K^2}{2}$ , where,  $v_f$ , the SAW velocity for the free surface, and  $v_m$ , the SAW velocity for a metallized surface. Hence, the coupling constant  $K^2$ , is defined as twice the fractional difference. For the metallized surface case a thin metal layer with infinite conductivity is assumed to cover the surface which does not affect the mechanical boundary conditions, but shorts out the in-plane components of the electric field. It is also worth mentioning that when the  $\beta$  angle changes, the SAW velocity for the metallized velocity changes. An illustration of both free and metallized cases SAW velocity versus  $\beta$  angle is shown in **Figure 2.4** (b) for a X cut LiNbO<sub>3</sub>. The orientations of the X, Z, and

–Y principal axes for this cut are shown in **Figure 2.4 (a)**. The dashed line in **Figure 2.4 (b)** indicates that in an angle  $\beta=38^\circ$  the velocity difference between free and metallized case is maximum, implying that the piezoelectric coupling is the strongest possible at this angle.

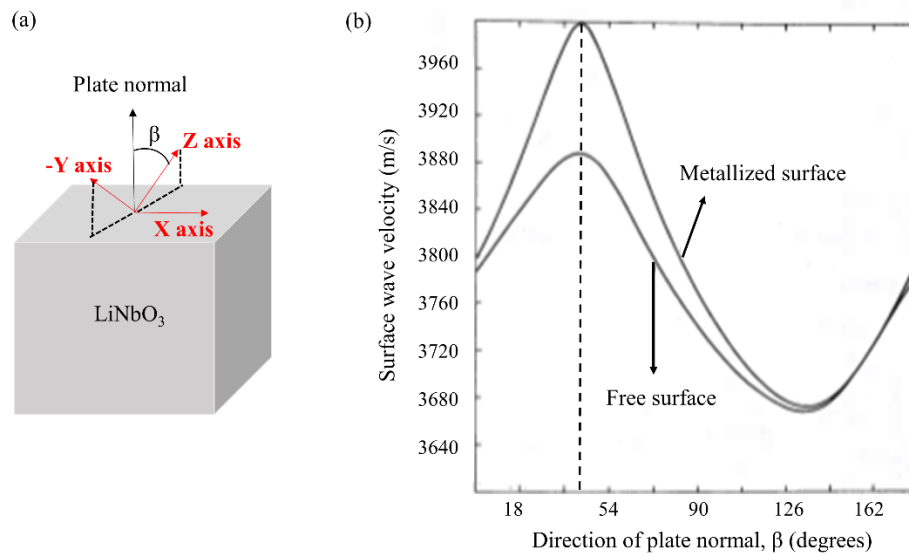


**Figure 2.4 (a)**. Principal axis orientation for a X-cut LiNbO<sub>3</sub>. **(b)** Surface wave velocities for a free and a metallized surface versus angle  $\beta$ . The dashed line guides the eye to the  $\beta=38^\circ$  case, which corresponds to the  $128^\circ$  Y-X cut. Modified from [16].

## 2.2.4 Interdigital transducer (IDT)

In this work, the device which uses a piezoelectric material, as a substrate is an interdigital transducer (IDT). This type of transducer presented direct piezoelectric coupling to surface elastic waves and was invented by White and Voltmer [17] as a source or receiver of surface waves. An interdigital transducer (IDT) comprised of metallic electrodes is used as a means of generating SAWs. The transducer is deposited on the surface of piezoelectric material and the voltage applied to the metallic electrodes triggers material displacement. In the numerical model used in this work, which is described in Chapter 4, 5 metallic fingers are used as shown in **Figure 2.5**.

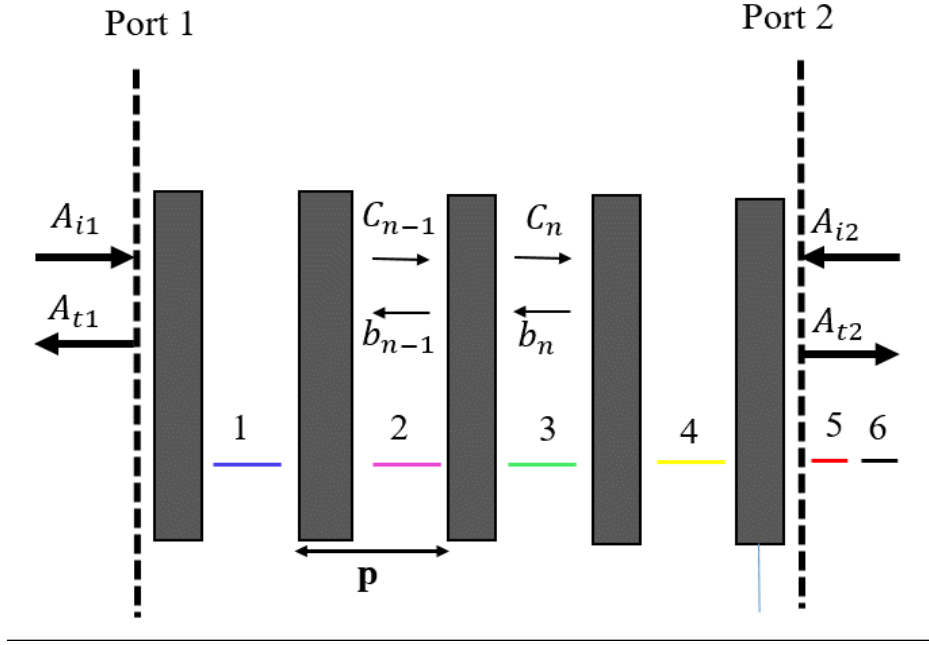


**Figure 2.5.** Schematic of 5 metallic finger IDT transducer used in COMSOL® simulations.  $A_{i1}$ ,  $A_{t1}$  and  $A_{i2}$ ,  $A_{t2}$  denote the incident and transmitted SAW amplitude from port 1 and port 2 respectively.  $C_n$  and  $b_n$  denote waves traveling to the right and left, respectively. Transducer pitch,  $p$ , is  $\frac{\lambda_0}{4}$ , where  $\lambda_0$ , is the center-frequency wavelength. Coloured lines between transducer electrodes indicate the positions at which the minimum displacement, rms field is calculated.

The electrode pitch,  $p$ , is  $\frac{\lambda_0}{4}$ , where  $\lambda_0$ , is the center-frequency wavelength. At this pitch and at the center-frequency, reflections from adjacent electrodes have phases differing by  $180^\circ$ , so that they cancel. In order to characterize the transducer model, we plot the displacement, rms field in the regions between the electrodes, denoted as 1, 2, 3 and 4 regions as well as in regions outside the transducer, denoted as 5 and 6 regions. The rms displacement field is defined as  $\frac{1}{\sqrt{2}} \sqrt{A_x^2 + A_y^2 + A_z^2}$ , where  $A_x$ ,  $A_y$ ,  $A_z$ , is the amplitude of the displacement field in the  $x$ ,  $y$ ,  $z$  directions, respectively. **Figure 2.6** shows the minimum rms displacement field, averaged along the cutlines shown in **Figure 2.5**.

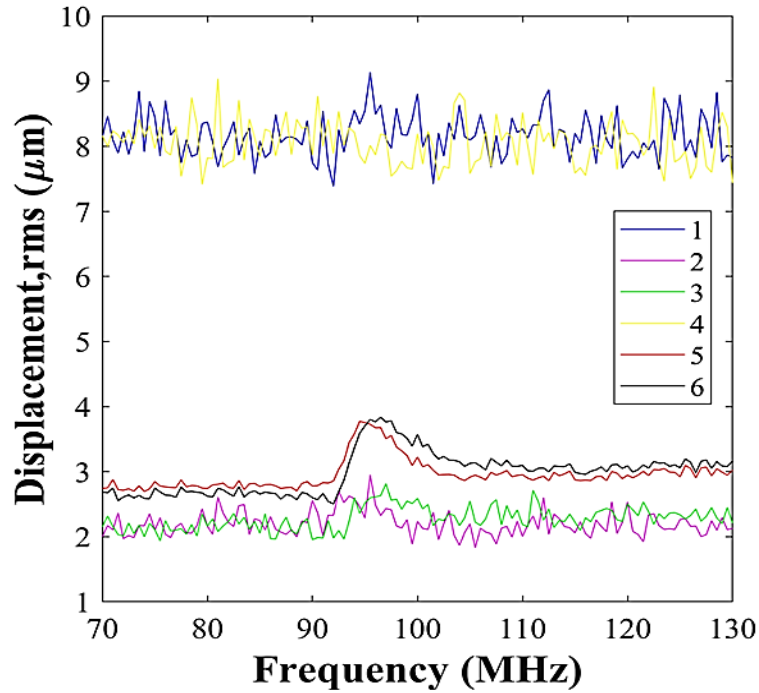


**Figure 2.6.** Displacement, rms field versus frequency calculated along the cutlines shown in **Figure 2.5**.

By observing the displacement fields at regions 5, 6 shown in red and black colors respectively, it is deduced that the operating frequency of the transducer is at the frequency region [92-102] MHz. At regions 5, 6 displacement fields have almost the same amplitude, meaning that there is no SAW propagation loss. Therefore, in what follows, coupling to the bulk waves will not be considered and it will be assumed that there is only one type of acoustic wave present, the Rayleigh wave. By observing the displacement fields at regions 2, 3, shown in magenta and green colors respectively, it can be seen that there are no large differences in their amplitudes, which is the case if we compare displacement fields between regions 1 and 4, shown in blue and yellow colors respectively. Regions 2, 3 and 1, 4 are positioned symmetrically with respect to the transducer center, hence the transducer is characterized as symmetrical and when a voltage is applied, the transducer generates surface waves of equal amplitude in the two directions. However, although in the area outside the transducer (regions 5, 6) there is no apparent loss, the average displacement field at region 1 is around 8  $\mu\text{m}$ , whereas the average displacement field at region 2 is around 2  $\mu\text{m}$ , as shown in **Figure 2.6**. The 75% decrease in

the average displacement field amplitude, may be attributed to reflections in the area between the transducer electrodes. Therefore, the reflective array method for an infinite grating is discussed in the next section, and the SAW scattering matrix is introduced.

#### 2.2.4.1 Rayleigh SAW grating

The behaviour of the SAW grating is described by considering power conservation in the acoustic ports on either side of the grating, shown in **Figure 2.5** and by assuming that the SAW amplitude, denoted by  $A$ , is uniform in the transverse direction. COMSOL® simulations have shown that uniform amplitude in the transverse simulation is achieved when the number of electrodes is very large, hence an infinite length grating will be considered in the following analysis, in order to exclude waveguiding and diffraction. The amplitudes are subscripted 1 or 2 to refer to the acoustic ports and i or t to refer to the incident and transmitted amplitudes respectively. If we exclude the electrical port, as the substrate is an insulating material, the SAW grating scattering matrix is defined:

$$\begin{bmatrix} A_{t1} \\ A_{t2} \end{bmatrix} = \begin{bmatrix} P_{11} & P_{12} \\ P_{21} & P_{22} \end{bmatrix} \begin{bmatrix} A_{i1} \\ A_{i2} \end{bmatrix} \quad (2.1)$$

Power conservation gives:

$$|A_{i1}|^2 + |A_{i2}|^2 = |A_{t1}|^2 + |A_{t2}|^2 \quad (2.2)$$

From (2,2) , (2,1) and by setting  $A_{i1}=0$  or  $A_{i2}=0$  it follows that

$$|P_{11}|^2 + |P_{21}|^2 = |P_{22}|^2 + |P_{12}|^2 \quad (2.3)$$

Setting  $A_{i2}A_{i1}^*$  to be either real or imaginary and subtracting the results gives:

$$P_{11}P_{12}^* + P_{12}P_{22}^* = 0 \quad (2.4)$$

Considering that waves traveling to the right and left have amplitudes denoted by  $C_n$  and  $b_n$  respectively, the scattering by the central electrode shown in **Figure 2.5** can be written as

$$b_{n-1} = (r_{s_1} C_{n-1} + t_s b_n) e^{-jk_e p}$$

$$C_n = (r_{s_2} b_n + t_s C_{n-1}) e^{-jk_e p}, \quad (2.5)$$

where the reflection coefficient is  $r_{s_1}$  for wave incident from the left and  $r_{s_2}$  for waves incident from the right. The transmission coefficient is  $t_s$  and  $k_e$  is the wavenumber. The grating mode solution, which is also called Bloch wave can be written as

$$C_n = C_{n-1} e^{-j\gamma p}$$

$$b_n = b_{n-1} e^{-j\gamma p} \quad (2.6)$$

,where  $\gamma$  is the Bloch wavenumber and it must be expressed in terms of frequency to obtain the dispersion relation. The physical meaning of the Bloch wave, which exists because of the presence of the SAW grating, will be thoroughly described in section 5.3. The Bloch wavenumber will be referred to as wavevector or wavenumber in the rest of this thesis for the sake of simplicity. Expressing the scattering P-matrix elements given in equation (2.1) in terms of reflection and transmission coefficients and substituting in relation (2.4) gives

$$r_{s_2} = -r_{s_1}^* \quad (2.7)$$

Further manipulation of equations (5) , (6) and (7) gives:

$$\cos(\gamma p) = \frac{\cos(k_e p)}{t_s} \quad (2.8)$$

The wavenumber  $k_e$  is real if we assume no losses and hence,  $\cos(\gamma p)$  is real. However,  $t_s = \sqrt{1 - |r_{s_1}|^2} = \sqrt{1 - |r_{s_2}|^2}$ , from which it follows that  $0 < t_s < 1$  . When  $k_e p$  is near  $M\pi$ , which is the case for certain frequencies, the right side of equation (2.8) has magnitude greater than unity. By Maclaurin series the first four terms of the cosine function are:

$$\cos(x) = 1 - \frac{x^2}{2!} + \frac{x^4}{4!} - \frac{x^6}{6!} \quad (2.9)$$

Therefore, if and only if the angle under consideration is complex the value of the cosine can be greater than one. If  $\gamma$  has an imaginary part, there are stop bands in the dispersion relation, as shown in **Figure 2. 7** (a). The imaginary part of  $\gamma$  is plotted in **Figure 2.7** (b). From both figures it can be seen that there is an infinite number of solutions for  $\gamma$ , which repeat at an interval  $\Delta\gamma = 2\pi/p$ .

If we assume losses that occur in the propagation between strips, as it is the practical case shown in **Figure 2.5**,  $k_e$  becomes complex but the above equations are still valid. The constant  $\gamma$  is imaginary at all frequencies in this case, so there is no clear distinction between the stop bands and the passbands. A time transient analysis is therefore necessary in order to confirm that the transducer consisted of 5 electrodes, used in COMSOL® modelling does not filter out certain frequencies of interest.

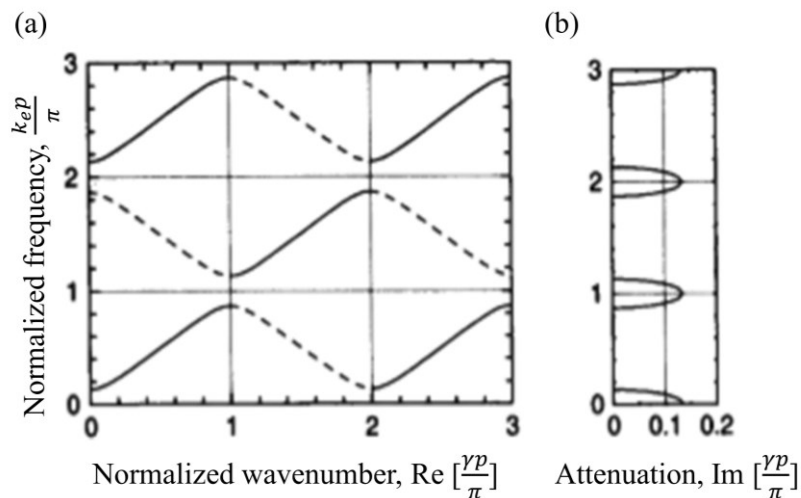


**Figure 2.7** (a) Frequency versus real part of the wavenumber. (b) Frequency versus imaginary part of the wavenumber, taken from [9].

#### 2.2.4.2 Excitation signal and response

The time domain analysis was performed via COMSOL® software. The geometry and the basic parameters of the time domain model will be introduced in Chapter 8, as the scope of this section is SAW excitation. The generation of wave signal is represented by [18],[19]

$$V_{in} = V \left[ H(t) - H \left( t - \frac{C}{f_c} \right) \right] \left[ 1 - \cos \left( \frac{2\pi f_c t}{C} \right) \right] \sin(2\pi f_c t) \quad (2.10)$$

where  $V$  is voltage amplitude,  $f_c$  is the central frequency of excitation,  $C$  is number of wave cycle,  $t$  is the time duration and  $H(t)$  is Heaviside step function. The number of wave cycles  $C$

was set to 5 and V was set to 1 V. For  $f_c = 97$  MHz, a pulse of duration 50 ns is illustrated in the following figure:

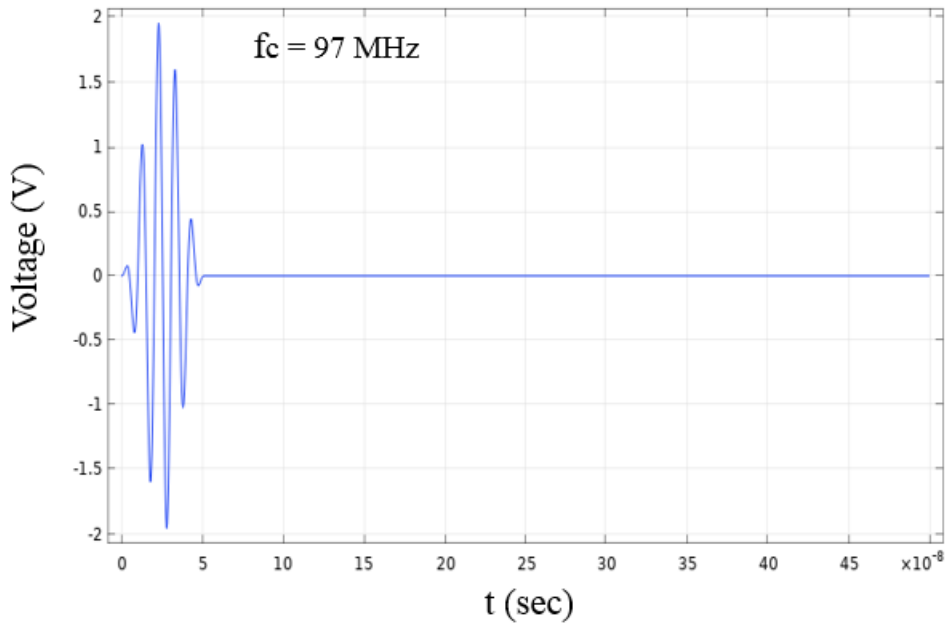


**Figure 2.8.** Voltage versus time for the pulse of equation (2.10), where  $C = 5$ ,  $V = 1$  V and  $f_c = 97$  MHz.

The frequencies of interest,  $f_c$ , are in the frequency range [100-200] MHz. Specifically, waves of central frequency  $f_c = 100$  MHz, 118 MHz, 135 MHz, 145 MHz, 150 MHz, 157 MHz and 200 MHz were launched and the response for each case is shown in **Figure 2.9 (a)**, where the displacement field along the  $z$  direction is plotted versus time. For  $f_c = 100$  MHz, the displacement is significantly decreased but is not zero. Therefore, the transducer does not filter out the above mentioned frequencies. The maximum displacement fields obtained from **Figure 2.9 (a)** were then plotted versus frequencies (**Figure 2.9 (b)**). It is shown that by doubling the excitation frequency the maximum displacement fields are increased by 78%.

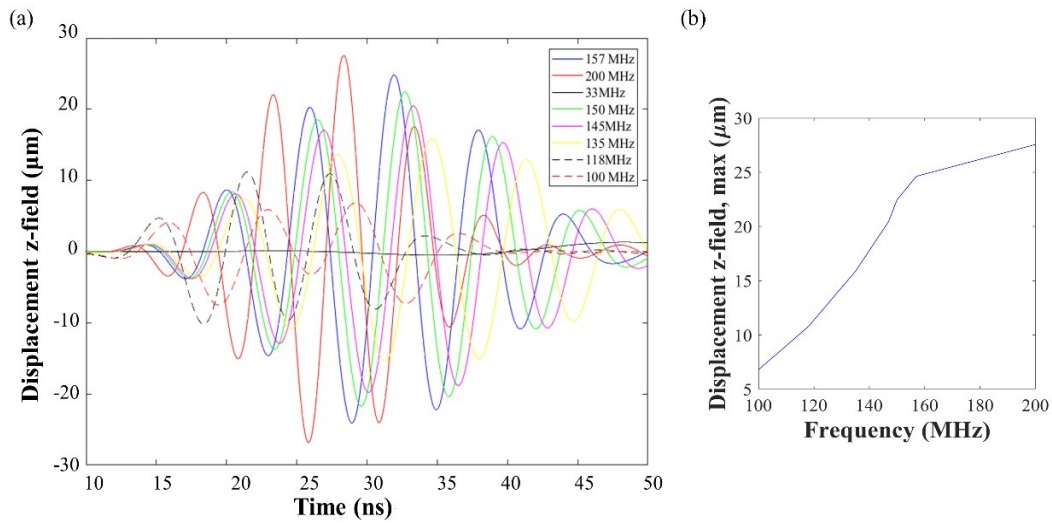


**Figure 2.9.** (a) Calculated displacement field along the direction normal to the surface versus time at different excitation frequencies: 100 MHz (red dashed line), 118 MHz (black dashed line), 135 MHz ( yellow solid line), 145 MHz (magenta solid line ), 150 MHz (green solid line), 157 MHz (blue solid line ), 200 MHz (red solid line ). (b) Maximum displacement field obtained from (a) versus frequency.

## 2.3 Surface wave solutions in a piezoelectric half space

### 2.3.1 Elasticity

When a body is subjected to an applied force the body will deform. The ability of a body to recover from this deformation is called elasticity. In this thesis, materials which recover completely from a deformed shaped will be considered, that is materials which are perfectly elastic.

### 2.3.2 Stress

Stress is defined as the force per unit area acting on a body which may be expressed as:

$$\text{Stress} = \lim_{\Delta A \rightarrow 0} \frac{\Delta F}{\Delta A} \quad (2.11)$$

where  $\Delta F$  is the force acting on the area  $\Delta A$ . The notation used for identification of stress components is demonstrated in **Figure 2.10** (a). The normal stresses are denoted by  $\sigma_i$ , where  $i$  represents the coordinate direction in which the stress acts. The shear stresses are denoted by  $\tau_{ij}$ , where  $i$  represents the direction of the normal to the plane in which the stress acts, and  $j$  represents the direction of stress [20]. If the cubic element in **Figure 2.10** (b) is in equilibrium, the sum of moments is zero giving

$$2\tau_{zy}(dydx) \frac{dz}{2} - 2\tau_{yz}(dzdx) \frac{dz}{2} = 0 \quad (2.12)$$

from which it follows that  $\tau_{zy} = \tau_{yz}$ , meaning that the number of stress components is reduced to six.

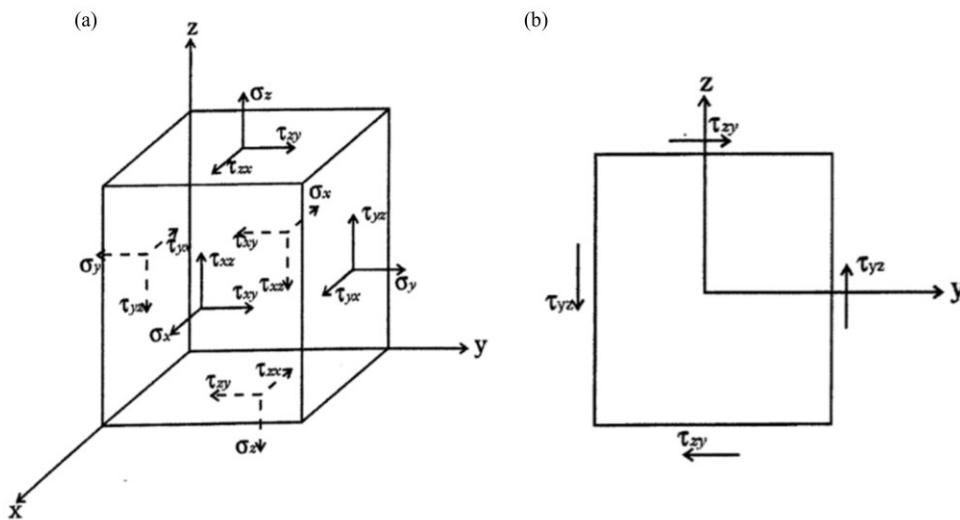


**Figure 2.10.** (a) Notation for stress components in a Cartesian coordinate system; (b) shear stresses on a plane. Taken from [21]

### 2.3.3 Strain

Strain describes the deformation of a body and quantifies the displacement of points in the body. If the displacement of a point in a body in the x, y and z directions is u, v and w respectively, the strains are defined as [20]:

$$\varepsilon_x = \frac{\partial u}{\partial x}, \quad \varepsilon_y = \frac{\partial v}{\partial y}, \quad \varepsilon_z = \frac{\partial w}{\partial z} \quad (2.13)$$

$$\gamma_{xy} = \frac{1}{2} \left( \frac{\partial v}{\partial x} + \frac{\partial u}{\partial y} \right), \quad \gamma_{yz} = \frac{1}{2} \left( \frac{\partial w}{\partial y} + \frac{\partial v}{\partial z} \right), \quad \gamma_{xz} = \frac{1}{2} \left( \frac{\partial w}{\partial x} + \frac{\partial u}{\partial z} \right) \quad (2.14)$$

where  $\varepsilon_x, \varepsilon_y, \varepsilon_z$  are the longitudinal strain components and  $\gamma_{xy}, \gamma_{yz}, \gamma_{xz}$  are the shearing strain components. The assumption in the derivation of these equations is that the deformation of the body is small [22], [23].

### 2.3.4 Generalised Hooke's Law for anisotropic materials

An equation relating the deformation of an elastic body to the applied forces, through the stresses and strains of the body is the generalised Hooke's law:

$$\begin{aligned} \sigma_x &= c_{11}\varepsilon_x + c_{12}\varepsilon_y + c_{13}\varepsilon_z + c_{14}\gamma_{yz} + c_{15}\gamma_{xz} + c_{16}\gamma_{xy} \\ \sigma_y &= c_{21}\varepsilon_x + c_{22}\varepsilon_y + c_{23}\varepsilon_z + c_{24}\gamma_{yz} + c_{25}\gamma_{xz} + c_{26}\gamma_{xy} \\ \sigma_z &= c_{31}\varepsilon_x + c_{32}\varepsilon_y + c_{33}\varepsilon_z + c_{34}\gamma_{yz} + c_{35}\gamma_{xz} + c_{36}\gamma_{xy} \\ \tau_{yz} &= c_{41}\varepsilon_x + c_{42}\varepsilon_y + c_{43}\varepsilon_z + c_{44}\gamma_{yz} + c_{45}\gamma_{xz} + c_{46}\gamma_{xy} \\ \tau_{xz} &= c_{51}\varepsilon_x + c_{52}\varepsilon_y + c_{53}\varepsilon_z + c_{54}\gamma_{yz} + c_{55}\gamma_{xz} + c_{56}\gamma_{xy} \\ \tau_{xy} &= c_{61}\varepsilon_x + c_{62}\varepsilon_y + c_{63}\varepsilon_z + c_{64}\gamma_{yz} + c_{65}\gamma_{xz} + c_{66}\gamma_{xy} \end{aligned} \quad (2.15)$$

The coefficients  $c_{ij}$  describe the elastic properties of the material and the above equations imply that a normal stress  $\sigma_x$ , will induce a material element to not only stretch in the x direction and contract laterally, but to undergo shear strain too. The above equation can be written in a more compact, matrix form if we denote stresses as  $T_{ij}$  (where  $T_{11}$ , corresponds to  $\sigma_{xx}$ ) and strains as  $S_{kl}$ .

$$T_{ij} = \sum_k \sum_l c_{ijkl} S_{kl}, \quad i,j,k,l=1,2,3 \quad (2.16)$$

Considering equations (2.14),  $S_{ij}$  can be expressed as:

$$S_{ij} = \frac{1}{2} \left( \frac{\partial u_i}{\partial x_j} + \frac{\partial u_j}{\partial x_i} \right), \quad i,j=1,2,3 \quad (2.17)$$

Here  $c_{ijkl}$  is the stiffness tensor of the material which is a fourth rank tensor. The number of elastic constants may be reduced if the material is hyperelastic, in which case the deformation takes place isothermally or adiabatically. Then the elastic constants are symmetrical such that  $c_{ijkl} = c_{klji}$ , meaning that the total number of independent elements is 21. The values of those 21 independent elements, which were used to simulate LiNbO<sub>3</sub> which is an anisotropic, piezoelectric material are given in the Appendix of Chapter 4.

### 2.3.5 Equations of motion for bulk elastic waves in anisotropic, non-piezoelectric materials

By considering the variation of stress across the small cubic element shown in **Figure 2.10** (a) and by assuming that the cube edge is  $\delta$ , the equation of motion can be derived. Under a stress described by equation (2.16), the material exerts a force on each of the six faces along the x direction, denoted as 1. Specifically, on the zy face and at  $x = \delta$  the force is:

$$(T_{x1} \delta^2 + \frac{\partial T_{x1}}{\partial x} \delta^3) \quad (2.18)$$

On the zy face and at  $x = 0$  the force exerted is:

$$-(T_{x1}\delta^2) \quad (2.19)$$

On the zx face and at  $y = \delta$  the force exerted is:

$$+(T_{y1}\delta^2 + \frac{\partial T_{y1}}{\partial y}\delta^3) \quad (2.20)$$

On the zx face and at  $y = 0$  the force exerted is:

$$-(T_{y1}\delta^2) \quad (2.21)$$

On the xy face and at  $z = \delta$  the force exerted is:

$$+(T_{z1}\delta^2 + \frac{\partial T_{z1}}{\partial z}\delta^3) \quad (2.22)$$

On the xy face and at  $z = 0$  the force exerted is:

$$-(T_{z1}\delta^2) \quad (2.23)$$

Summing the forces to obtain the total force acting in the x direction and equating to Newton's second law of motion gives:

$$\frac{\partial T_{x1}}{\partial x}\delta^3 + \frac{\partial T_{y1}}{\partial y}\delta^3 + \frac{\partial T_{z1}}{\partial z}\delta^3 = \rho\delta^3 \frac{\partial^2 u_1}{\partial t^2} \quad (2.24)$$

The above equation can be expressed as

$$\sum_j \frac{\partial T_{ij}}{\partial x_j} = \rho \frac{\partial^2 u_i}{\partial t^2}, \quad i = 1,2,3 \quad (2.25),$$

which is the equation of motion for bulk elastic waves in anisotropic, non-piezoelectric materials.

### 2.3.6 Equations of motion for bulk elastic waves in anisotropic, piezoelectric materials and electroelastic coupling

Considering that the piezoelectric material is homogeneous anisotropic and insulating, the coupling between elastic stresses and strains to electric fields and displacements is described by the following equation,

$$T_{ij} = \sum_k \sum_l c_{ijkl}^E S_{kl} - \sum_k e_{kij} E_k \quad (2.26)$$

Here  $c_{ijkl}^E$  represents the stiffness tensor for constant electric field and  $e_{kij}$  represents the piezoelectric coupling coefficient relating elastic to electric fields. The electric displacement  $D$  is found to be dependent on strain such that

$$D_i = \sum_j \varepsilon_{ij}^S E_j + \sum_j \sum_k e_{ijk} S_{jk} \quad (2.27)$$

where  $\varepsilon_{ij}^S$  is the permittivity tensor for constant strain. The complete derivation of these equations can be found in [24]. In the quasi-static approximation an electric field can be defined by:

$$E_i = -\frac{\partial \Phi}{\partial x_i}, \quad i = 1, 2, 3 \quad (2.28)$$

where  $\Phi$  is the electric potential. Moreover, in the quasi-static approximation the Maxwell equation amounts to the Poisson's equation:

$$\nabla \cdot \mathbf{D} = \frac{\partial D_i}{\partial x_i} = 0 \quad (2.29)$$

Replacing (2.17) and (2.28) in (2.26) and (2.27), we obtain

$$T_{ij} = \sum_k \sum_l c_{ijkl}^E \frac{1}{2} \left( \frac{\partial u_l}{\partial x_k} + \frac{\partial u_k}{\partial x_l} \right) + \sum_k e_{kij} \frac{\partial \Phi}{\partial x_k} \quad (2.30)$$

$$D_{ij} = -\sum_k \varepsilon_{ik}^S \frac{\partial \Phi}{\partial x_k} + \sum_j \sum_k e_{ijk} \frac{1}{2} \left( \frac{\partial u_j}{\partial x_k} + \frac{\partial u_k}{\partial x_j} \right) \quad (2.31)$$

Replacing (2.30) in the equation of motion (2.25) gives:

$$\rho \frac{\partial^2 u_i}{\partial t^2} = \sum_j \sum_k \sum_l c_{ijkl}^E \frac{\partial^2 u_k}{\partial x_j \partial x_l} + \sum_j \sum_k e_{kij} \frac{\partial^2 \Phi}{\partial x_j \partial x_k} \quad (2.32)$$

Replacing (2.31) in (2.29) gives

$$-\sum_{k,i} \varepsilon_{ik}^S \frac{\partial^2 \Phi}{\partial x_k \partial x_i} + \sum_{i,k,l} e_{ikl} \frac{\partial^2 u_k}{\partial x_l \partial x_i} = 0 \quad (2.33)$$

Equations (2.32) and (2.33) characterize the electroelastic coupling between the elastic displacement vector of components  $u_1, u_2, u_3$  and the electric potential  $\Phi$ . By substituting the form of solution for  $u_1, u_2, u_3$  and  $\Phi$  into equations (2.32) and (2.33) and applying the appropriate boundary conditions (see section 2.3.7), the relative amplitude of the  $u_1$  and  $u_3$  components can be obtained and it can be proven that the particle motion is retrograde elliptical, as shown earlier in this chapter (see **Figure 2.1**).

### 2.3.7 The form of solution and the boundary conditions for a piezoelectric half-space

The piezoelectric wave is the solution of the elastic and electric equations that satisfy elastic and electric boundary conditions. The coordinate system used in order to define the solution form is shown in **Figure 2.11**.

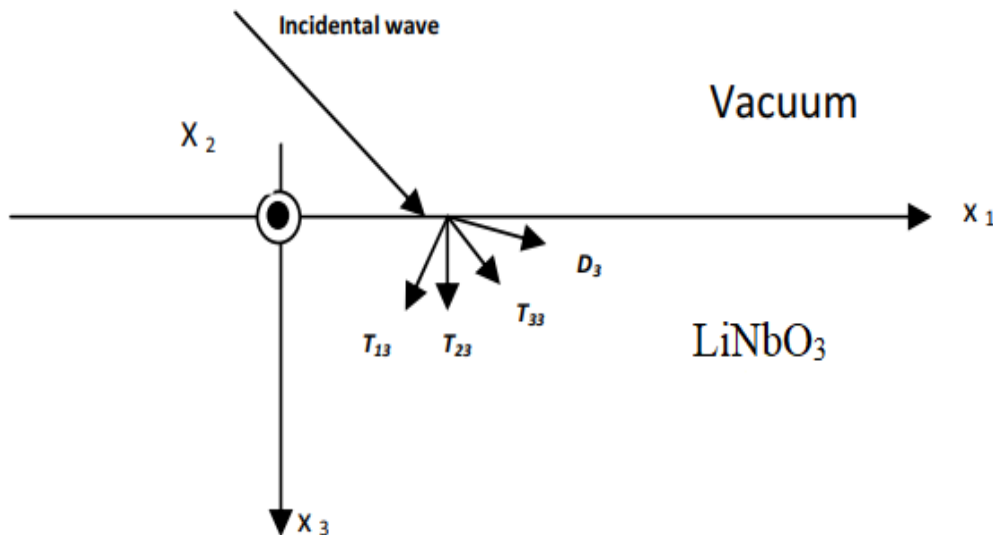


**Figure 2.11.** Coordinate system for the surface wave propagation in a semi-infinite structure. Modified from [25].

The  $x_3$  axis is normal to the surface and the region with  $x_3 > 0$  is considered to be vacuum and free of charges and stresses. For sinusoidal traveling waves along  $x_1$  at a radian frequency  $\omega$  radians per second, the assumed solution form, considering that the attenuation in the  $x_1$  direction is zero is:

$$\begin{aligned} \mathbf{u}(x_1, x_3, t) &= \mathbf{B}e^{ik_1x_1}e^{ik_3x_3}e^{-i\omega t} = \mathbf{B}e^{ik_1\left(x_1 + \frac{k_3}{k_1}x_3\right)}e^{-i\omega t} \Rightarrow \\ \mathbf{u}(x_1, x_3, t) &= \mathbf{B}e^{ik_1bx_3}e^{ik_1(x_1 - v_p t)}, \end{aligned} \quad (2.34)$$

where  $v_p$  is the phase velocity along  $x_1$  and  $b = \frac{k_3}{k_1}$ , the wave number ratio. The vector of normal stresses  $\mathbf{T}_3 = [T_{13} \ T_{23} \ T_{33}]^t$  and the elastic displacement vector  $\mathbf{u} = [u_1 \ u_2 \ u_3]^t$  are chosen as the six mechanical variables since these must be continuous across interfaces. Moreover, at the free surface,  $x_3 = 0$ , the stress free boundary conditions apply and both tangential and normal stresses are set to zero. Hence  $T_{13}(x_3 = 0) = T_{33}(x_3 = 0) = 0$ . The electric variables which must be continuous are two: the normal electric displacement component  $D_3$ , and the electric potential  $\Phi$ . For a metallised surface  $\Phi = 0$  at  $x_3 = 0$ . These 8 variables are a sufficient independent set and all other variables can be expressed as linear combination of the chosen ones [26]. Therefore there are eight complex roots for the wave number ratio and we have:

$$\mathbf{u}_m(x_1, x_3, t) = \mathbf{B}e^{ik_1b_mx_3}e^{ik_1(x_1 - v_p t)} \quad (2.35)$$

where  $m=1,2,3,\dots,8$ . However, in the surface mode (or Rayleigh wave) the eight different complex roots for  $b_i$  are conjugated by pairs and only the complex roots with positive imaginary parts are taken into consideration (for convergence reasons), which are four

$$b_m = \alpha_m + |c_m|i \quad m=1,\dots,4 \quad (2.36)$$

Substitution of (2.36) into (2.35) gives:

$$\mathbf{u}_m(x_1, x_3, t) = \mathbf{B}e^{-k_1|c_m|x_3}e^{ik_1(x_1 + \alpha_ix_3)}e^{-i\omega t} \quad (2.37)$$

The same form of solution holds for the potential:

$$\Phi_m(x_1, x_3, t) = Ae^{-k_1|c_m|x_3}e^{ik_1(x_1 + \alpha_ix_3)}e^{-i\omega t} \quad (2.38)$$

The solution is assumed to be a linear summation of these partial waves in the half space such that:

$$\mathbf{u}_i = \sum_{m=1}^4 A_m \mathbf{u}_m \quad (2.39)$$

$$\Phi = \sum_{m=1}^4 A_m \Phi_m \quad (2.40)$$

Substitution of (2.39) and (2.40) into (2.32) and (2.33), gives four relations between the four quantities  $\mathbf{u}_i$  and  $\Phi$ , and hence the particle motion is determined when the above mentioned boundary conditions are applied. Literature to the general form of the system matrix  $A$ , is given in the next section. The matrix method is employed to calculate the SAW velocity in layered piezoelectric structures, although the SAW velocity can also be specified experimentally. The SAW velocity is required as an input value in our computational model and it is set at 3960 [m/s], after experimental verification. We used an oscilloscope to measure how long it takes for a pulse to propagate from the excitation to the receive transducer. However, for the sake of completeness the matrix method is presented in the following section.

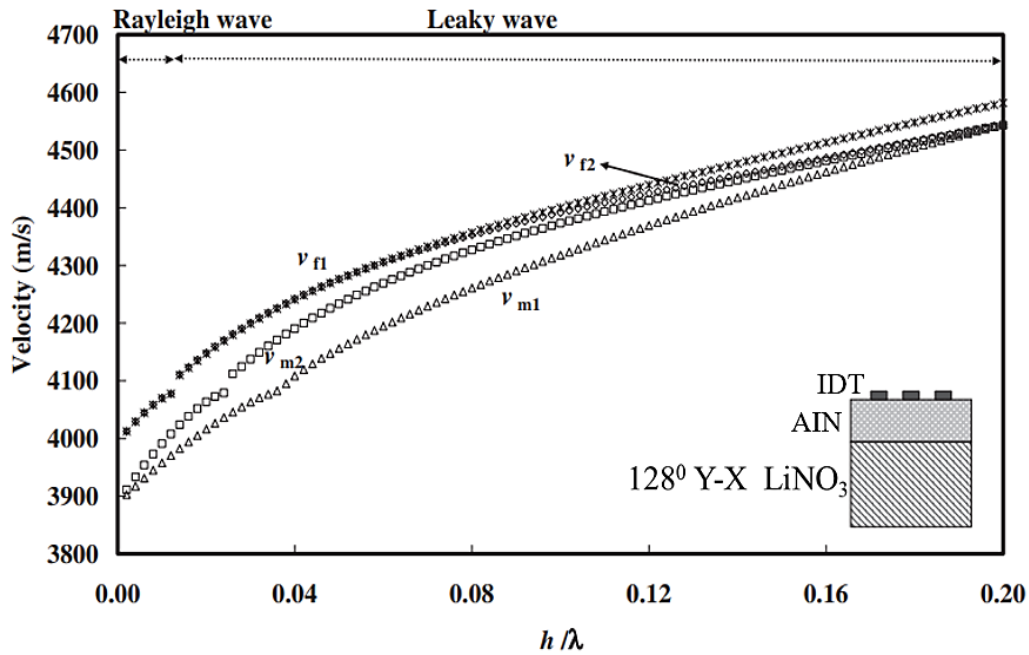
### 2.3.8 The system ordinary differential equation and the system matrix

For a free piezoelectric surface at  $x_3 = 0$  there are no variations in the  $x_2$  direction, hence  $d/dx_2 = 0$ . In the  $x_1$  direction the variation is  $d/dx_1 = -j\omega/v_p$  and in the  $x_3$  direction the variation in the sinusoidal steady state is [27]:

$$\frac{d\boldsymbol{\tau}}{dx_3} = j\omega\mathbf{A}\boldsymbol{\tau} \quad (2.41),$$

where  $\boldsymbol{\tau}$  is the eight-component vector comprised of the 8 variables, that were introduced in the previous section  $\boldsymbol{\tau} = [\mathbf{T}_3 \ D_3 \ \mathbf{u} \ \Phi]^t$ . For convenience vector-columns are written as transposes of row vectors. The system matrix  $A$  is a function of material constants referred to the coordinate system of **Figure 2.11** and of the phase velocity  $v_p$ . For a piezoelectric material, the  $A$  matrix, described by Adler E. in [26], contains 4×4 compliance and stiffness submatrices. These submatrices contain compliance, stiffness, piezoelectric and permittivity constants included in equations (2.26) and (2.27). The phase velocity as well as the attenuation

coefficients for a  $128^\circ$  Y-X cut  $\text{LiNO}_3$  substrate layered with an AlN film were obtained numerically by solving the above mentioned system matrix and the results are shown in **Figure 2.12** [28]. The phase velocities obtained when the electrical boundary conditions at the interface at which the IDT is placed are assumed to be electrically free and shorted, are  $v_f$  and  $v_m$  are respectively. The subscripts 1 and 2 in  $v_{f1}$  and  $v_{f2}$  indicate the AlN film is deposited on the positive surface and the negative surface of the substrate. The thickness of the AlN substrate is  $h$ , and determines whether the solution is a Rayleigh wave or a leaky wave. The criterion for the wave to be considered as Rayleigh wave is zero attenuation coefficient and the horizontal dashed line indicate the two regions. It can be observed that for  $h \rightarrow 0$  the SAW phase velocity is 3900 m/s and 4000 m/s for the metallised and free cases respectively.



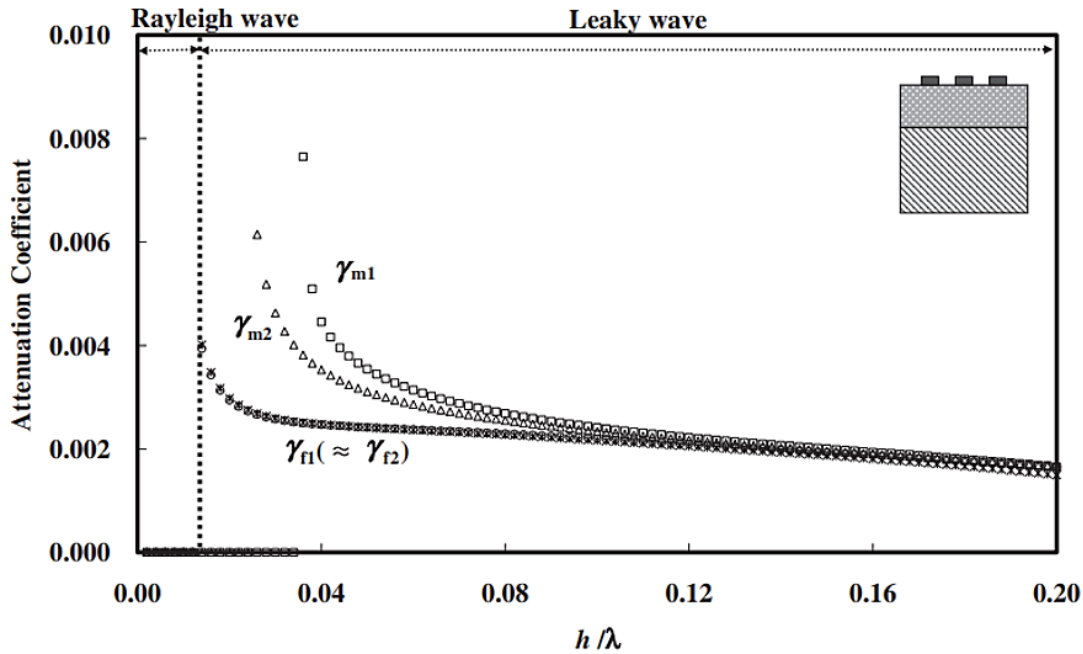


**Figure 2.12.** Upper panel: Calculated phase velocity versus  $h/\lambda$  for an IDT/AlN/128° Y-cut LiNbO<sub>3</sub> structure. The subscripts 1 and 2 indicate the AlN film is deposited on the positive surface and the negative surface of the substrate, respectively. Lower panel: Calculated attenuation coefficient for the same structure. Modified from [28].

### 2.3.9 Conclusions

Rayleigh SAW propagation in a piezoelectric medium results in retrograde elliptical motion of the medium particles. This is confirmed by substituting the form of solution for a piezoelectric half-space to the equations of motion for a piezoelectric material. Lithium niobate is selected as a substrate due to its high piezoelectric coupling to the Rayleigh SAW which ensures almost lossless propagation. Interdigital transducer is selected as excitation source thanks to its direct piezoelectric coupling to surface elastic waves. Coupling is confirmed by the peak shown in the calculated rms displacement field at the area outside the transducer, whereas in the area between the transducer fingers a decrease in the average displacement field amplitude is observed. This decrease is attributed to losses that occur in the propagation between strips and the time transient COMSOL® modelling proves that certain frequencies of interest are not

filtered out by the 5 finger transducer. The matrix method is described and it is deduced that the theoretical value of the phase velocity for Rayleigh SAWs propagating in free  $128^\circ$  Y-X cut  $\text{LiNO}_3$  substrate is 4000 m/s. It is also shown that the absence of an AlN substrate between transducers and substrate favors Rayleigh SAW propagation against the leaky wave.

## **CHAPTER 3**

### **Acoustic surface waves (ASWs)- Sound in air**

#### **3.1 Introduction**

In Chapter 2 the equations describing sound propagating through a solid piezoelectric material were given and the surface mode obtained by the solution of those equations subject to specific boundary conditions was denoted as Rayleigh SAW wave. In that case, the SAW existed between an infinite solid and a vacuum, and decayed away exponentially from the boundary into the solid with elliptical particle oscillations.

In the present chapter those oscillations are not possible, as all solids are treated as perfectly rigid, meaning that by definition a SAW cannot exist. The interaction of sound with a region of air bounded by a rigid-walled cavity is the key focus of this chapter. For the ease of the reader, the propagation of sound through an unbound gas and the equations describing it will be introduced before moving to the description of the rigid-walled bound gas interacting with sound. A gas will be considered as a fluid for the purpose of this chapter and hence, when it is in contact with a rigid-boundary, viscous and thermal effects will be accounted for. We are only concerned with air as the fluid in which sound propagates and we will start our analysis by showing that only longitudinal pressure waves can be generated in this medium. In contrast, sound propagating through an elastic solid (described in Chapter 2), generates shear waves which propagate in orthogonal directions to the longitudinal pressure waves. This is because molecules which are part of the solid, are tightly bound to a lattice and their shear displacement depends on many parameters, one of those being the exact molecular structure of the lattice.

In the last section of this chapter thermoviscous effects will be neglected in order to simplify the discussion of the formation of resonances in rigid-walled cylindrical pipes. For the same reason an analogue to a similar system for which resonances have been investigated both experimentally and theoretically will be presented.

#### **3.2 Sound generation in air**

Sound is generated by continuous and regular vibrations, as opposed to noise, and travels through some elastic medium via molecular collisions caused by fluctuations in density and pressure. Air is an elastic medium since its bulk modulus can be defined. A uniform

compression of an air column leads to a decrease of its volume. In the case that we have a constant-entropy process, the approximate bulk modulus of air is 101 kPa, meaning that air loses one percent of its volume when subjected to an external pressure of 1.01 kPa. It is worth mentioning however, that air is less elastic when compared to solids such as steel (bulk modulus,  $K = 160\text{GPa}$ ) or diamond ( $K = 443\text{GPa}$  at 4 K). If we consider a large vibrating plate as the source for sound generation in air, and considering that the plate is moving in the positive  $x$  direction, the region of air adjacent to the plate is compressed and its density is increased, as shown schematically in **Figure 3.1**. As a result the fluid molecules at this region of air will respond by diffusing to a lower pressure region further along  $x$ . In turn, the pressure in this region increases and the whole process repeats, with the compression propagating along the positive  $x$  direction. Similarly, when the plate moves along the negative  $x$  direction, the air density in the region adjacent to the plate decreases and so does the pressure. Hence, the fluid molecules move to a high pressure region and again the whole process repeats, leading to a travelling rarefaction. The pressure wave is constituted by this set of travelling compressions and rarefactions and its wavelength is the distance between adjacent compressions or rarefactions. The maximum amplitude of the oscillation is the deviation  $+\delta P$  from the atmospheric pressure and it is shown in the upper panel of **Figure 3.1**.

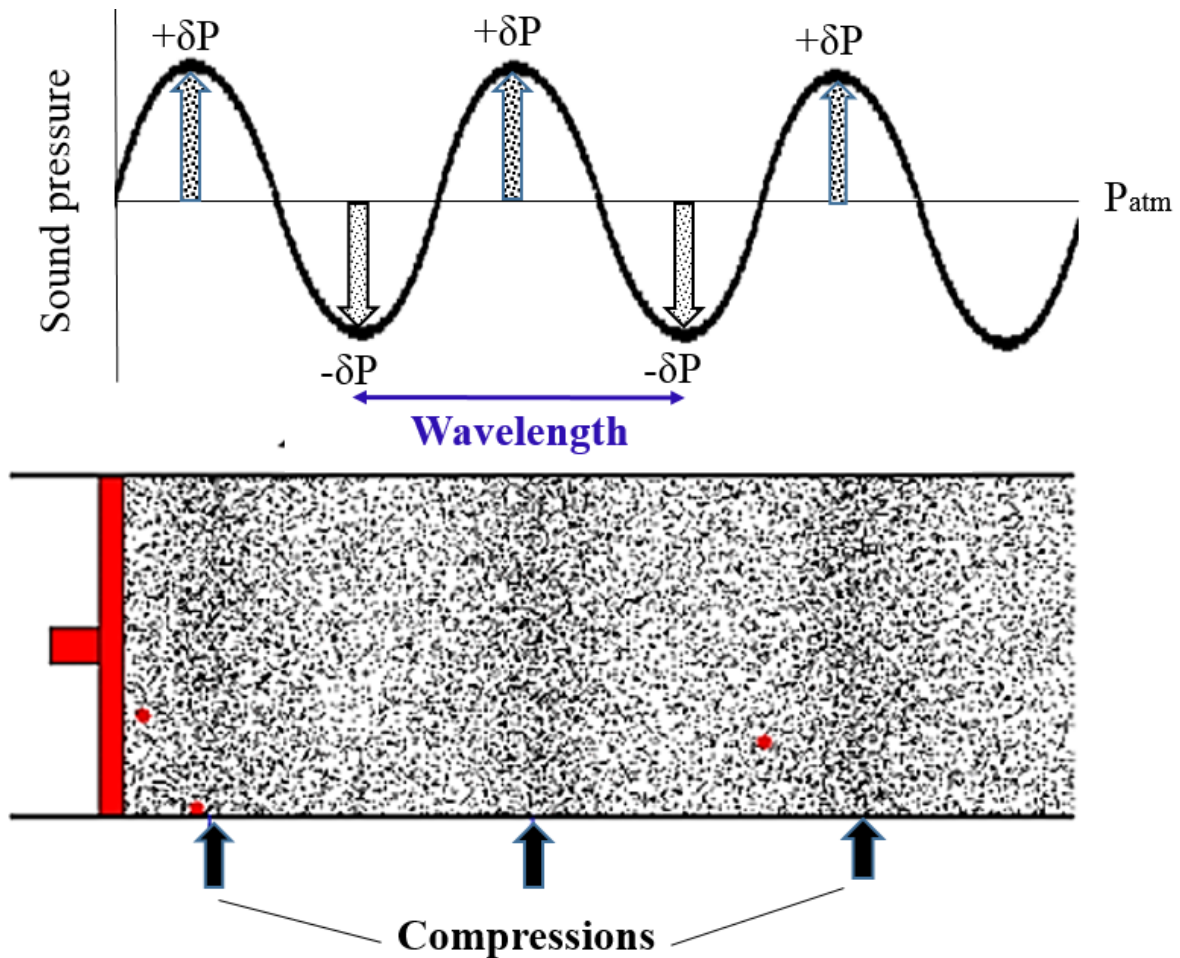


**Figure 3.1.** Qualitative illustration of sound generation by a vibrating plate. Black points represent the air molecules.

### 3.3 Sound propagation through an unbound gas

Once the acoustic wave has been generated by means discussed in the previous section, the fluid on which it propagates will undergo perturbations in its pressure, density, temperature and velocity. Considering that the unperturbed fluid has definite-valued and time independent thermodynamic variables pressure  $p_0$ , density  $\rho_0$ , temperature  $T_0$  and velocity  $\vec{v}_0$ , the perturbation state can be stated as  $p_0 + \Delta p$ , where  $p_0 \gg \Delta p$ ,  $\rho_0 + \Delta \rho$ , where  $\rho_0 \gg \Delta \rho$  and  $T_0 + \Delta T$ , where  $T_0 \gg \Delta T$ . The background velocity,  $\vec{v}_0$ , is assumed to be zero since the fluid is assumed to be stationary. Moreover, it is assumed that no heat transfer occurs between regions of high and low pressure and density, hence the propagation of sound is considered as an adiabatic process. The complex intermolecular processes occurring within the fluid are also ignored and, as this section describes sound propagation through an unbound gas, the fluid is

treated as frictionless. Friction is the resistance that one object encounters when moving over another and when considering fluid particles, the term used is viscosity. A high viscosity fluid is more resistant to deformation, but in this section, the fluid's resistance to shearing (resistance to forces acting on particles between adjacent regions of different net velocity) is assumed to be zero. That resistance is quantified in terms of the shear viscosity coefficient,  $\eta$ , and its value (given in Table 3.1) is significant when the propagation medium is in contact with a rigid boundary, which will be analysed in section 3.4. The shear viscosity coefficient is also referred to as dynamic viscosity and is related to the kinematic viscosity  $\nu$  by the relation  $\eta = \rho_0 \nu$ . Kinematic viscosity is hence obtained by dividing the dynamic viscosity of the fluid with the fluid mass density  $\rho_0$ . Note that the background density  $\rho_0$  is a function of temperature and pressure. In the present section, the equations required to define  $\Delta p$ , the scalar pressure and  $u_x$ , the velocity of gas molecules along x direction will be presented.

### 3.3.1 Equation of state for an ideal gas

In the case of an ideal gas, the equation of state is written as:

$$\frac{p}{\rho} = RT, \quad (3.1)$$

where  $R$ , is the gas constant and takes the value  $287.058 \text{ J}\cdot\text{K}^{-1}\cdot\text{kg}^{-1}$ ,  $\rho$ ,  $p$  and  $T$ , the gas density, pressure and temperature respectively [29]. The equation is derived after applying conservation of energy and momentum laws to classic kinetic theory and describes the propagation of sound through an unbound gas, when the process can be considered adiabatic. Hence, once two independent thermodynamic variables are known, the other variable can be determined. In order to fully describe the gas, the conservation of mass and the conservation of momentum equations are required.

### 3.3.2 Conservation of mass – Continuity equation

The conservation of mass law states that matter cannot be created or destroyed. Therefore the rate of flow into a volume element of a fluid  $dV$  ( $= dx \, dy \, dz$ ) must be equivalent to the rate at which mass leaves the system plus the gain of fluid within the system [30]. For compressible

fluid flow, the fluid density is dependent on space and time and for the velocity vector field  $\vec{v}$ , the differential form of the conservation of mass law, also known as the continuity equation is:

$$\frac{\partial \rho}{\partial t} - \nabla(\rho \mathbf{v}) = 0 \quad (3.2)$$

where  $\nabla = \frac{\partial}{\partial x} \hat{\mathbf{x}} + \frac{\partial}{\partial y} \hat{\mathbf{y}} + \frac{\partial}{\partial z} \hat{\mathbf{z}}$ , is the gradient operator.

### 3.3.3 Conservation of momentum

Newton's second law neglecting viscous forces, gives the forces acting upon a fluid volume element  $dV$  is:

$$d\mathbf{F} = d\mathbf{m}\mathbf{a} \quad (3.3)$$

where  $\mathbf{a}$  is the acceleration of a particle moving within velocity field  $\mathbf{v}$  and is written as:

$$\mathbf{a} = \frac{D\mathbf{v}}{Dt} \quad (3.4)$$

The operator  $\frac{D}{Dt}$ , known as the convective derivative is given by:

$$\frac{D}{Dt} = \frac{\partial}{\partial t} + \frac{\delta x}{\delta t} \frac{\partial}{\partial x} + \frac{\delta y}{\delta t} \frac{\partial}{\partial y} + \frac{\delta z}{\delta t} \frac{\partial}{\partial z} \quad (3.5)$$

This is because in a time interval  $Dt$ , the coordinates of the fluid volume element change in time as the fluid flows. Specifically the x-coordinate changes by  $v_x Dt$ , the y-coordinate changes by  $v_y Dt$  and the z coordinate by  $v_z Dt$ . Therefore, the acceleration is not simply  $\frac{\partial \mathbf{v}}{\partial t}$ , implying that even if the velocity at a given point is not changing, the fluid element may be accelerating. An example is a circular flow in a bucket; if the flow is steady,  $\frac{\partial \mathbf{v}}{\partial t} = 0$  at a point in the bucket, although a fluid element is experiencing centripetal acceleration. In section 2.3.5, the variation of stress across a small cubic element was described and it was shown the total force acting in the x direction is

$$F_x = \left( \frac{\partial T_{x1}}{\partial x} + \frac{\partial T_{y1}}{\partial y} + \frac{\partial T_{z1}}{\partial z} \right) \delta^3, \quad (3.6)$$

where  $\delta^3$  equals  $dV$ , and subscript 1 corresponds to the x direction. Assuming that gravity along x direction is  $g_x$  the sum of forces  $d\mathbf{F}$  acting along x direction is written as:

$$dF_x = \left( \rho g_x + \frac{\partial T_{xx}}{\partial x} + \frac{\partial T_{yx}}{\partial y} + \frac{\partial T_{zx}}{\partial z} \right) dV \quad (3.7)$$

Newton's second law therefore gives:

$$\rho g_x + \frac{\partial T_{xx}}{\partial x} + \frac{\partial T_{yx}}{\partial y} + \frac{\partial T_{zx}}{\partial z} = \rho \left( \frac{\partial v_x}{\partial t} + \frac{\delta x}{\delta t} \frac{\partial v_x}{\partial x} + \frac{\delta y}{\delta t} \frac{\partial v_x}{\partial y} + \frac{\delta z}{\delta t} \frac{\partial v_x}{\partial z} \right) \quad (3.8)$$

For a Newtonian fluid the normal and shear stress tensors are given by the following equations which arise from complex fluid mechanics discussed in [31]:

$$T_{xx} = -\Delta p - \frac{2}{3} \eta \nabla \cdot \mathbf{v} + 2\eta \frac{\partial v_x}{\partial t} \quad (3.9)$$

$$T_{yx} = T_{xy} = \eta \left( \frac{\partial v_y}{\partial x} + \frac{\partial v_x}{\partial y} \right) \quad (3.10)$$

and similar for the other dimensions. Considering the frictionless fluid assumption  $\eta = 0$ , valid for the description of an unbound gas, and taking the gravitational force as negligible, Newton's second law can be rewritten as:

$$-\nabla(\Delta p) = \Delta \rho \frac{D\mathbf{v}}{Dt} \quad (3.11)$$

which is known as the linear Euler's equation [32] and along with the continuity equation are the governing equations of nonviscous fluid flow.

### 3.3.4 The acoustic wave equation

Considering the assumptions discussed in section 3.3 and treating the x-direction only the continuity equation (3.2) reduces to:

$$\frac{\partial \Delta \rho}{\partial t} = -\rho_0 \frac{\partial v_x}{\partial x} \quad (3.12)$$

The momentum equation (3.11) reduces to:

$$\frac{\partial \Delta p}{\partial x} = -\rho_0 \frac{\partial v_x}{\partial t} \quad (3.13)$$

For an ideal gas, the adiabatic process condition states that:

$$p\rho^\gamma = \text{constant} \quad (3.14)$$

where  $\gamma = \frac{c_p}{c_v}$ , is the ratio of specific heat capacities and for air it equals 1.4 [29]. We should note that this  $\gamma$  is different from that introduced in section 2.2.4.1, equation (2.6). The heat capacity at constant pressure  $C_p$  is a measure of how much energy is required to change the temperature of the fluid at constant pressure and its value is given in Table 3.1. Differentiation of (3.14) gives [32]:

$$\frac{1}{p_0} \frac{\partial \Delta p}{\partial t} = \frac{\gamma}{\rho_0} \frac{\partial \Delta \rho}{\partial t} \quad (3.15)$$

Manipulation of (3.15) and (3.12) gives:

$$\frac{\partial^2 \Delta p}{\partial t^2} = -\gamma p_0 \frac{\partial^2 v_x}{\partial t \partial x} \quad (3.16)$$

Differentiation of (3.13) with respect to  $x$  gives:

$$\frac{\partial^2 \Delta p}{\partial x^2} = -\rho_0 \frac{\partial^2 v_x}{\partial x \partial t} \quad (3.17)$$

By equating the cross differential terms in equations (3.16) and (3.17) the acoustic wave equation along the  $x$  direction is derived:

$$\frac{\partial^2 \Delta p}{\partial x^2} = \frac{1}{c_a^2} \frac{\partial^2 \Delta p}{\partial t^2} \quad (3.18)$$

where  $c_a = \sqrt{\frac{\gamma p_0}{\rho_0}} = \sqrt{\gamma RT_0}$ , and the subscript  $a$  denotes that the process is adiabatic. It is worth mentioning that the above mentioned speed of sound, derived by Laplace [33], is different to Newton's prediction which was based on the assumption that sound propagation is an isothermal process. At audible frequencies, however, the temperature gradients are low and hence, heat transfer is effectively zero. For air at room temperature  $c_a = 343 \text{ ms}^{-1}$ . According to Newton's derivation the speed of sound was predicted to take the value  $c_i = 245 \text{ ms}^{-1}$ , [33], where the subscript  $i$  stands for isothermal propagation.

The solution of (3.18) can be written as:

$$\Delta p(x, t) = \mathbf{A} e^{i(\omega t - k_x x)} \quad (3.19)$$

where  $\mathbf{A}$  is the complex peak amplitude of the wave,  $\omega = 2\pi f$  is the angular frequency and  $k = \frac{2\pi}{\lambda_0}$  is the wavenumber. Similarly, the particle velocity along x direction can be expressed:

$$v_x = \frac{\mathbf{A}}{\rho_0 c} e^{i(\omega t - k_x x)} \quad (3.20)$$

By adding in the other dimensions in equation (3.18) the three-dimensional acoustic wave equation is obtained:

$$\nabla^2 \Delta p = \frac{1}{c^2} \frac{\partial^2 \Delta p}{\partial t^2} \quad (3.21)$$

In terms of frequency this equation is written:

$$\nabla^2 \Delta p + \frac{\omega^2}{c^2} \Delta p = 0 \quad (3.22)$$

which is the Helmholtz equation. Once the scalar pressure is known, the density  $\rho$  can be recovered from the equation of state.

### 3.4 Sound propagation through a rigid-walled bound gas -Thermoviscous loss effects

As mentioned in the introduction to this chapter, viscous and thermal boundary layer effects play an important role to the description of sound propagation in cases where the propagation medium is in contact with a rigid boundary. This is because acoustic energy will gradually dissipate due to friction at the rigid boundary. In order to quantitatively describe the pressure wave in such conditions, the equation of state must be revisited. In order to account for the heat transfer that occurs between regions of high and low density as the pressure wave propagates, the energy equation is expressed as [34]:

$$\Delta \rho C_p \left( \frac{\partial T}{\partial t} \right) = -\nabla \cdot (-\kappa \nabla T) - \frac{1}{\rho} \left. \frac{\partial \rho}{\partial T} \right|_p T \frac{\partial p}{\partial t} \quad (3.23)$$

where  $\kappa$  is the thermal conductivity, a coefficient of proportionality between the temperature gradient and the heat flux in Fourier's heat conduction law. The quantity  $\left. \frac{1}{\rho} \frac{\partial \rho}{\partial T} \right|_p$  is the isobaric

coefficient of thermal expansion and relates to the ability of the fluid to expand when its temperature rises. It is often denoted as  $\alpha_p$  and its value is given in table 3.1. Another important parameter, used to describe sound propagation in cases where thermoviscous effects are not negligible is the bulk viscosity  $\eta_B$ , which is different to the shear viscosity  $\eta$ , described in section 3.3. The bulk viscosity is also known as the volume viscosity, the second viscosity, or the expansive viscosity, it is difficult to measure and is often seen to depend on frequency [35], [36]. It is related to the losses that appear due to the compression and expansion of the fluid and it appears in the Navier-Stokes equation:

$$\Delta\rho \left( \frac{\partial \mathbf{v}}{\partial t} + (\mathbf{v} \cdot \nabla) \mathbf{v} \right) = -\nabla \Delta p + \left( \frac{4}{3} \eta + \eta_B \right) \nabla (\nabla \cdot \mathbf{v}) - \eta \nabla \times \nabla \times \mathbf{v} \quad (3.24)$$

The Navier-Stokes equation is derived by combining equations (3.8), (3.9) and (3.10) and it contains the information necessary to predict turbulence, eddy currents and capillary flow. The  $\left( \frac{4}{3} \eta + \eta_B \right) \nabla (\nabla \cdot \mathbf{v})$  term accounts for viscous losses that occur within the fluid bulk and the term  $\eta \nabla \times \nabla \times \mathbf{v}$  accounts for losses that occur due to complex non-linear effects that occur near the rigid boundary which bounds the gas.

Finally, in order to present the complete set of thermoviscous acoustic equations, the isothermal compressibility parameter, denoted as  $\beta_T$ , is introduced. It relates changes in pressure to changes in volume in the fluid and is related to the usual (isentropic) compressibility  $\beta_S$  through the ratio of specific heats,  $\beta_T = \gamma \beta_S$ . As density fluctuates with temperature and pressure, the thermoviscous equation of state is:

$$\rho = \rho_0 (\beta_T p - \alpha_p T) \quad (3.25)$$

The values of the thermoviscous material parameters in the case that the sound propagation medium is low humidity air at temperature 19.5 °C, and at atmospheric pressure, are shown in Table 3.1. Note that the bulk viscosity is not zero, as air is a polyatomic gas and has translational, rotational and vibrational degrees of freedom. The translational degrees of freedom relax to equilibrium conditions relatively quickly and the process of such relaxation is represented by the dynamic viscosity coefficient. In contrast, the rotational and vibrational degrees of freedom have longer relaxation times, hence delaying thermodynamic equilibrium when excited, which results in attenuation. The bulk viscosity coefficient accounts for such

processes, but in the presence of a rigid boundary those processes do not play an important role. The rigid wall boundary can be considered an infinite heat sink that is at thermal equilibrium with the environment. Therefore, there is no significant delay for the air to come in a thermodynamic equilibrium state and in this thesis, the assumption that  $\eta_B = 0$  is made.

<b>Thermoviscous acoustic material parameter</b>	<b>Value</b>	<b>Units</b>
Background density, $\rho_0$	1.2	kg/m <sup>3</sup>
Dynamic viscosity, $\eta$	18.1	$\mu\text{Pa s}$
Bulk viscosity, $\eta_B$	0.6 $\eta$	$\mu\text{Pa s}$
Heat capacity at constant pressure, $C_p$	1005	J/(kg K)
Thermal conductivity, $\kappa$	28.5	mW (m K)
Isobaric coefficient of thermal expansion, $\alpha_p$	$3.4 \cdot 10^{-3}$	1/K
Isothermal compressibility, $\beta_T$	$9.87 \cdot 10^{-6}$	1/Pa

**Table 3.1** Summary of basic thermoviscous acoustic parameter values in low humidity air at temperature 19.5 °C and at atmospheric pressure.

Despite the fact that the losses due to internal molecular effects are negligible, the rigid boundary induces a thermal loss mechanism. As already mentioned in section 3.3, the pressure and density fluctuations arising from sound propagating in free space, generate an excess temperature  $\Delta T$ . This excess temperature, when in close proximity to the rigid wall (heat sink) is conducted into it; when it is far away in free space however, it is too insignificant in magnitude to be conducted to surrounding regions of fluid. Hence, the sound propagation can be considered as an adiabatic process in free space which evolves into an isothermal process close to the rigid wall. The temperature field within the distance over which this change occurs, can be described as a secondary thermal wave, whose full mathematical description is given in

references [33] , [37], [38], [39]. It is shown that combined field of the primary  $\Delta T$  and the secondary temperature waves can be written [39]:

$$\Delta T - T_0 = \left(1 - e^{(1+i)\frac{z}{\delta_\alpha}}\right) T_0 (\gamma - 1) \left(\frac{P}{\rho_0 c^2}\right) e^{i(\omega t - kx)} \quad (3.26)$$

where  $\gamma$  the ratio of specific heats,  $P$  the pressure amplitude of the plane wave,  $T_0$  is the temperature at equilibrium and  $\delta_\alpha$  the thermal boundary layer thickness which is a function of frequency  $f$ :

$$\delta_\alpha = \sqrt{\frac{a}{\pi f}} \quad (3.27)$$

where  $a = \frac{\kappa}{\rho_0 c_p}$ , is the thermal diffusivity of the gas. Note that the rigid wall is placed perpendicular to plane wave's wavefronts for this equation to hold, in other words, it is valid for sound incident at small angles from the parallel to the wall. On the contrary, when sound is incident normally to the wall, it is totally reflected as a result of the huge impedance mismatch between the two different mediums (air and solid). The definition of impedance will be given in the next section.

For sound at grazing incidence to the wall, in addition to the secondary temperature wave, a secondary viscous wave is also formed, arising from the no-slip boundary condition [40] which states that the particle velocity  $u_x$ , must fall to zero at the wall boundary, as shown in **Figure 3.2**, in which colour plot shows the velocity amplitude and vectors indicate the acoustic velocity vector at a fixed time.

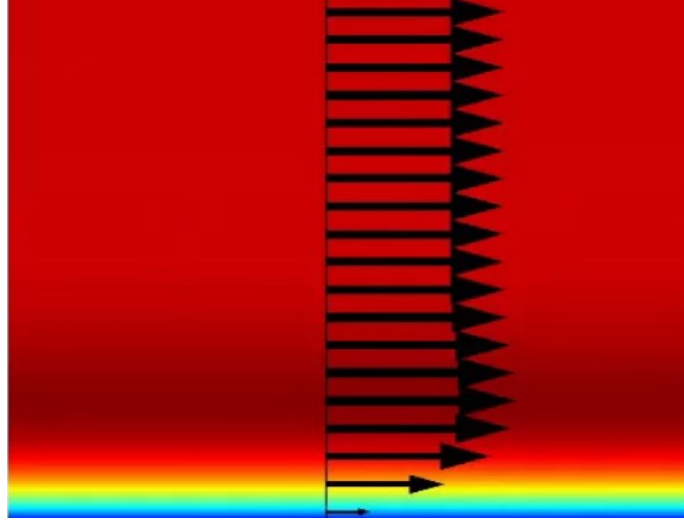


**Figure 3.2.** No slip condition at the horizontal boundary. Blue colour indicates that the velocity amplitude is zero. Dark red colour indicates maximum velocity amplitude. Taken from [41].

Note that the sound wave is considered as a time-harmonic wave propagating in the horizontal plane along a single rigid-wall, which could be, for example, a wave propagating in a small section of a pipe. The latter is part of the system that is investigated numerically and experimentally in this thesis; a rigid-walled cylindrical pipe. Because this system is of relatively small dimensions, the losses associated with the boundary layer become important. It has been shown [37] that losses can become more pronounced in the case of a rigid-walled cylindrical pipe compared to the single rigid-wall case which has been discussed up to this point.

The secondary viscous wave has its own particle velocity  $u'$  arising from the velocity field gradient, can be treated as part of the primary plane wave. The diffusion equation is written [39]:

$$\frac{\partial u'}{\partial t} = \frac{\eta}{\rho_0} \frac{\partial^2 u'}{\partial z^2} \quad (3.28)$$

The solution of the diffusion equation is:

$$u' = u_x e^{-(1+i)\frac{z}{\delta_v}} \quad (3.29),$$

where  $u_x$  is the solution of the acoustic wave equation along x direction for the lossless case (given in equation (3.20)) and  $\delta_v$  is the frequency dependent thickness of the viscous boundary layer, which is defined as:

$$\delta_v = \sqrt{\frac{2\eta}{\rho_0 2\pi f}} = \sqrt{\frac{\nu}{\pi f}} \quad (3.30)$$

where  $\nu$  is the kinematic viscosity (defined in section 3.3.) The square of the ratio between viscous and thermal boundary layers is known as the Prandtl number:

$$Pr = \frac{\delta_v^2}{\delta_\alpha^2} \quad (3.31)$$

In air the thermal and viscous effects are roughly equal in importance and the Prandtl number is 0.7. **Figure 3.3** shows calculated values of the thickness of the viscous and thermal boundary layers over a range of frequencies. It can be seen that for air at 5 kHz the viscous boundary layer thickness is  $\sim 20 \mu\text{m}$ , implying that the velocity gradient and hence the viscous loss are large at this distance from the rigid wall.

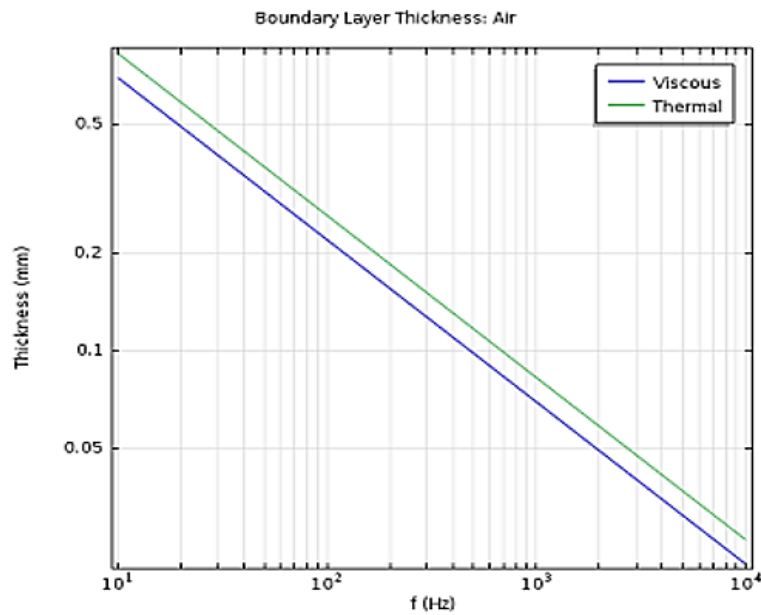


**Figure 3.3.** The value of the viscous (blue solid line) and thermal (green solid line) boundary layer thicknesses as function of frequency for air at 20°C and 1 atm. Taken from [41]

### 3.5 Sound propagation through a rigid walled cylindrical pipe

In order to describe sound propagation in a rigid walled pipe the assumption that the wavelength of sound generated by the source  $\lambda_0$  is large compared to the lateral dimensions of the pipe is made. Therefore a plane wave will propagate along the pipe, which will reflect at the far end of a pipe, will come back and reflect again giving rise to standing waves or resonances. Depending on whether the pressure of the returning wave is in phase or out of phase with the driving pressure, the measured impedance will be higher or lower compared to the impedance measured when reflections are absent. The characteristic acoustic impedance  $Z$  is the ratio of acoustic pressure  $p$  to acoustic volume flow  $U$ :

$$Z = \frac{p}{U} \quad (3.32)$$

where  $U = uA$ ,  $A$  being the cross section through which the wave passes. Equation 3.32 defines the characteristic acoustic impedance  $Z$ , but there are different kinds of acoustic impedances which will be introduced later on. One of those, is the specific acoustic impedance  $z$ , which relates pressure and velocity,  $u$ :

$$z = \frac{p}{u} \quad (3.33)$$

Hence, it follows that  $Z = \frac{z}{A}$ . This implies that when sound encounters a change in the cross-sectional area of the fluid, for example, at the time that it enters or exits a rigid-walled pipe, an impedance mismatch occurs at the pipe entrance or exit which causes reflections. There is hence a sum of waves travelling to the right and left and this gives standing waves and resonances. In order to gain deeper understanding on why impedance mismatch causes reflection (discussed in section 3.5.2), another kind of impedance, the radiation impedance,  $Z_{\text{rad}}$ , will be defined.

As pipes resemble musical wind instruments, we can think of the acoustic impedance as the acoustic response of the instrument for all possible frequencies. There are different techniques employed for measuring the acoustic impedance [42] and once this information is retrieved precisely the characterization of musical instruments is achieved. **Figure 3.4** presents the measured impedance spectra for the clarinet, the flute and the cylinder, each of which has an effective length of about 325 mm and diameter 15 mm.

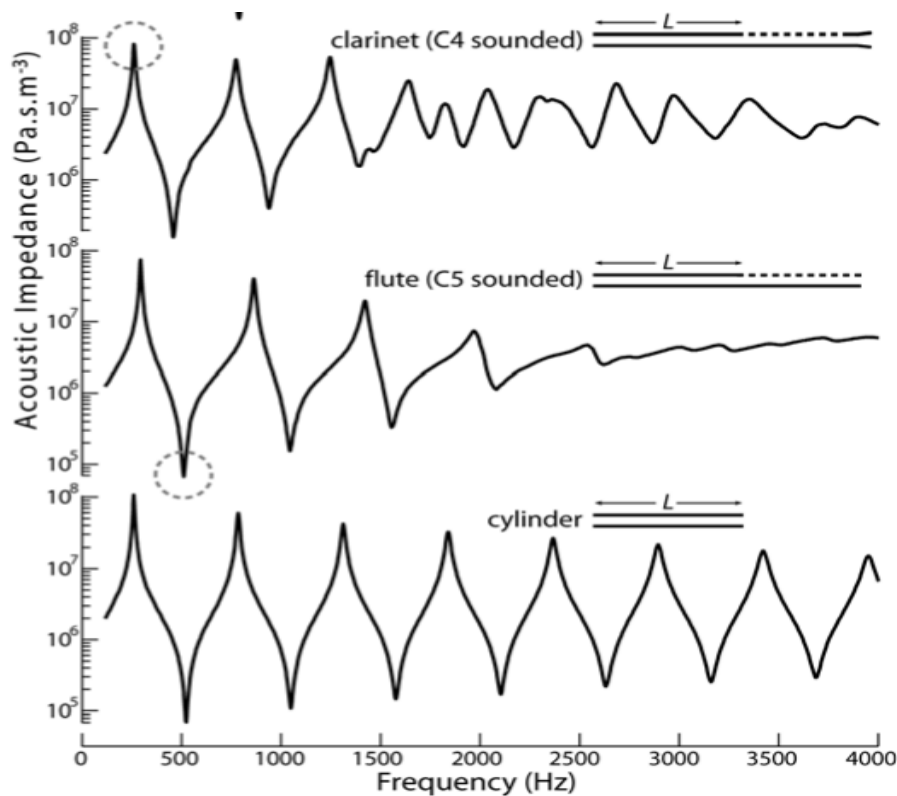


**Figure 3.4.** The acoustic impedance of (bottom to top) a simple cylinder (325 mm long, 15 mm in diameter), flute and clarinet. The circle indicates the maximum or minimum where each instrument operates. Modified from [43].

The maxima for the cylinder are at approximately  $(2n-1)(c/4L)$ , where  $L$  is the length of the cylinder, and the minima at  $n(c/2L)$  [43], where  $c = 343$  m/s, is the speed of sound in air at room temperature. The dashed circle highlights the first maximum of the acoustic impedance for the clarinet and the first minimum of the acoustic impedance for the flute. This is because the clarinet operates at *maxima* of  $Z$  and the flute at *minima* of  $Z$ . The flute, is played with the embouchure hole open to the atmosphere, so that the varying part of the acoustic pressure is zero. The acoustic flow is large, however, due to the jet of air between the player's lips. By taking into account the definition of the impedance, the operation at minima of  $Z$  for the flute is explained. In addition, by cross-comparing acoustic impedances of **Figure 3.4**, it can be deduced that the acoustics of an open rigid-walled cylindrical pipe is similar to the acoustics of a flute, and the acoustics of a closed rigid-walled cylindrical pipe is similar to the acoustics of a clarinet. Hence, the sound produced for the open and closed cylindrical pipes has frequencies:

$$f_{open} = n \frac{c}{2L} \quad (3.34)$$

$$f_{closed} = (2n - 1) \frac{c}{4L} \quad (3.35)$$

where  $n$  is integer. Substitution,  $n = 1$ , gives the frequency of the fundamental mode ( $f_{closed} = 263$  Hz,  $f_{open} = 527$  Hz), whereas for  $n$  greater than 1, the frequencies of higher harmonics are deduced. These equations also imply that the open pipe supports both odd and even harmonics whereas for the closed pipe, even harmonics are absent.

The boundary conditions for open and closed rigid-walled cylindrical pipes are shown in **Figure 3.5** and the pressure amplitude satisfying those boundary conditions is derived by solving the Helmholtz equations, when losses are ignored, and the Navier-Stokes equations, for the thermoviscous losses to be accounted for. In the case that the pipes have constant cross sections the solutions are written in terms of sine and cosine functions [43]

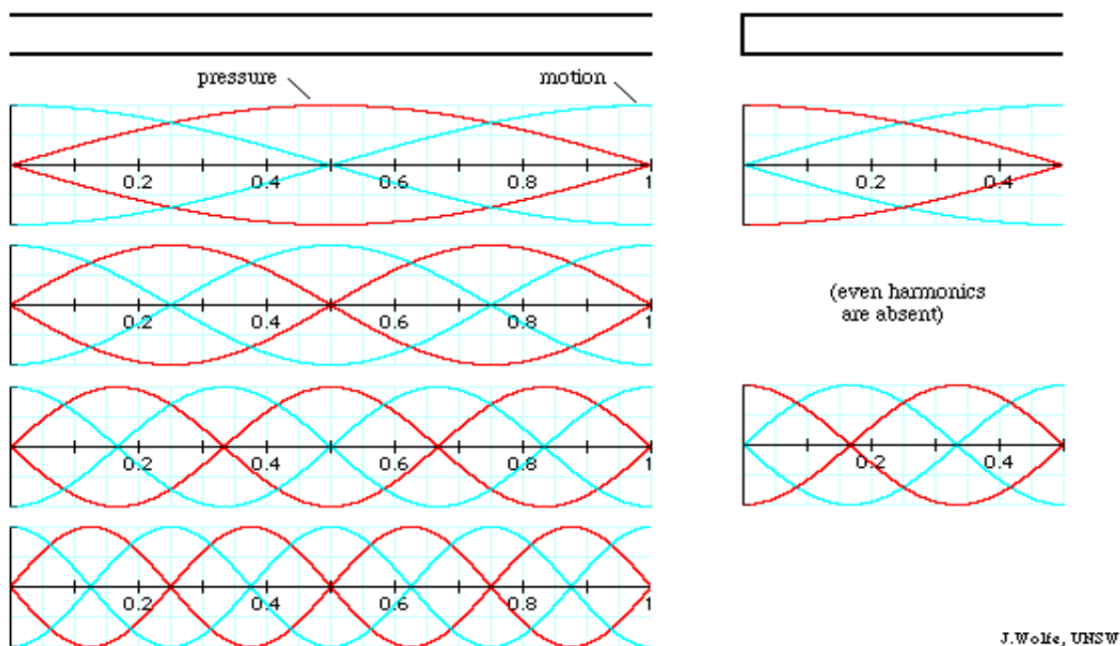


**Figure 3.5.** Variation in pressure (red) and variation in flow (blue) for an open and closed rigid walled cylindrical pipe. The frequency and wavelength are the same for the figures in each row. Taken from [44].

According to equations (3.34) and (3.35), the longest wavelength is twice the length of the open cylindrical pipe (upper left panel) and four times the length of the closed cylindrical pipe (upper right panel). Therefore, for the same frequency of sound to be produced, the length of the closed pipe must be one quarter of the length of the open pipe. The amplitude of the variation in pressure is shown in red and it is zero at an open end (pressure node), where the pressure is almost equal to the atmospheric pressure. At the closed end, the variation in pressure with respect to the atmospheric is maximum (pressure antinode). The amplitude of the variation of the flow of air is shown in blue. At an open end, this is maximum, because air can flow freely in and out, and at a closed end it is zero.

### 3.5.1 End effects and cut-off frequency

The resonant frequencies defined in Equations (3.34) and (3.35) are not valid in real problems unless a correction is made to take account of the fact that when the sound propagates to the open end of a pipe, it affects the pressure at the volume of air just outside the pipe. A related problem was first solved by William Strutt [45] who considered that a cylindrical oscillating piston (of area  $A$ ) lying in a large plane baffle has an effect on the air closest to the piston and just in front of it (of mass  $\rho V = \rho A \delta$ ); the air must move with the piston (due to its inertia) and the force required to move the air is

$$\mathbf{F} = m\mathbf{a} = \rho A \delta \frac{dv}{dt} \quad (3.36),$$

where  $\delta$ , is the height of the cylindrical air mass that is actually moving with the piston and  $v$  is the velocity of the piston. The position of the piston with respect to the plane of the baffle is:

$$\mathbf{x} = \mathbf{x}_m \sin \omega t \quad (3.37)$$

where  $x_m$  is the maximum amplitude of the oscillation. Differentiation of (3.37) and substitution to (3.36) gives:

$$\mathbf{F} = \rho A \delta (-\omega^2 \mathbf{x}_m \sin \omega t) \quad (3.38)$$

The acoustic flow at the surface of the piston is:

$$U = Av = \omega Ax_m \cos \omega t \quad (3.39)$$

Combining the definition of pressure,  $F=pA$  and the definition of impedance (3.32) the magnitude of the radiation impedance is obtained:

$$|Z_{rad}| = \frac{p}{U} = \omega \rho \frac{\delta}{A} \quad (3.40)$$

However, for the complete definition of  $Z_{rad}$ , the phase difference between the pressure and the flow must be included. An impedance can be characterized as inertive, in the case that the pressure is ahead of flow in phase or compliant, in the case that the pressure is behind of flow in phase. In complex notation, the inertive impedance is defined written as:

$$Z_L = j\omega\rho\frac{L}{A} \quad (3.41)$$

where  $j^2 = -1$ , and  $\rho$ ,  $L$ ,  $A$  are the density, length and area of the cylindrical fluid volume respectively, which is vibrating with frequency  $\omega$ , due to an acoustic pressure difference  $p$  applied across it. The inertive impedance  $Z_L$  is proportional to  $\omega$  because vibration at higher frequency requires greater acceleration and thus a greater acoustic pressure difference. The compliant impedance is written as:

$$Z_C = \frac{1}{j\omega C} \quad (3.42)$$

where  $C = V/\gamma P_{atm}$ . The adiabatic factor  $\gamma$ , has already been defined (see equation (3.14)). In this case, the cylindrical volume is closed at one end and an acoustic pressure is applied at the other end. The air in the confined volume acts like a spring and thus an increase in flow is necessary before the pressure increases much. Hence the pressure lags the flow in phase. The compliant impedance is inversely proportional to frequency, as vibration at a higher frequency has a shorter period, during which the amount of gas flowing in the cylindrical volume is smaller and thus it produces a smaller pressure.

The radiation impedance for the piston is inertive since the inertance of the air adjacent to the piston is responsible for the radiation pressure. For a piston in an infinite plane,  $\delta$  is  $0.85a$ , where  $a$  is the radius of the circular base of the cylindrical piston.

The example of the piston has been chosen as this system approximates the flow at an open cylindrical pipe, which is the basic component of the novel acoustics system investigated computationally and experimentally in this thesis. The accepted value for the so called end correction for an open pipe is  $\delta = 0.8a$  [39]. This means that the radiation inertance at an open end of the pipe gives it an extra length  $\delta$ , as illustrated in dotted line in **Figure 3.6**. The resonant frequency for the open pipe given in equation (3.34) after including end corrections is written:

$$f_n = \frac{nc}{2(L+\delta)} \quad (3.43)$$

The length of the open pipe in **Figure 3.6** is chosen so as to give the same resonant frequency as the flute pictured in the upper panel. The standing waves of the first two harmonics for the flute are shown by solid lined, and the analogy between the flute and the open pipe is obvious. It can be seen that both the standing wave pressure and the end effect increase with frequency. The pressure of the standing wave does not fall to zero at the first open tone hole because the inertance of the air in the open hole is not zero. The standing wave penetrates into the lattice and gets attenuated along the bore. In addition, according to (3.41) the inertive impedance increases with frequency and hence the relative amplitude of the propagating standing wave increases for higher harmonics. A high amplitude wave can thus “perceive” whether tone holes are open or closed. As a result, closing some of them, the so called fingering by the musicians, affects the resonant frequency as well as the length of the end correction.

However, for frequencies higher than the cut-off frequency all fingerings behave as though all the holes were closed. Consequently, the increase of the cut-off frequency of a musical instrument is desirable for better quality of sound to be produced. Below cut-off frequency the flute behaves approximately as an open tube terminated at the position of the first open tone hole as shown in **Figure 3.6**.

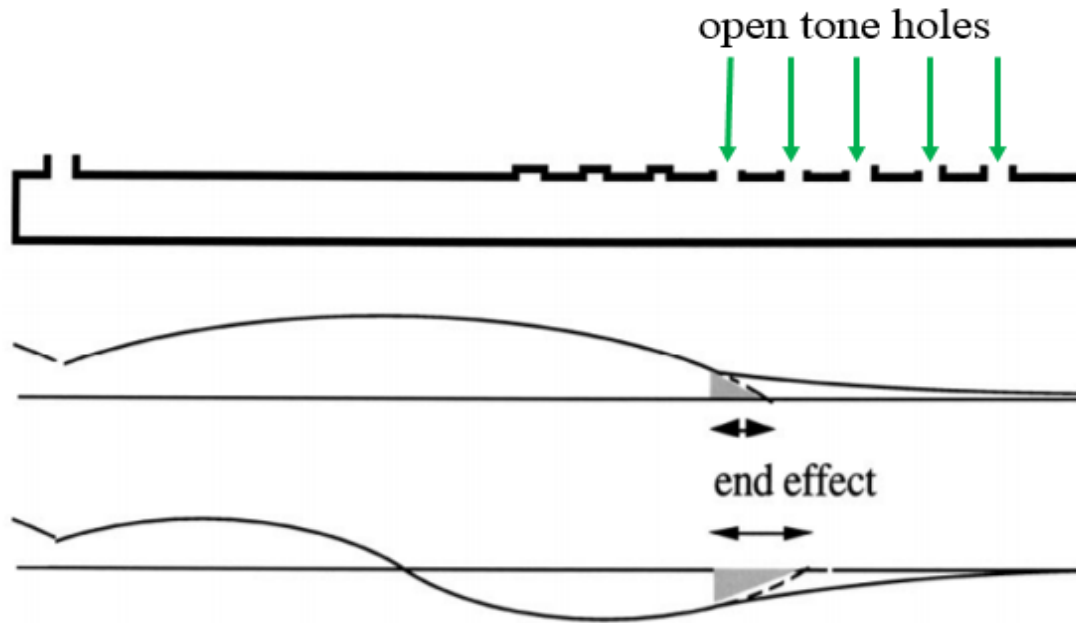


**Figure 3.6.** Acoustic pressure of the standing waves a) for the first two harmonics in the bore of a flute (solid line) and b) for the first two harmonics in a rigid-walled cylindrical pipe (dotted line). The cylindrical pipe length has been selected so as to give the same resonant frequency as the flute. Modified from [46].

The characteristics of the standing waves in the flute have been studied as a function of both position along the length of the bore and frequency [45], and have been compared to the impedance spectra to determine if the resonances observed are standing wave peaks. This occurs if the standing wave peaks and the impedance minima are equally spaced in frequency. The flute comprises of an array of holes connected via short sections of bore and thus resembles an acoustical transmission line comprising compliances and inertances. The theoretical expression for its cut-off frequency is given in [46]. The cut off frequency is determined by the cavity's exact shape and size as well as the properties of the fluid medium within it and must be calculated on an individual basis [39], [32]. The dimensions of the cavities comprising the samples in this thesis have been selected so that the frequencies of interest lie below each cavity's cut-off frequency.

### 3.5.2 Reflection coefficient

Assuming that the open pipe of **Figure 3.7** is very long, there are no reflections and thus the impedance of the pipe ( $x < 0$ ) is  $Z$ , as defined in equation (3.32). The impedance at  $x = 0$  is  $Z_{rad} = p_{rad}/U_{rad}$  if one looks at  $x > 0$ , and  $Z$  if one looks at  $x < 0$ . A sine wave travelling along the pipe towards the right generates pressure and flow fluctuations which can be written as:

$$p = p_{>} \sin(kx - \omega t) \quad (3.44)$$

$$U = U_{>} \sin(kx - \omega t) \quad (3.45)$$

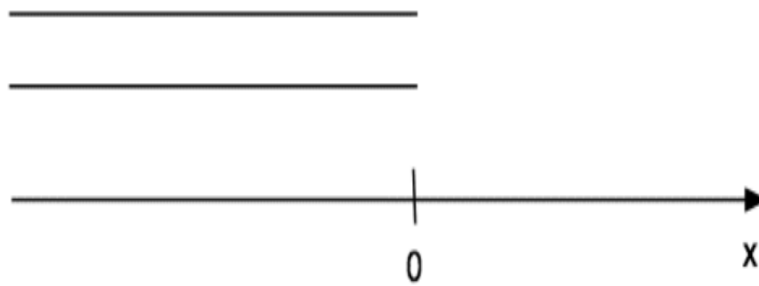


**Figure 3.7.** Schematic of a simple open pipe placed at  $x < 0$ .

Exactly at  $x = 0$ , continuity of pressure and continuity of flow cannot be satisfied considering only the wave towards the right and the radiated wave because the magnitude of  $Z$  is much greater than that of  $Z_{rad}$ . Hence, if we set the flows equal, the pressures cannot be equal. As expected, a reflection occurs at the end of the pipe. The reflected wave generates pressure and flow fluctuations travelling to the left and can be written as:

$$p = p_{<} \sin(kx - \omega t) \quad (3.44)$$

$$U = U_{<} \sin(kx - \omega t) \quad (3.45)$$

The continuity equations can be written as:

$$p_{>} + p_{<} = p_{rad} \quad (3.46)$$

$$U_{>} - U_{<} = U_{rad} \quad (3.47)$$

Substituting the definition of impedance in equation (3.47) gives:

$$\frac{p_{>}}{Z} - \frac{p_{<}}{Z} = \frac{p_{rad}}{Z_{rad}} \quad (3.48)$$

Combining (3.46) and (3.48) gives the reflection coefficient  $R$  at the end of the pipe:

$$R = \frac{p_{<}}{p_{>}} = \frac{Z_{rad} - Z}{Z_{rad} + Z} = -\frac{1 - \frac{Z_{rad}}{Z}}{1 + \frac{Z_{rad}}{Z}} \quad (3.49)$$

Except at very high frequencies,  $|Z_{rad}| \ll Z$  so the reflection coefficient is almost -1 and hence a reflection with a phase change of  $\pi$  occurs at the open end of the pipe. This explains the pressure node observed in **Figure 3.5**.

The aforementioned sort of cavity resonance is often referred to as “Fabry-Pérot like” since it can be thought as a resonance that occurs when reflecting waves interfere and form only standing waves of certain wavelengths, as in the classic Fabry-Pérot interferometer [47]. Fabry-Pérot intererferometry has been applied in a large number of disciplines [48],[49],[50] including as a remote sensing technique for probing the middle and upper atmosphere [51], and to observe ballistic electron propagation in graphene [52].

The way these Fabry-Pérot like cavities have been utilised so as to form trapped surface waves, and thus manipulate sound is discussed in Chapter 5.

### 3.6 Conclusions

It has been shown that one means of generating sound is a vibrating plate which causes pressure and density fluctuations in the volume of air adjacent to it. As a result, air molecules move leading to travelling compressions and rarefactions. Based on the assumptions that the unperturbed fluid is frictionless, has definite-valued and time independent thermodynamic variables, as well as that sound propagation is an adiabatic process, the unbound gas is fully described by the equation of state, the conservation of mass and the conservation of momentum, which are all combined to derive the acoustic wave equation. The acoustic wave

equation predicts that the speed of sound in air is 343 m/s. When sound waves interact with a rigid wall thermoviscous effects are accounted for in the Navier Stokes equation. Hence, for sound grazing a single rigid wall, the velocity of the particles is different to the one predicted by the lossless acoustic equation. Both viscous and thermal boundary layer thicknesses are inversely proportional to frequency. For sound grazing a rigid walled cylindrical pipe, the impedance mismatch at the open ends, due to the presence of an inertive impedance, results in reflection of the pressure wave with a phase change of  $\pi$ . Hence, standing waves with pressure nodes are formed in the pipe. The resonant frequencies of those standing waves are integer multiples of the fundamental mode, thus resembling the behaviour of the Fabry-Pérot interferometer. The inertive impedance at the open ends is also responsible for the end corrections at the resonant frequencies of the standing waves. When Fabry-Pérot like resonators are arranged periodically so as to form an array, a trapped surface wave is formed due to those end corrections, and this is the focus of the Chapter 5.

## CHAPTER 4

### Simulations and modelling methods

#### 4.1 Introduction

It is well known that the laws of physics for space and time dependent problems are usually expressed in terms of partial differential equations (PDEs). However, these PDEs cannot be solved with analytical methods for the vast majority of geometries and problems. Instead, an approximation of the equations can be constructed, typically based upon different types of discretizations. The modified equations are often called weak formulations and the next step is the discretization of those equations. This chapter describes those methods, as well as the settings used in the FEM (finite element modelling) package, COMSOL®, in order to implement frequency domain, time domain and eigenfrequency models.

#### 4.2 Discretization

Assuming that a function  $u$ , is approximated by a function  $u_h$ , the approximation can be written as a linear combination of basis functions  $\psi_{iR,L}$ , shown in **Figure 4.1 (a)**, according to the following expression:

$$u_h(x) \approx a_{1L}\psi_{1L}(x) + a_{1R}\psi_{1R}(x) + a_{2L}\psi_{2L}(x) + a_{2R}\psi_{2R}(x) + \dots \quad (4.1)$$

where  $a_{iR,L}$  denotes the coefficients of the approximate function. **Figure 4.1 (b)** illustrates a discretization that can be chosen for the function  $u$  (shown in solid black line). The domain where the function  $u$  is defined, is divided into four evenly spaced sub-intervals, or mesh elements, bound by five nodal points  $x = 1, 2, 3, 4, 5$ . The approximate function  $u_h$  is shown in cyan color and it can be seen that it is discontinuous across the boundary between adjacent mesh elements. However, the approximation can be simplified, if the coefficients are constrained so that the solution is continuous across boundaries between adjacent elements.

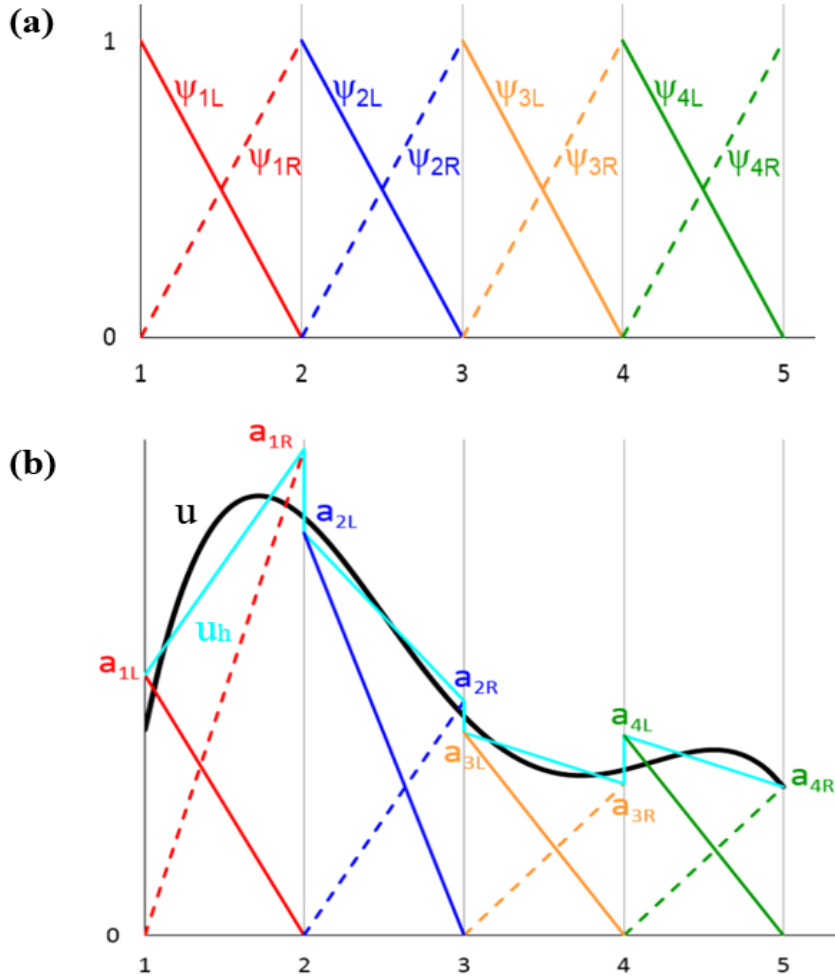


**Figure 4.1** (a) Vertical lines divide the domain in four evenly spaced mesh elements. In each mesh element, there are two basis functions represented by a solid line and a dashed line. (b) The function  $u$  (solid black line) is approximated with  $u_h$  (solid cyan line), which is a linear combination of the basis functions  $\psi_{iR,L}$  shown in (a) The coefficients are denoted by  $a_{iR,L}$ , where  $i=1,2,3,4$ . Taken from [53]

The constraint imposed on the coefficients results in introducing a new set of basis functions which are written as:

$$\begin{aligned}
 \varphi_1(x) &= \psi_{1L}(x) \\
 \varphi_2(x) &= \psi_{1R}(x) + \psi_{2L}(x) \\
 \varphi_3(x) &= \psi_{2R}(x) + \psi_{3L}(x) \\
 &\vdots
 \end{aligned}
 \tag{4.2}$$

Therefore, each new basis function is essentially a triangular-shaped, piecewise-linear function centered around a nodal point.

Another type of discretization where the elements are non-uniformly distributed over the  $x$  axis, different basis functions, or a larger number of elements could have been chosen, implying that the finite element method offers great freedom in the selection of discretization depending on the problem at hand.

### **4.3 The Finite Element Method from the Weak Formulation: Basis Functions and Test Functions**

In order to obtain the weak form of a PDE, the equation of interest is multiplied by a test function, integrated over the computational domain and the boundary conditions are imposed. The dependent variable is then expressed as a linear combination of basis functions, as already described in section 4.2. In the so called Galerkin method [54], the test function is set equal to a basis function and the solution are assumed to belong to Hilbert space, which is an infinite-dimensional function space with functions of specific properties. These functions can be conveniently manipulated in the same way as ordinary vectors in a vector space. For example, you can form linear combinations of functions in this collection and you can measure the angle between the functions, just like Euclidean vectors. Hence, the mathematical model equations, can be discretized to obtain the numerical model equations. It is worth mentioning that there is a close relationship between the numerical formulation and the weak formulation of the PDE problem as the theory provides useful error estimates when the numerical model equations are solved on a computer.

#### **4.3.1 System matrix and meshing**

Once the weak form of a PDE is obtained and the dependent variable is discretised, the matrix form of the resulting equation can be written as:

$$Au_h = f \tag{4.3}$$

where  $u_h = \{u_1, \dots, u_i, \dots, u_n\}$  is a vector of unknowns,  $A$  is a  $n \times n$  matrix and contains the coefficients of  $u_i$ ,  $f$ , is the source vector of dimension 1 to  $n$ . Matrix  $A$  contains products of the test functions and basis functions which belong to the same set. The test functions, can be prescribed at our convenience and the basis functions (or elements) can be defined in many different ways (infinitely many, in theory) as already discussed in section 4.2. For 2D/3D linear functions, the basis functions are expressed as functions of the position of the nodes ( $x$  and  $y$  or  $x, y, z$  respectively). The most common elements are illustrated in the **Figure 4.2 (a)** below. The mathematical description of the triangular element has already been given in equation 4.2.

It is worth noting, however, that the basis functions may not be linear, in which case the corresponding elements are second order and the edges and surfaces are curved. These element types are called Langrangian or serendipity. An example of Langrange elements used for quadratic basis functions are shown in **Figure 4.2 (b)**.

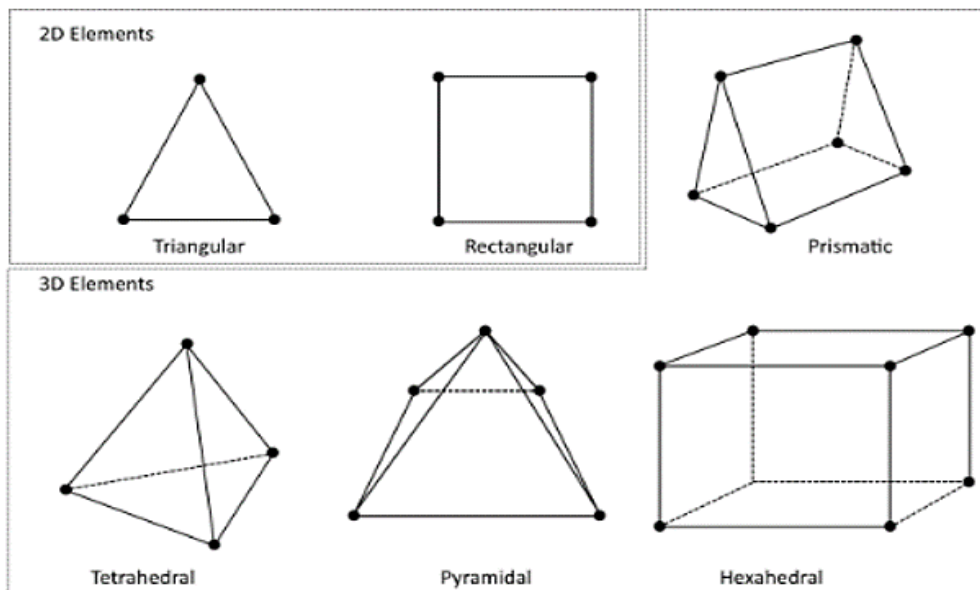


**Figure 4.2 (a)** Node placement and geometry for 2D and 3D linear elements.

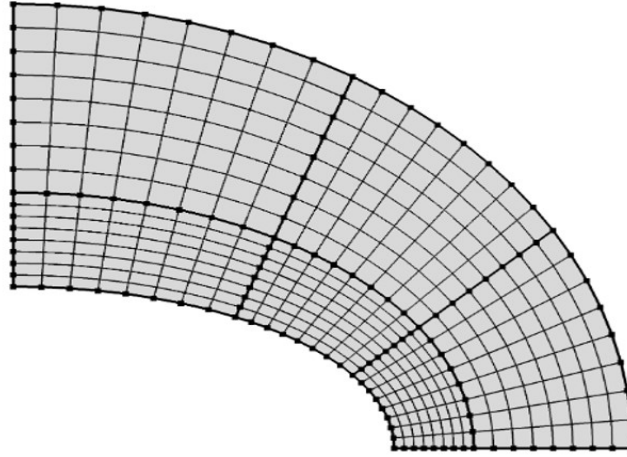


**Figure 4.2 (b)** Rectangular elements used for the quadratic base functions.

The problem is, in essence,

$$u_h = [A]^{-1}f \quad (4.4)$$

The system matrix  $A$  becomes sparse, with the above-mentioned selection of test function according to the Galerkin method. The solution of the system of algebraic equations gives an approximation to the solution to the PDE. The denser the mesh, the closer the approximate solution gets to the actual solution.

If we suppose that the mathematical model equation (PDE) is the inhomogeneous acoustic wave equation,

$$\left(\nabla^2 - \frac{1}{c_0^2} \frac{\partial^2}{\partial t^2}\right) u(x, t) = f(x, t) \quad (4.5)$$

and the geometry is a duct shown in the **Figure 4.3 (a)** below, the solution of the matrix form gives the instantaneous pressure at the nodes  $1, \dots, n$ , illustrated in **Figure 4.3 (c)**. **Figure 4.3 (b)** shows the discretization and **Figure 4.3 (d)** shows the interpolated instantaneous pressure in duct, using quadratic Lagrange interpolating polynomials.

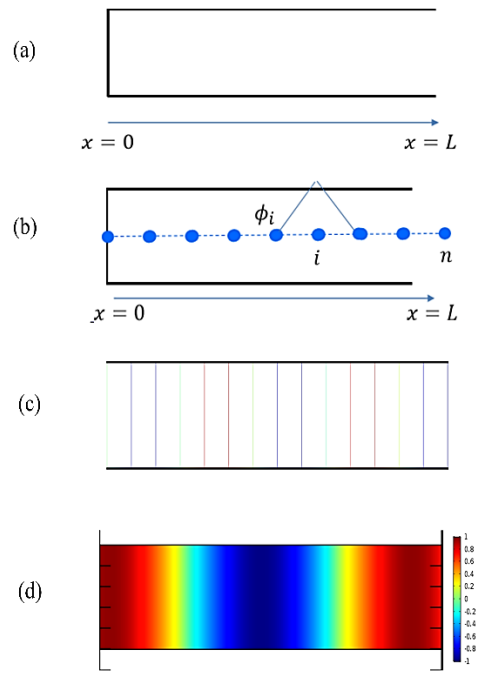


**Figure 4.3** (a) Duct of length  $L$ . (b) Discretization using basis function  $\phi$ . (c) Instantaneous pressure at the nodes. (d) Interpolated instantaneous pressure in duct. Taken from [55].

The FEM implementation method is summarized in the following flow diagram:

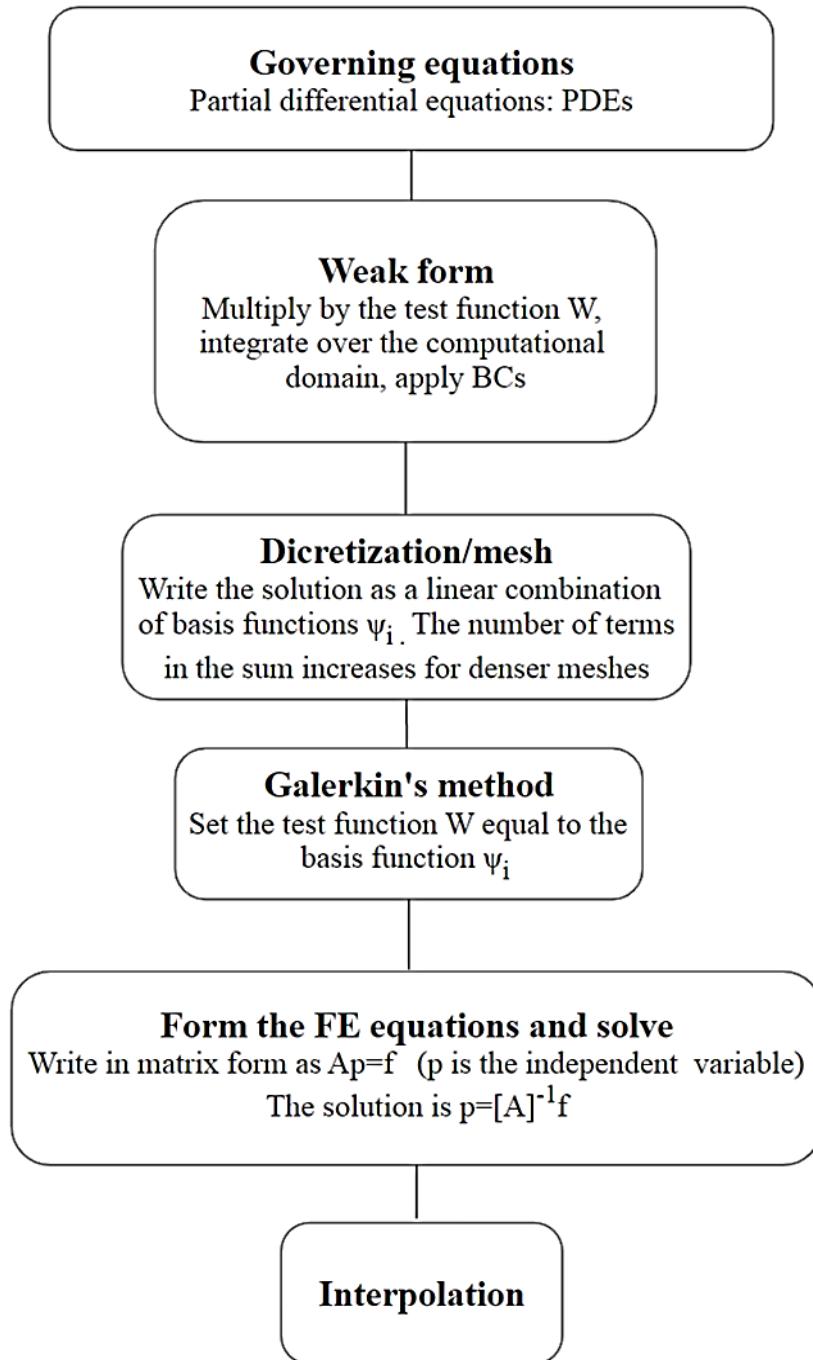


**Figure 4.4** Flowchart of the finite element analysis summarizing section 4.3.

#### 4.4 COMSOL®-Module and solver selection

The FEM software used in this work is COMSOL®, versions 5.4 to 5.5. COMSOL® is a software package that uses application specific modules such as the solid mechanics module, electrostatics module, pressure acoustic module and many others. All modules include the equations that define the system matrix discussed in the previous section. In the case that different physics and hence different sets of equations apply simultaneously, the coupling between different modules can be used to simulate the coupled physics. Once the spatial dimension investigated is selected, which can be 2D, 3D or 2D axisymmetric, the geometry is constructed, and material properties are applied to each subdomain of the geometry. Depending on the problem to be solved, the dependent variables are selected via choosing the appropriate module. In this work we are interested in the displacement field throughout the solid and the module which contains equations of this variable is the solid mechanics module. Since the material that is used, lithium niobate is piezoelectric, the second dependent variable in the models used is voltage. In models simulating sound in air the dependent variable is pressure. The computational algorithm used to calculate these variables at each point in the computational domain is often referred to as solver. COMSOL® has several different solvers, classified as either direct or iterative. Direct solvers compute solutions in a single large step whereas iterative solvers arrive at a solution in a number of steps,  $n$ . The most time efficient solver for the sound in solids and sound in air problems investigated in this thesis, was found to be the MUPS (MULTifrontal massively Parallel Sparse *direct solver*) direct solver.

#### 4.5 Study selection – Frequency domain

In mathematical modelling, the values of dependent variables depend on the values of independent variables. In the case that we want to investigate how the dependent variable, displacement field, is affected by the change in frequency, a frequency domain study is selected. The independent variable, frequency, is changed via a parametric sweep, and the solver calculates the value of the dependent variable in the desired range of frequencies.

##### 4.5.1 The geometry of model simulating SAW device

The 3D plane geometry of the SAW device shown in **Figure 4.5**. The width of the geometry  $W$  is set as the pitch of the PnC, i.e.  $10.9 \mu\text{m}$ . The IDT electrodes (see section 2.2.2 for details)

lie on a LiNbO<sub>3</sub> substrate of length  $L$ ,  $15\lambda$ , and depth  $D$ ,  $3\lambda$ , where  $\lambda$  is the wavelength of the excited SAW. The device is terminated with perfectly matched layer (PML), shown in blue, of width  $2\lambda_{\text{SAW}}$ , to avoid reflections at the edges. The PnC geometry is infinite in the in-plane direction perpendicular to the propagation direction, as periodic boundary conditions are applied on the two boundaries, shown in **Figure 4.5**. In the frequency domain study, the geometry scales with the SAW frequency, as a prerequisite for SAW excitation is the electrode pitch to be  $\lambda/4$ . A scaled substrate length  $L$ , means that for each frequency calculated, the distances between the PnC and the other domain features are always the same integer values of  $\lambda$ . Scaling  $D$  means that the substrate is always deep enough for the SAW depth profile not to leak into the PMLs.

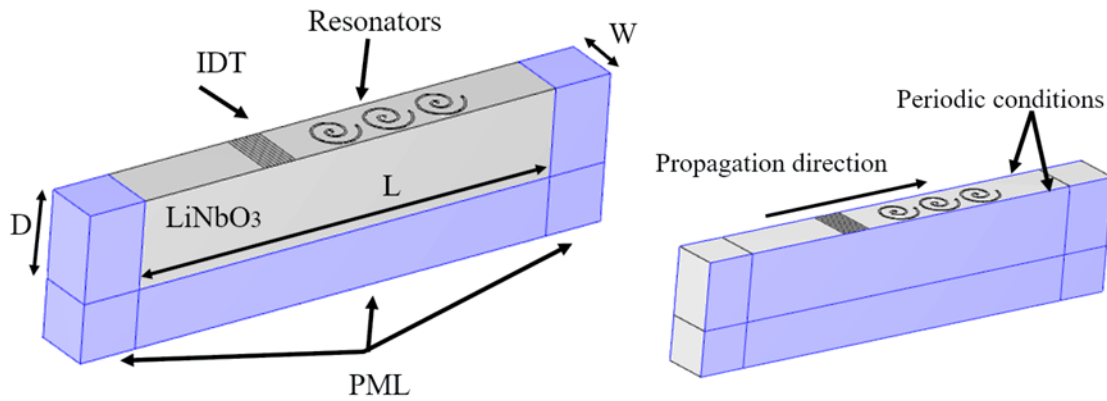


**Figure 4.5.** Frequency domain geometry schematics showing the SAW excitation source and resonators, substrate dimensions, PML subdomains, propagation direction and boundaries where periodic conditions are applied.

#### 4.5.2 Perfectly matched layers

In practice the entire space cannot be modelled and computational models have to be truncated for the outgoing waves to pass through with minimal reflection. Radiation boundary conditions, perfectly matched layers and boundary element method are different options in COMSOL® to minimise reflections but in this thesis perfectly matched layers are used. PMLs are virtual domains which correspond to a coordinate transformation, where a complex coordinate stretching is applied in a given direction [55], [56]. Ideally, the real term kills the wave before it hits the end of the PML. Optimisation of 3 parameters is required for an effective PML.

Those parameters are the typical wavelength,  $\lambda$ , the PML scaling factor  $p$ , and the PML curvature parameter  $s$ . For stretching applied to the  $x$  direction, the polynomial scaling is defined as

$$x = x_0 + s\lambda\varepsilon^p(1 - i), \quad (4.6)$$

where  $\varepsilon \in [0,1]$ . Although there are other types of stretching, for example the rational stretching, only polynomial stretching is used in this work and the optimised parameters are  $\lambda = \lambda_{\text{SAW}}$ ,  $p = 0.575$  and  $s = 1.5$ . The displacement rms field is defined as  $\frac{1}{\sqrt{2}}\sqrt{A_x^2 + A_y^2 + A_z^2}$ , where  $A_x, A_y, A_z$  is the amplitude of the displacement field in the  $x,y,z$  direction respectively. As shown in the **Figure 4.6** below, it is eliminated at the end of the PML, implying minimal reflections.

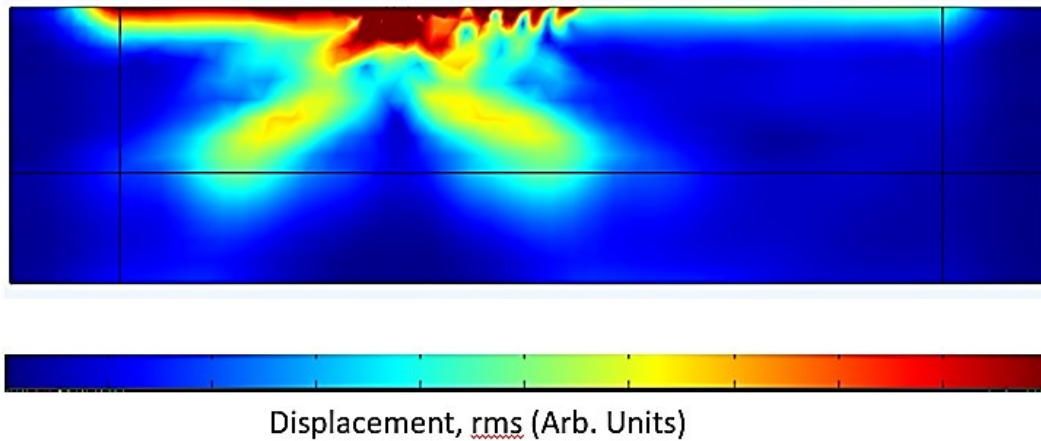


**Figure 4.6.**  $xz$  plane of the computational domain shown in previous picture. Displacement is zero on the end of the PML on both sides of the domain.

### 4.5.3 Multiphysics settings

In domain settings, the electrostatics and the solid mechanics module are applied to whole computational domain shown in **Figure 4.6**. In the solid mechanics settings, the whole geometry is declared as piezoelectric. The piezoelectric effect is therefore simulated via coupled solid mechanics and electrostatics interfaces. Since piezoelectricity is a result of anisotropy, the principal crystallographic axis, shown in **Figure 2.4** are defined in the definitions section. PMLs are also applied in this section. Input voltage 1 V is applied to first, third and fifth electrodes whereas the second and fourth electrodes are grounded.

#### 4.5.4 Mesh settings

The entire computational domain is divided into small parts for meshing. Tetrahedral mesh is applied to whole domain, a part of which is shown in blue in the **Figure 4.7** below.

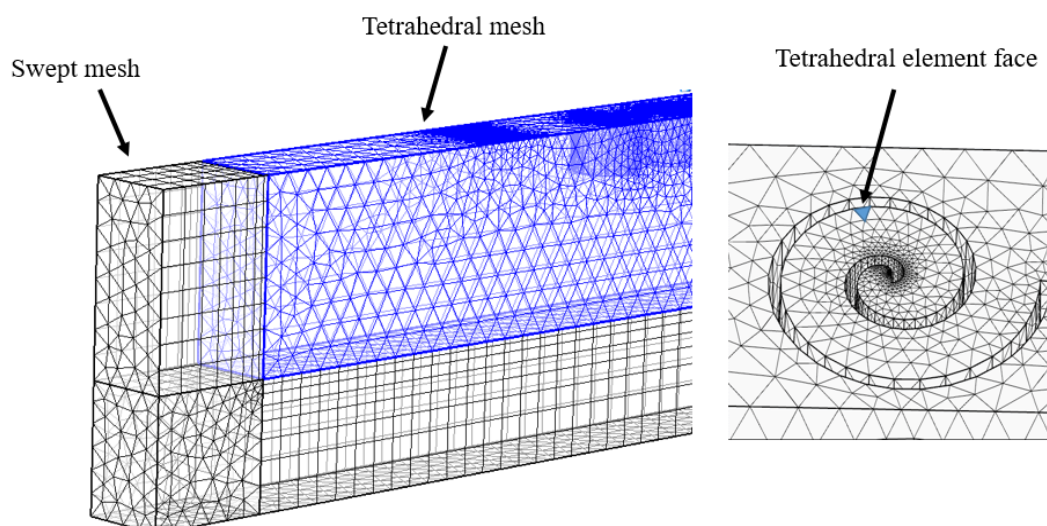


**Figure 4.7.** Meshing details for the structure shown in the previous **Figure 4.6**. Left panel: Tetrahedral mesh is applied to the main domain and swept mesh is applied to the PML. Right panel. Mesh in the area of the resonator with the face of the tetrahedral element highlighted in blue.

Then the PML is meshed under swept meshing. As shown in the left panel of **Figure 4.7**, the swept mesh starts at the boundary between the main domain and the PML and sweeps along to as specified destination boundary. Swept meshing is a powerful technique for minimising computational complexity and in the present model it is applied since there is no variation in each specific direction along which the PML extends. The SAW wavelength needs to be resolved and in geometries consisted of small edges, as the one shown in the right panel of **Figure 4.7**, more elements are added at those locations. The average edge size in our COMSOL® model is  $h = \lambda_{\text{SAW}}/10$  in the area where there is no necessity to resolve small geometrical element, although in the starting point of the resonator the edge size is smaller than  $\lambda_{\text{SAW}}/1000$ . A tetrahedral element face is highlighted in blue color in the right panel of **Figure 4.7**.

#### 4.6 Study selection – Time domain

In order to investigate the time evolution of the dependent variables, a time domain study is selected. The input signal and transducer response deduced by the time domain study were described in Chapter 2 section 2.2.4.2. Because we were interested only in the transducer response, the computational domain did not include resonators. Therefore, there was no need to apply periodic conditions in the geometry, which is shown in **Figure 4.8**.

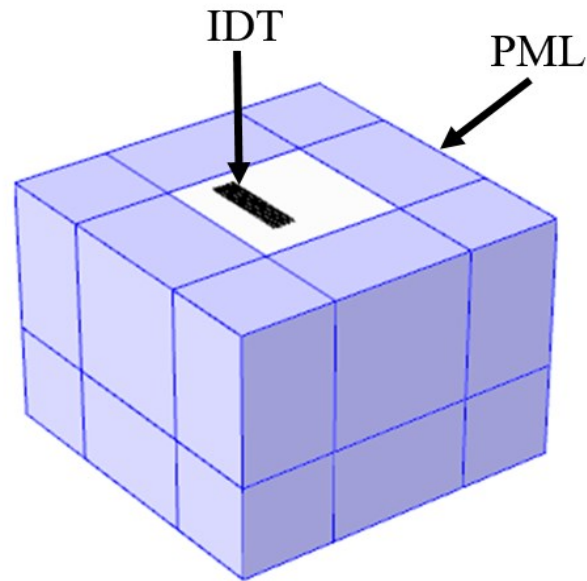


**Figure 4.8.** Computational domain used in the time domain study. PMLs surrounding the piezoelectric slab are illustrated in blue.

The basic differences compared to the frequency domain model is the PML width, which is now  $10\lambda_{\text{SAW}}$  and the number of the swept PML layers which is set to 8 . Since the equations of motion, described in Chapter 2 (Equations 2.32, 2.33) contain second order derivatives in time, the time stepping method used is Generalized alpha, which was first suggested in 1993 for second order systems of structural mechanics [57].

#### 4.7 Study selection – Eigenfrequency model for sound in solid

Considering the description of the frequency and time domain models, SAW generation is a result of electroelastic coupling between an IDT transducer lying on a surface free of stresses and charges, and a lithium niobate piezoelectric substrate. However, SAWs can also arise from

the interaction of elastic waves with the free surface, an example being Rayleigh waves propagating along the surface of the earth. Another example, is Rayleigh waves propagating in  $\text{LiNbO}_3$  and the latter is examined in this section.

In order to clarify the apparent velocity,  $c_R$ , of a Rayleigh wave propagating in  $\text{LiNbO}_3$ , an eigenfrequency analysis was performed. For input wavelength components  $k_x = \frac{\pi}{\alpha}$ ,  $k_y = 0$ , corresponding to the Brillouin zone border in the  $\Gamma X$  direction of a square lattice (lattice constant  $\alpha = 10.9 \mu\text{m}$ ), three eigenfrequencies calculated by the COMSOL® models are shown in **Figure 4.9**, in descending frequency order.

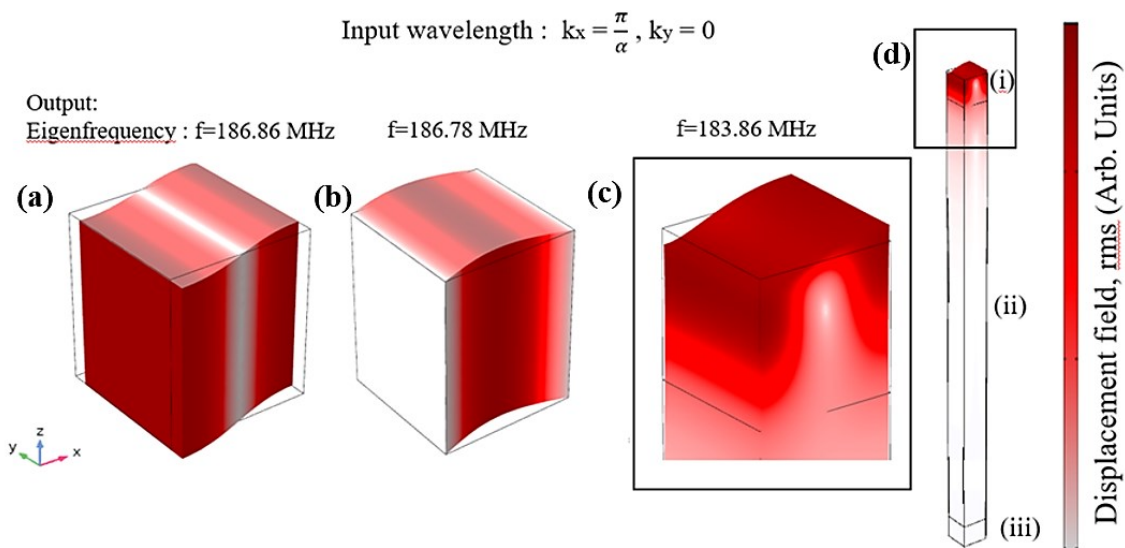


**Figure 4.9.** (a) Unit cell schematic showing geometry and displacement field at eigenfrequency  $f = 186.86 \text{ MHz}$ . (upper frequency bulk mode); (b) Unit cell schematic showing geometry and displacement field at eigenfrequency  $f = 186.78 \text{ MHz}$ . (lower frequency bulk mode). (c) Detail of the unit cell shown on (d), illustrating displacement field at eigenfrequency  $f = 183.86 \text{ MHz}$ . (d) Unit cell used to calculate Rayleigh SAW phase velocity. At the top of the geometry (i) the displacement field presents higher values compared to the extended bulk domain (ii) and the perfectly matched layer (iii).

The first two panels from right to left show the displacement field for the bulk modes, whereas the right panel shows the displacement field for the Rayleigh SAW wave. Two different models were used to obtain those graphs. For the bulk waves, a cubic unit cell of length  $\alpha$  and periodic conditions at all boundaries; for the Rayleigh SAW, the computational domain consists of 3 separate regimes. The top (i) is the active domain, where the finite depth phononic crystal is usually placed, but in order to calculate the Rayleigh SAW velocity before the interaction with the PnC, the domain is blank. This domain is typically tuned to be around an order of magnitude deeper than the pitch of the photonic crystal. The middle (ii) is the bulk domain, tuned to be around at least 10 times the PnC pitch, for the solutions to converge as shown in [58]. The bottom regime (iii) is the perfectly matched layer. The setup for the simulation of Rayleigh SAWs is adopted from Assouar et al. [59]. For the selected value of wavevector  $k_x = \pi/\alpha$ , the phase velocities for the bulk modes are  $v_{ph,1} = \omega/k_x = 2\pi f/(\pi/\alpha) = 2f\alpha \cong 4073$  m/s and  $v_{ph,2} \cong 4071$  m/s, where  $v_{ph,1}$  and  $v_{ph,2}$  correspond to the phase velocities of the modes shown in **Figure 4.9**. Due to the lower eigenfrequency calculated for the Rayleigh wave compared to the bulk waves at certain wavelength, it can be deduced that the phase velocity is also smaller compared to the bulk modes,  $v_{ph,R} = 4002.8$  m/s. Hence, there is no large deviation from the theoretical value of 4000 m/s, obtained by the method discussed in section 2.3.8. Besides, in section 2.2.3, it was explained that for velocities around 4000 m/s, maximum piezoelectric coupling is achieved. But for the SAW to propagate with this velocity, the correct crystallographic axis needs to be assigned to the material, which is declared by setting the 2<sup>nd</sup> Euler angle at -0.663 radians and the 1<sup>st</sup> and 3<sup>rd</sup> Euler angles at zero radians in the definition section in COMSOL®.

In order to calculate phase velocities at different values of excitation wavevectors from the ones mentioned above, a parametric sweep in wavevectors was performed. However, as shown in **Figure 2.7** section 2.2.4.1, the solutions repeat beyond a certain interval and therefore, the parametric sweep is limited within the first Brillouin zone, as defined by the geometry. For a square lattice, the reciprocal lattice vectors orientations and absolute values are described in **Figure 4.10**. In order to calculate solutions along the  $\Gamma X$  direction  $k_y$  is fixed at zero and  $k_x$  spans from 0 to  $\pi/\alpha$ . For the solutions along  $XM$  direction  $k_x$  is fixed at  $\pi/\alpha$  and  $k_y$  ranges from 0 to  $\pi/\alpha$ . Finally, since the irreducible Brillouin zone forms an equilateral triangle, solutions along  $\Gamma M$  directions are found if  $k_x$  is set at the same value as  $k_y$ , with the value being in the range from 0 to  $\pi/\alpha$ . The study searches for solutions around 0 Hz and the eigenfrequencies for different combinations of  $k_x$  and  $k_y$  are calculated. The derived solutions, the so called

dispersion relations (not shown here), are linear, indicating that phase velocities are independent of frequency for both bulk waves and the Rayleigh SAW. Except from the dispersion relations, the dependent variables, which are the displacement field and the electric potential are also an output of the calculation. Hence, their values are known at every single point inside the unit cell. The calculated displacement at those points is denoted as  $\mathbf{u}_{src}$  and the position vector is denoted as  $\mathbf{r}_{src}$ . The Floquet boundary condition applied to the unit cell is expressed as:

$$\mathbf{u}_{dst} = \mathbf{u}_{src} e^{-\mathbf{k}_F \cdot (\mathbf{r}_{dst} - \mathbf{r}_{src})} \quad (4.7)$$

where  $\mathbf{u}_{dst}$  is the displacement,  $\mathbf{k}_F$  is the wavevector given by:

$$\mathbf{k}_F = k_x \hat{\mathbf{x}} + k_y \hat{\mathbf{y}} + k_z \hat{\mathbf{z}} \quad (4.8)$$

The position vector at any point in space is denoted as  $\mathbf{r}_{dst}$ . The displacement  $\mathbf{u}_{dst}$  can be therefore calculated by using equations (4.7) and (4.8).

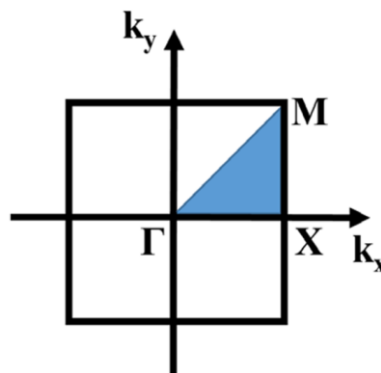


**Figure 4.10.** Blue triangle denotes the irreducible Brillouin zone of the square lattice.  $\Gamma X = XM = \frac{\pi}{\alpha}$ ,  $M\Gamma = \sqrt{2} \frac{\pi}{\alpha}$

#### 4.7.1 Mesh settings

The mesh used in these simulations is free tetrahedral in subdomain (i) (**Figure 4.9**), with maximum element size  $\alpha/8$ , and swept meshes in subdomains (ii) and (iii) with  $\alpha/2$  maximum element size in subdomain (ii) and a six element distribution in the perfectly matched layer (iii).

## 4.8 Study selection – Eigenfrequency model for sound in air

### 4.8.1 The geometry of model simulating ASW device

In order to model an acoustically rigid solid material bounding fluid cavities the geometry shown in **Figure 4.11** was used. Along the depth of the domain there are 5 separate regimes. The middle regime (i) simulates the fluid cylindrical cavities arranged in a honeycomb configuration perforated through an acoustically rigid plate. The sound hard boundaries are indicated in red arrows. In the direction normal to those boundaries the material is either acoustically rigid or air. The regime (i) is zoomed in, in the right panel of **Figure 4.11** and the cylindrical cavities filled with air can be seen. The fluid-solid interfaces are shown in purple color. Regimes (ii (a)) and ii (b) simulate the air with losses taken into account whereas regimes (iii (a)) and (iii (b)) simulate the air without losses. Loss causes a small (approx. 0.5 kHz) reduction in the frequency of the modes at the Brillouin zone when compared a loss-less system.

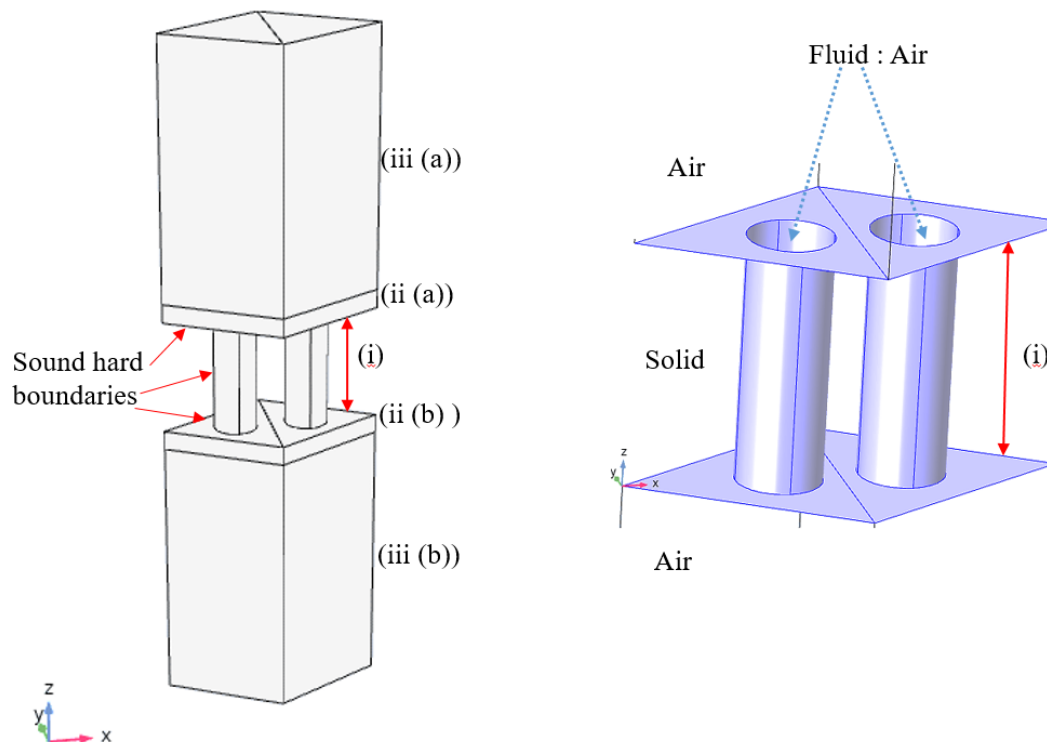


**Figure 4.11.** Unit cell schematic showing geometry of a model simulating an acoustically rigid material bounding fluid cavities arranged in a honeycomb configuration. Subdomain (i) is the

active subdomain including the PnC structure, (ii (a)) and (ii (b)) are the subdomains simulating the air above and below the PnC slab, with losses taken into account, (iii (a)) and (iii (b)) are the subdomains simulating the air above and below the PnC slab, without losses taken into account.

#### **4.8.2 Multiphysics settings**

In domain settings, the thermoviscous acoustic module, which solves the frequency domain linearized Navier-Stokes, continuity and energy equations, is applied to domains (i), (ii (a)) and (ii (b)). The dependent variables are pressure, velocity and temperature. The pressure acoustics module, which solves the Helmholtz equation is applied to the rest of the domains. The coupling between those modules is applied to the appropriate interfaces and Floquet periodic boundary conditions are applied to the parallel faces of the rhombic unit cell in order to simulate an infinite honeycomb surface. The material parameters and explanations will be given in Chapter 3, along with the basic equations describing sound propagation in air.

#### **4.8.3 Mesh settings**

The mesh used in regime (i) is shown in **Figure 4.12** below. The top faces of the cylinders are meshed with triangular elements and swept meshes are used along the depth of the cylinders with 10 element distribution. Triangular mesh is then applied to the triangles constituting the rhombuses on both top and bottom sides of the cylinders. Tetrahedral mesh is applied to regimes (ii (a)) , (ii (b)) (iii (a) ) and (iii (b)) with maximum element size 1.2372 mm.

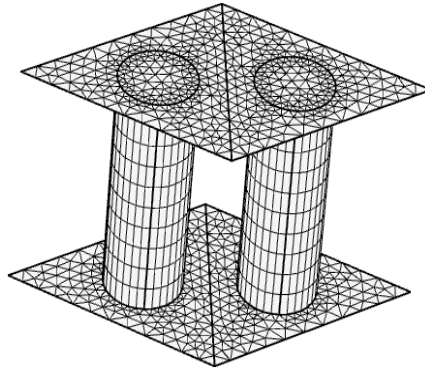


**Figure 4.12.** Mesh details of regime (i) shown in the previous **Figure 4.11**.

## 4.9 Conclusions

In this Chapter the principles of finite element were outlined, including discretisation. The properties of the software package used in this work, COMSOL<sup>®</sup>, were then described, together with a summary of the models used. The importance of appropriate mesh settings in order to obtain accurate solutions has been highlighted and the meshing details have been given for different geometries used to implement frequency domain, time domain and eigenfrequency models. Another key feature is the use of perfectly matched layers (PML) in the case of modelling sound propagation in solids for the reflections in the ends of the computational domain to be eliminated. However, in the eigenfrequency model for sound propagation in air, the PML was not necessary since losses are significant.

## 4.10 Appendix

The whole SAW device is assigned with 128° rotated Y-cut X-propagating LiNbO<sub>3</sub> piezoelectric material. This material is selected from a list of commonly used pre-defined materials, although materials can be also defined manually. The material density,  $\rho$ , introduced in chapter 2, where the equation of motion (19) was derived, is 4700 [kg/m<sup>3</sup>]. The values for the stiffness tensor (in GPa units)  $c_{ijkl}^E$ , relative permittivity tensor  $\epsilon_{ij}^S$ , and piezoelectric

coupling coefficient (in C/m<sup>2</sup> units)  $e_{kij}$ , introduced in equations (20) and (21) in chapter 2 are given below,

$$c_{ijkl}^E = \begin{bmatrix} c_{11} & c_{12} & c_{13} & c_{14} & c_{15} & c_{16} \\ c_{21} & c_{22} & c_{23} & c_{24} & c_{25} & c_{26} \\ c_{31} & c_{32} & c_{33} & c_{34} & c_{35} & c_{36} \\ c_{41} & c_{42} & c_{43} & c_{44} & c_{45} & c_{46} \\ c_{51} & c_{52} & c_{53} & c_{54} & c_{55} & c_{56} \\ c_{61} & c_{62} & c_{63} & c_{64} & c_{65} & c_{66} \end{bmatrix}$$

where:  $\{c_{11}, c_{12}, c_{22}\} = \{202.897, 52.9177, 202.897\}$ ,

$\{c_{13}, c_{23}, c_{33}\} = \{74.9098, 74.9098, 243.075\}$ ,

$\{c_{14}, c_{24}, c_{34}\} = \{8.99874, -8.99874, 0\}$ ,

$\{c_{44}, c_{15}, c_{25}\} = \{59.9034, 0, 0\}$ ,

$\{c_{35}, c_{45}, c_{55}\} = \{0, 0, 59.9018\}$ ,

$\{c_{16}, c_{26}, c_{36}\} = \{0, 0, 0\}$ ,

$\{c_{46}, c_{56}, c_{66}\} = \{0, 8.985, 74.8772\}$ .

$$\varepsilon_{ij}^S = \begin{bmatrix} \varepsilon_{11} & \varepsilon_{12} & \varepsilon_{13} \\ \varepsilon_{21} & \varepsilon_{22} & \varepsilon_{23} \\ \varepsilon_{31} & \varepsilon_{32} & \varepsilon_{33} \end{bmatrix},$$

where:  $\{\varepsilon_{11}, \varepsilon_{22}, \varepsilon_{33}\} = \{43.6, 43.6, 29.16\}$ ;  $\varepsilon_{ij} = 0$

$$e_{kij} = \begin{bmatrix} e_{11} & e_{12} & e_{13} & e_{14} & e_{15} & e_{16} \\ e_{21} & e_{22} & e_{23} & e_{24} & e_{25} & e_{26} \\ e_{31} & e_{32} & e_{33} & e_{34} & e_{35} & e_{36} \end{bmatrix},$$

where:  $\{e_{11}, e_{21}, e_{31}\} = \{0, -2.53764, 0.193644\}$ ,

$\{e_{12}, e_{22}, e_{32}\} = \{0, 2.53764, 0.193644\}$ ,

$$\{e_{13}, e_{23}, e_{33}\} = \{0, 0, 1.30863\},$$

$$\{e_{14}, e_{24}, e_{34}\} = \{0, 3.69548, 0\},$$

$$\{e_{15}, e_{25}, e_{35}\} = \{3.69594, 0, 0\},$$

$$\{e_{16}, e_{26}, e_{36}\} = \{-2.53384, 0, 0\}.$$

## CHAPTER 5

### ASW and SAW dispersion relations

#### 5.1 Introduction

Localised Acoustic Surface Waves (ASWs) on sculpted surfaces arise from the interference between localized (evanescent) and propagating fields (as already covered), and have been mainly used to demonstrate applications such as super-resolution [60] and deep-subwavelength focusing [61].

Localised Surface Acoustic Waves (SAWs) arise due to the coupling of Rayleigh waves with meta-surfaces. SAWs are characterized by displacements which decay exponentially with depth into an elastic material, and the maximum amplitude of the displacement induced by a SAW is small compared to the SAW wavelength. Within certain frequency range SAW delocalisation occurs as Rayleigh waves are deflected away from the surface (in the form of shear vertically polarized waves). Rayleigh-to-shear wave conversion has been proposed for applications in sensing [62] and seismic waves deflection [63], [64].

The main focus of the present chapter is to discuss (ASW) and (SAW) dispersion relations in order to understand the aforementioned circumstances, under which trapped ASWs and SAWs are formed. Modes that lie inside the sound cone (or sound line) will be referred to as non-radiative ASW and SAW modes. For normal incidence, ( $k_x = 0$ ), a mode lies outside the sound cone, thus it is radiative.

To begin with, the dispersion relation of a simple system supporting ASWs, a one dimensional array of slits, will be presented followed by a short review of structures showing Dirac-cone dispersion relations both in the radiative and the non-radiative regime. An emphasis is given to the study which proves that there is an analogy between ASWs and electrons in graphene.

The dispersion relation derivation for a SAW grating has already been discussed in section 2.2.4.1 where the grating's scattering matrix was introduced and the appearance of band gaps was explained. In the present chapter, the dispersion relation for a Rayleigh SAW wave interacting with a periodic structure will be presented in order to cross compare with the ASW dispersion relation.

## 5.2 Acoustic Surface Wave dispersion relation

In order to define the surface wave, we consider a plane wave with maximum momentum value  $k_0 = \frac{2\pi}{\lambda_0} = \frac{\omega}{c}$ , propagating in free space in some arbitrary direction over a lattice surface. The wavevector, can be analysed in its parallel and perpendicular components. We will denote  $k_{par}$ , the component which is parallel to the lattice surface and  $k_{ver}$ , the perpendicular to the lattice surface component. Thus  $k_0^2 = k_{par}^2 + k_{ver}^2$ . In the case that an ASW is excited, the magnitude of its momentum,  $k_{par}$ , is greater than the momentum of the plane wave ( $k_0 < k_{par}$ ), Therefore  $k_{ver}$ , must become imaginary for the conservation of momentum to be satisfied:

$$k_{ver}^2 = -(k_0^2 - k_{par}^2) = i^2(k_0^2 - k_{par}^2) \quad (5.1)$$

The physical meaning is that the wave propagates parallel to the surface but exponentially decays in the vertical direction with respect to the boundary. It is an evanescent wave, also known as surface wave. Equation (5.1) also explains why the imaginary roots were selected for substitution in the form of solution for Rayleigh surface waves in section 2.3.7 (Equation 2.36). For simplicity it will be assumed that  $k_{par}^2 = k_x^2$  and  $k_{ver}^2 = k_z^2$ , hence the system is two dimensional. The boundary between the free space and the lattice surface is at  $z = 0$  and a plane wave travelling at  $z \geq 0$  satisfies the Helmholtz equation (3.22) and is written as:

$$\Delta p = p(x, z)e^{i\omega t} \quad (5.2)$$

where  $p$  is pressure and  $\omega$  the angular frequency of the plane wave.

The impedance boundary condition at  $z = 0$  is:

$$\frac{\partial p(x, 0)}{\partial z} = -\frac{ik\rho_0 c}{z_s} p(x, 0) \quad (5.3)$$

where  $z_s$  is the specific acoustic impedance of the lattice extending through  $z \leq 0$  and  $\rho_0 c$  the specific acoustic impedance of air. The definition of specific acoustic impedance has been given in equation (3.33) but since the situation we are describing in this section involves geometry changes, it takes the complex form:

$$z_s = r_s + ix_s \quad (5.4)$$

where  $r_s$  is the real-valued specific acoustic resistance and  $x_s$ , the specific acoustic reactance. For the solutions to satisfy the boundary condition (5.3) the imaginary part of the  $z_s$  must be greater than zero, meaning that the surface's acoustic reactance is a stiffness [65]. A reasonable criterion for a wave to be characterized as surface wave is a fast decay of its pressure amplitude in direction perpendicular to the surface ( $z$  direction) and a relatively long decay length in the direction parallel to the surface ( $x$  direction). Specifically, the pressure along  $z$  direction must fall to  $1/e$  of its initial value within one free space wavelength  $\lambda_0$ . The quantitative criteria for the existence of a surface wave is that the surface's acoustic reactance is greater in magnitude than its acoustic resistance,  $x_s > r_s$  and that  $2 < \frac{x_s}{\rho_0 c} < 6$  [66]. It is hence implied that a trapped wave can exist at the boundary of an impedance mismatch [67] and that the impedance discontinuity must be finite.

The first ASW was measured by Ivanov-Shits and Rozhin in 1959 [68] and since then many studies have focused on the creation of ASWs by depositing a layer of air-filled porous material above a solid [69], [70]. However, in this thesis the creation of ASWs is achieved by utilising impedance gratings. The impedance gratings investigated, are subwavelength gratings, meaning that the condition  $\lambda_g \ll \lambda_{FP}$  must be met, where  $\lambda_{FP}$  is the wavelength corresponding to the Fabry-Pérot (FP) resonant frequency.

An impedance grating is shown in **Figure 5.1**. This grating is periodic only in one direction in order to simplify the analysis, although the experimental samples (Chapter 6) are 2D periodic structures. The structure is formed of air cavities arranged periodically in a perfectly rigid material. Each individual cavity acts as a resonator (as discussed in **section 3.5**) which is coupled to its adjacent cavities via periodicity induced diffracted evanescent waves. As a result of periodicity, cavities' surface integrals overlap and cavities' radiation impedance  $Z_{rad}$  changes, leading to a modified end correction [71]. ASWs arise from coupling between these end effects. Coupling between cavities creates the condition for developing theories that can describe useful parameters and properties of the composite material as a whole. One of these parameters, is the effective impedance of the surface, and a good agreement between modelled and measured acoustic effective impedance is shown in [72]. The grating's effective impedance affects waves' confinement to the surface and its value changes with frequency. Specifically, at low frequencies the effective impedance of the grating is little different to the impedance of air and hence, the ASW sits near the sound line, as shown in the lower panel of **Figure 5.1**. Consequently, the ASW is only loosely confined to the surface.

It should be noted that the sort of plot is the so called dispersion relation which gives information about how a wave's phase velocity  $v_p = \frac{2\pi f}{k}$  changes as a function of frequency. The sound line is the wave travelling in air in direction parallel to the wall and it can be seen that its phase velocity does not change with frequency. Moreover, the group velocity,  $v_g = \frac{2\pi f}{\partial k}$ , i.e, the gradient of any point in the sound line, is equal to the phase velocity; the mode is hence non-dispersive.

In contrast, the ASW's phase velocity changes with frequency and as illustrated in **Figure 5.1**, it diverges from the sound line as frequency increases. This is attributed to the fact that as the excitation frequency approaches the cavity's resonance frequency (shown in dashed line), the impedance grating's effective imaginary reactance approaches infinity [71] causing  $k_{ASW,x} \rightarrow \infty$  and  $ik_{ASW,z} \rightarrow \infty$ . Hence, the ASW moves further from the sound line in  $k_x$  and since its imaginary component in  $k_z$  is rising, it is gradually more confined to the surface.

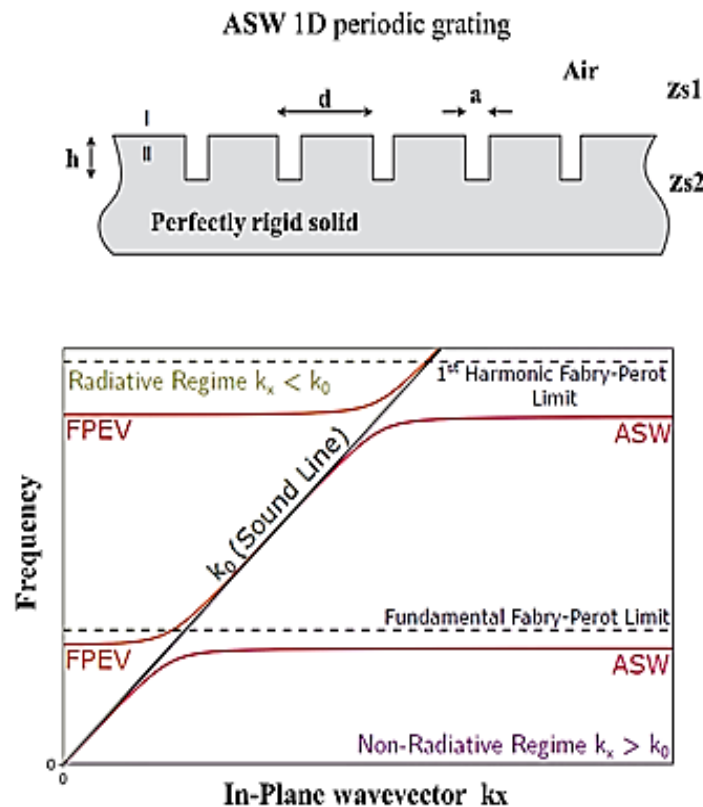


**Figure 5.1.** Top panel :1D periodic grating of period  $d$ . The slit width  $a$ , and height,  $h$ , are shown in black arrows. The perfectly rigid solid has impedance  $z_{s2}$  and the cavities are filled

with air, of impedance  $z_{s1}$ . Modified from [73]. Bottom panel: Qualitative example of a dispersion plot for a typical short-pitch impedance grating. The solid red lines show the eigenmodes of the system both in the radiative ( $k_x < k_0$ ) and the non-radiative regimes ( $k_x > k_0$ ). The fundamental Fabry-Pérot resonant frequency and its first harmonic, are indicated in dashed lines. Modified from [74].

In order to understand the nature of the mode at  $k_x = 0$ , shown in red solid line at the bottom left panel of **Figure 5.1**, the instantaneous pressure fields at normal incidence ( $k_x = 0$ ) must be taken into account. If the mode originates at  $k_x = 0$ , it behaves more like an unperturbed FP resonance. By contrast, in case it is band folded from  $k_x = k_g$  via diffraction, it behaves more like an evanescent mode [74]. An ASW mode of that kind will be referred to as Fabry-Pérot Evanescent (FPEV) mode.

Note that  $k_g$ , is the first reciprocal lattice point (for simplicity it will be denoted by  $G$  in section 5.3) and the first Bragg plane, or in other words the first Brillouin zone, occurs halfway between the origin and  $k_g$ . Hence the first Brillouin zone is defined as extending over  $-\frac{k_g}{2} \leq k_x \leq \frac{k_g}{2}$ .

The mode's behaviour is dependent on the pitch of the impedance grating,  $d$ , as well as the width of the slit  $a$ . **Figure 5.2** (upper panel) shows the instantaneous pressure fields at normal incidence for a short pitch grating. It can be seen that no significant phase change occurs along  $x$ , as it would be required for an evanescent mode to propagate along  $x$ . Consequently, for a short pitch grating, the mode at  $k_x = 0$  behaves more as a Fabry-Pérot resonance and its frequency is lower than the fundamental Fabry-Pérot limit due to end effects.

As  $k_x$  increases, two observations can be made. First, the FPEV mode is not flat banded (as it is at low  $k_x$ ) and it has a positive curvature due to the strong anti-crossing with the sound line. For higher momentum the mode crosses the FP limit and further increase in momentum makes it indistinguishable from a grazing wave. The second observation is that as  $k_x$  increases, the mode initially indistinguishable from the grazing wave in the non-radiative regime ( $k_x > k_0$ ) curves away from the sound line at larger values of  $k_x$ . This is due to the interaction of the ASW with the existing FPEV mode in the radiative regime ( $k_x < k_0$ ). The stronger the coupling strength between these two modes, the broader the frequency range over which the ASW curves away from the sound line. Consequently, for fixed pitch, the increase of slit width  $a$ , would result in a more intense anti-crossing; the FPEV would exhibit positive curvature at lower  $k_x$

values. At those low  $k_x$  values, the ASW would curve away from the sound line leading to a wider band gap with respect to the narrow width case.

For even higher  $k_x$ , the ASW approaches asymptotically the FP limit and at  $k_x = k_g/2$  (Brillouin zone), its group velocity falls to zero. This is because standing waves are formed at the Brillouin zone border (to be discussed).

The bottom panel of **Figure 5.2** shows that for the long pitch grating the mode at  $k_x = 0$ , behaves more like an ASW, since there is significant phase shift between each cavity above the solid. The spatial wavelength  $\lambda_x$ , (denoted by the black arrow) equals  $\lambda_g$  (denoted by the yellow arrow), meaning that it does not actually originate at  $k_x = 0$ , but rather on  $k_x = k_g$ . The wave's peaks and troughs are shown in black solid line and the peaks correspond to positive  $\Delta P$ , according to the colour legend.

At  $k_x = k_g/2$ , i.e at the Brillouin zone edge, the condition that must be satisfied is  $\lambda_x = 2\lambda_g$ . Two possible configurations of the instantaneous pressure field, satisfying this condition for a short pitch grating, are shown in the right panels of **Figure 5.2**. In the top right panel, the wave's antinodes are positioned inside the slits, meaning that two neighbouring slits have a phase difference of  $\pi$ . This results in the formation of an evanescent wave above the surface, where the phase shift along  $x$  direction can be observed. However, for the second configuration shown in the bottom right panel, the wave's nodes are placed inside the slits, meaning that the excitation of an ASW is not possible in that case, since an evanescent coupling of the periodic air-filled cavities is necessary for its existence. Hence, there is only one standing wave in the non-radiative regime for the ASW grating of **Figure 5.1** because the rigid-wall approximation forbids the placing of the pressure fields inside the solid material. It should be noted that a second standing wave occurs at the Brillouin zone border for more complicated ASW gratings. Examples will be given in the next section.

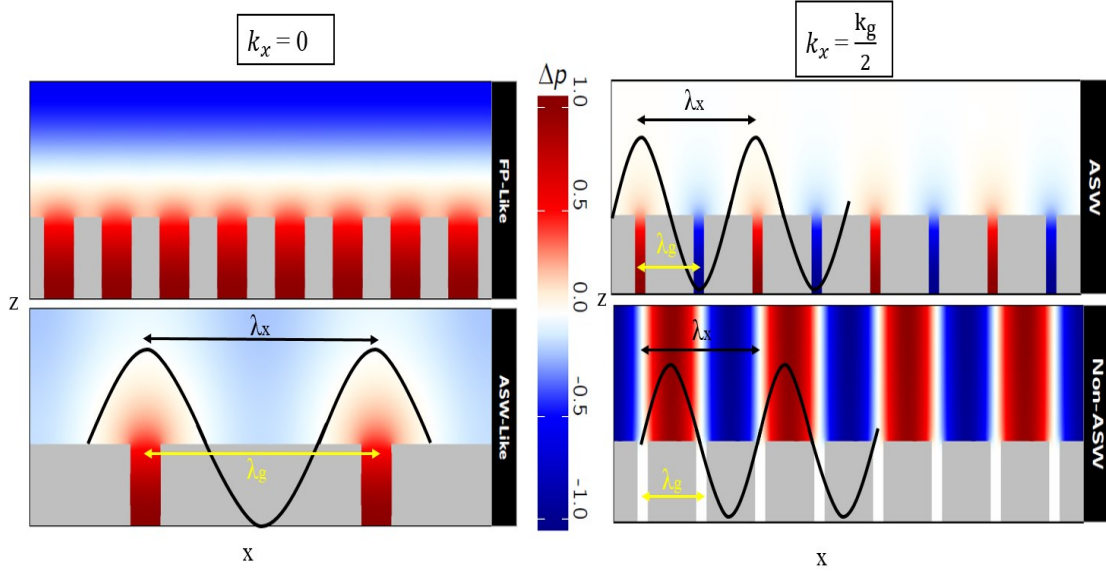


**Figure 5.2.** Instantaneous pressure field  $\Delta p$  maps of the FPEV modes at normal incidence  $k_x = 0$  for a short pitch grating (top left) and a long pitch grating (bottom left). For the short pitch grating  $\lambda_{FP} \gg \lambda_g$ , the FPEV is more FP-like whereas for the long pitch grating  $\lambda_{FP} \approx \lambda_g$  the mode is more ASW-like. The wave is represented by solid black line with peaks at positive  $\Delta P$  and troughs at negative  $\Delta P$ . The black arrow indicates the distance between the wave peaks and the yellow arrow indicates the grating period  $\lambda_g$ . Top right: Instantaneous pressure fields of the ASW at the Brillouin zone boundary  $k_x = k_g/2$ , where a standing wave has been formed with  $\lambda_x = 2\lambda_g$ . Bottom right : Instantaneous pressure fields of a standing wave with  $\lambda_x = 2\lambda_g$ . The excitation of this mode requires fields with nodes inside the cavities and anti-nodes above the rigid walls. Therefore it is not a trapped mode but a radiative wave that exists at the point where the sound line crosses the BZ boundary,  $k_0 = k_x = k_g/2$ . Modified from [74]

### 5.3 Dirac-cone dispersion relations for Acoustic Surface Waves

The presence of two standing waves is of particular interest in the case that the standing wave modes cross each other at the BZ border. The point at the BZ border at which the crossing occurs is referred to as Dirac point. In the description of the transport of electromagnetic waves near the Dirac point inside photonic crystals (PhCs), Maxwell's equations [75] can be reduced to the Dirac equation and as a result the electromagnetic waves in the PhCs transmit in an unusual way. For example, the optical conductance near a Dirac point is inversely proportional

to the thickness of the sample. Inspired from electromagnetics, an acoustics study was made in order to prove if the transmission of an acoustic wave near the Dirac point is inversely proportional to the thickness of the sample [76]. This result, is illustrated in the middle panel of **Figure 5.3**, where it is clear that for thicker samples (middle panel, dashed line) the measured transmission coefficient decreases.

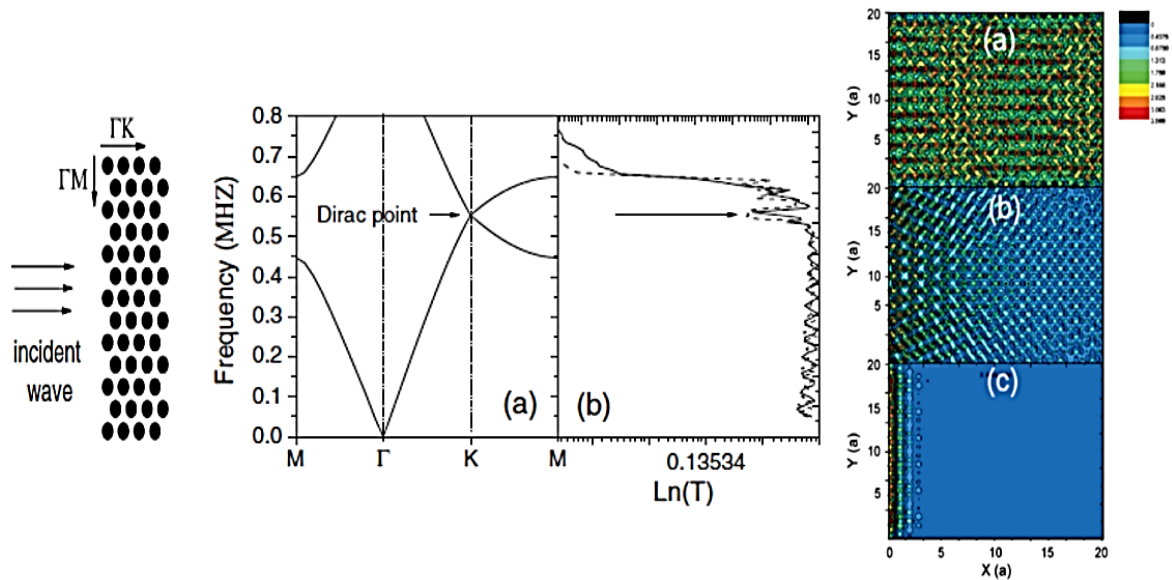


**Figure 5.3.** Left panel: Two dimensional structure consisted of a triangular lattice of steel cylinders in a water background. The  $\Gamma K$  and  $\Gamma M$  directions of reciprocal space are shown in arrows. Middle panel (a) Calculated phononic band structure (b) The measured transmission coefficient of an acoustic wave along the  $\Gamma K$  direction for a 2D sonic crystal of radius  $R/\alpha = 1/3$ , where  $\alpha$  is the lattice constant. The solid/dashed line corresponds to the result with sample thickness  $L = 10 \alpha / 20 \alpha$  respectively. Right panel: The field energy distribution at (a)  $f = 0.45$  MHz and (b)  $f = 0.55$  MHz (Dirac frequency) along the  $\Gamma K$  direction and (c) at  $f = 0.55$  MHz along the  $\Gamma M$  direction Taken from [76].

In order to study the role that the Dirac point plays to these peculiar transmission phenomena, the distribution of the field energy in  $\Gamma K$  and  $\Gamma M$  direction was plotted at the Dirac frequency,  $f = 0.55$  MHz and at another frequency close to the Dirac frequency in the  $\Gamma K$  direction. The  $\Gamma K$  and  $\Gamma M$  directions as are shown on the left panel of **Figure 5.3**. In the  $\Gamma K$  direction, and at frequency different from the Dirac frequency, the field intensity does not decrease along  $x$  direction (right panel, figure (a)), which corresponds to ballistic behaviour. On the other hand,

at the Dirac frequency, the field intensity decreases linearly along  $x$  (right panel, figure (b)) which is similar to the diffusion of waves through a disordered medium, even in the absence of any disorder in the sonic crystal. In the  $\Gamma M$  direction where a gap is expected at the Dirac frequency, the field intensity is suppressed exponentially (right panel, figure (c)). In the same study an attempt to observe an acoustic analogue effect to the “Zitterbewegung” (ZB) [77] was made by measuring the time dependence of transmission coefficients of acoustic pulses. Their experimentally obtained results were compared with analytical calculations for the time dependent displacement of the wave packet and a good agreement was displayed.

The experimentally confirmed acoustic analogue effect to the ZB of relativistic electrons and the unusual dispersion of the electronic bands in graphene [78] inspired Daniel Torrent and José Sánchez-Dehesa in 2012 [7] to investigate analogies between ASWs and electrons in graphene. The dispersion relation of an acoustically rigid surface with cylindrical cavities drilled in a honeycomb lattice using a phase-delay measurement illustrated in **Figure 5.4**. Near some isolated points of the BZ (the Dirac points), the band structure of the lattice system is described by Weyl [79] Dirac like equations [80], [81], which were first introduced as relativistic equations for a single free particle. The relativistic-like behaviour originates from the particular honeycomb lattice structure and was evidenced by observing a very particular Quantum Hall effect in graphene [82], which is specific to relativistic carriers. Interestingly, in the low energy effective theory near the Dirac points in acoustic graphene, the Hamiltonian describing the system, can be cast into the 2D Weyl Hamiltonian describing massless spin one-half relativistic particles. Therefore, the wave function of the acoustic system can be derived by solving the Schrödinger equation for an electron in a crystal. The presence of the lattice demands the Bloch theorem to be satisfied and this condition will be used in order to define the reciprocal lattice vectors.

The wave equation for an electron in a crystal is  $H\psi = \varepsilon\psi$ , where  $H$  is the Hamiltonian and  $\varepsilon$  is the energy eigenvalue. The solutions  $\psi$  are called eigen-functions. Explicitly, the wave equation is:

$$\left(\frac{1}{2m}p^2 + U(x)\right)\psi(x) = \varepsilon\psi(x) \quad (5.5)$$

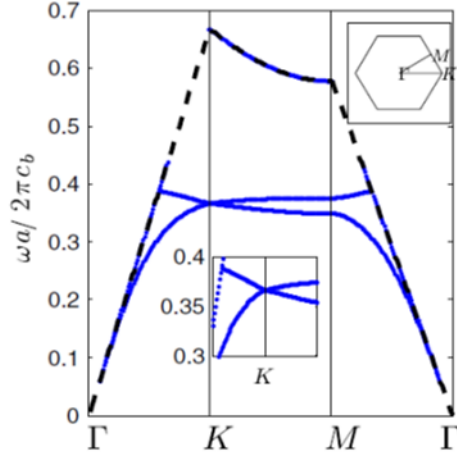


**Figure 5.4 :** Band structure of the acoustic surface waves propagating on a honeycomb lattice of boreholes drilled in a Plexiglass plate. The upper right inset shows the Brillouin zone with the high symmetry points. The central inset shows a zoom of the dispersion relation around the Dirac point. Taken from [7].

If  $U(x)$  is the potential energy of an electron in a linear lattice of lattice constant  $\alpha$ , the potential energy at the point  $U(x+\alpha) = U(x)$ , because the potential energy is invariant under a crystal lattice translation. A function invariant under a crystal lattice translation may be expanded by a Fourier series in the reciprocal lattice vectors  $G$ , as shown in the following equation:

$$U(x) = \sum_G U_G e^{iGx} \quad (5.6)$$

The wavefunction  $\psi(x)$  may be expressed as a Fourier series summed over all values of the wave vector permitted by the boundary conditions so that

$$\psi(x) = \sum_k C(k) e^{ikx}, \quad (5.7)$$

where  $k$  is real. The set of values of  $k$  has the form  $2\pi n/L$ , because these values satisfy the periodic boundary conditions over length  $L$ . By substituting (5.6) and (5.7) into (5.5), the wave equation is obtained as the sum:

$$\sum_k \frac{\hbar^2}{2m} k^2 C(k) e^{ikx} + \sum_G U_G \sum_k C(k) e^{i(k+G)x} = \varepsilon \sum_k C(k) e^{ikx} \quad (5.8)$$

By setting  $q \rightarrow k + G$ , and  $q \rightarrow k'$  a simpler form of the Schrödinger equation in  $k$ -space is obtained:

$$\sum_{k'} e^{ik'x} \left[ \left( \frac{\hbar^2(k')^2}{2m} - \varepsilon \right) C(k') + \sum_G U_G C(k' - G) \right] = 0 \quad (5.9)$$

For any fixed  $k$  in the first Brillouin zone, it only couples to  $k, k - G, k - G', \dots$

Therefore, the wave function will be of the form:

$$\psi_k(x) = \sum_G C(k - G) e^{i(k-G)x} \quad (5.10)$$

Equation (5.10) satisfies the Bloch theorem  $\psi_k(x + a) = e^{ikx} \psi(x)$ , if the reciprocal lattice vectors are  $\mathbf{G} = v_1 \mathbf{b}_1 + v_2 \mathbf{b}_2 + v_3 \mathbf{b}_3$ , where  $\mathbf{b}_1, \mathbf{b}_2, \mathbf{b}_3$  are the primitive vectors of the reciprocal lattice and  $v_1, v_2, v_3$  are integers. Therefore, it is proved that not all wavevectors of the set  $2\pi n/L$ , enter the Fourier expansion of any one Bloch function. If one particular wavevector  $k$  is contained in a  $\psi$ , then all other wavevectors in the Fourier expansion of this  $\psi$ , will have the form  $k - G$ . It should be noted that the reciprocal lattice points can be predicted by considering the real space honeycomb structure illustrated on **Figure 5.5**. The sites of the two triangular sublattices are marked with different colours and the basis vectors  $\mathbf{a}_1$  and  $\mathbf{a}_2$  of sublattice A (whose sites are shown in red circles) are :

$$\mathbf{a}_1 = \sqrt{3}a \mathbf{e}_x + 0 \mathbf{e}_y + 0 \mathbf{e}_z \quad (5.11)$$

$$\mathbf{a}_2 = \frac{a}{2} (\sqrt{3} \mathbf{e}_x + 3 \mathbf{e}_y) + 0 \mathbf{e}_z \quad (5.12)$$

$$\mathbf{a}_3 = (0 \mathbf{e}_x + 0 \mathbf{e}_y + 1 \mathbf{e}_z) \quad (5.13)$$

where  $a$  is the distance between sites A and B. The reciprocal lattice can be built from the direct lattice by substituting  $\mathbf{a}_1$  and  $\mathbf{a}_2$  to the following equations.

$$\mathbf{b}_1 = 2\pi \frac{\vec{a}_2 \times \vec{a}_3}{\vec{a}_1 \cdot (\vec{a}_2 \times \vec{a}_3)} \quad (5.14)$$

$$\mathbf{b}_2 = 2\pi \frac{\vec{a}_3 \times \vec{a}_1}{\vec{a}_1 \cdot (\vec{a}_2 \times \vec{a}_3)} \quad (5.15)$$

The reciprocal lattice vectors,  $\mathbf{b}_1, \mathbf{b}_2$ , are hence defined such that:

$$\mathbf{b}_1 = \frac{2\pi}{3} \frac{1}{a} (\sqrt{3}\mathbf{e}_x - \mathbf{e}_y) \quad (5.16)$$

$$\mathbf{b}_2 = \frac{4\pi}{3} \frac{1}{a} (0\mathbf{e}_x + \mathbf{e}_y) \quad (5.17)$$

The reciprocal lattice points (for the real lattice shown in **Figure 5.5**) are denoted in yellow filled dots in **Figure 5.6**. The reciprocal lattice vectors  $\mathbf{b}_1$  and  $\mathbf{b}_2$  are shown in black arrows and the first Brillouin zone (also shown in the inset of **Figure 5.4**) is the red coloured hexagon.

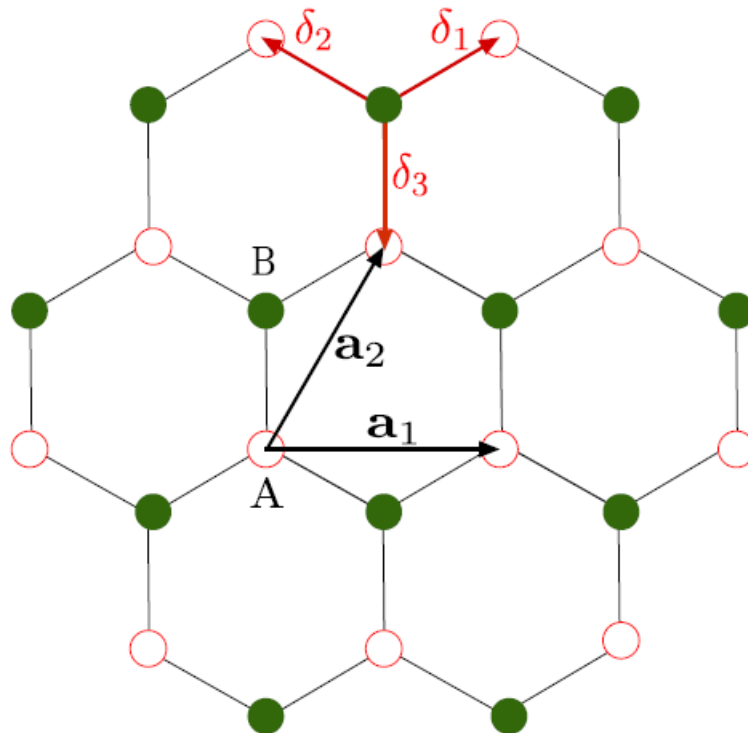


**Figure 5.5** Honeycomb lattice with two interpenetrating triangular sublattices. Red open (green filled) dots for A (B) sublattice. The red thick arrows denote the vectors  $\delta_\alpha$  ( $\alpha = 1, 2, 3$ ) connecting of a given site to its three nearest neighbours. The basis vectors  $\mathbf{a}_1$  and  $\mathbf{a}_2$  of the Bravais lattice are shown in black arrows.

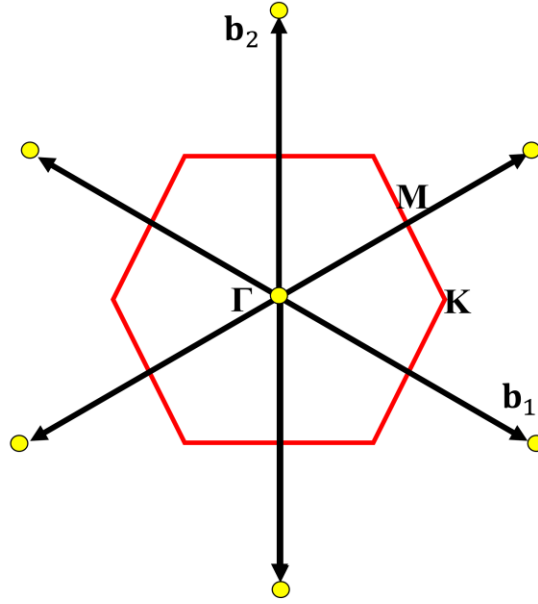


**Figure 5.6.** Reciprocal space corresponding to the real space lattice shown in **Figure 5.5**. The first Brillouin zone is the red hexagon, its origin is denoted with  $\Gamma$  and the letters M and K mark high symmetry directions along which dispersion relations are plotted. The reciprocal lattice vectors  $\mathbf{b}_1$  and  $\mathbf{b}_2$  are shown in black arrows.

Torrent's study [7] has proven that the pressure field above the structure, which is normally described by a linear superposition of surface waves, is described by a single wave at the Dirac frequency:

$$\Psi_s(\mathbf{K}, \mathbf{r}) = \sum_G A_G e^{i\mathbf{K} \cdot \mathbf{r}} e^{i\mathbf{G} \cdot \mathbf{r}} e^{-\Gamma_G z} \quad (5.11)$$

where  $\Gamma_G^2 = |\mathbf{K} + \mathbf{G}|^2 - k_0^2$ ,  $\mathbf{K}$  is the Bloch wave number and  $\mathbf{G}$  the reciprocal lattice vector. The equation has the same form as the Bloch's solution of Schrödinger's equation for an electron in a periodic potential, except for the exponential describing the  $z$  dependence of the ASW. The analogy has been also supported by describing the pressure field by means of Bessel equations and by casting the characteristic equation of the problem (obtained by applying the mode matching technique to the unit cell [83]) into the Dirac equation. The expressions of Dirac frequency and Dirac velocity as functions of the resonators' radius and depth were obtained and it was shown that at the Dirac frequency the ASW travels about 12 times slower than it does in free space. Applications of slow sound propagation as well as interesting

propagation phenomena arising from gapping out the Dirac points of graphene and similar lattice structures ( usually referred to as Dirac materials ) will be discussed in the next section.

#### 5.4 Applications of Dirac materials

In acoustics, slow sound propagation is relevant to the design of narrow band transmission filters, delay lines, switches and it also opens perspectives in ways to enhance nonlinear effects at local resonances [84]. Other applications that have experienced an increased interest in the field of slow sound are acoustic transparency [85] and the acoustic rainbow effect [86], [87]

Except for inducing slow light, Dirac materials have been used to manipulate light so that it can travel in only one direction, without any reflection. Using ideas borrowed from an abstract area of mathematics known as topology (which studies the properties of shapes that stay the same when you squeeze and mould them), ideas that won to 2016 Nobel prize, the discovery of new unusual materials became reality. This new class of materials, the so-called topological insulators (TIs) are distinguished from ordinary band insulators by the presence of a one-dimensional metal along their edge, in the case of 2D TIs. The 3D TIs are insulating in the bulk and exhibit topologically protected metallic states at their surfaces. Those 2D surface states are characterized by a single (or an odd number) of non-degenerated Dirac cone(s). The aforementioned Dirac points characterizing the Dirac materials have been gapped out in order to induce electromagnetic wave propagation protected from backscattering and undesired reflections. Topological materials can be used in telecommunications, where information propagates as pulses and it is lost when there are reflections, as well as in new generations of electronics and superconductors or in future quantum computers.

The range of applications of Dirac materials and TIs becomes even broader if we consider that Dirac points in dispersion relations, have been exhibited not only in electronic, photonic and phononic systems (some examples of which were given in the previous paragraphs) but also in polaritonic [88] and plasmonic systems [89], [90], [91]. The 2D plasmonic lattice can support both scalar waves and vector waves, terms like dipole and quadrupole modes have been used in order to characterise the bands of acoustic systems. Dirac points exist for both dipole and quadrupole modes in plasmonic systems and as a consequence these structures can support edge states with unique characteristics, for example they provide new propagation channels of

light for a specific range of frequencies. It was thus expected, that the discovery of new propagation channels for sound would require similar mode profiles.

The presence of edge states in an elastic system has been confirmed by using multiple scattering theory [92] and the phenomenon is illustrated in **Figure 5.7 (A)**. The first theoretical study that numerically demonstrated acoustic modes propagating along a zig-zag edge was by Zhong et al. [93]. The edge states at that work were a result of the existence of acoustic Dirac points at the Brillouin zone edges, although topologically protected edge states have been reported for structures exhibiting both acoustic Dirac (deterministic) and Dirac-like points at the Brillouin zone centre. This phenomenon has also been highlighted as important for the realisation of zero phase change propagation, (**Figure 5.7 (B)**) [94], the defect immune property and the Talbot effect [95] (**Figure 5.7 (C)**). The Talbot effect is a near-field diffraction effect, in which a plane wave transmits through a grating or other periodic structures with the resulting wave fronts propagating in such a way that replicates the structure.

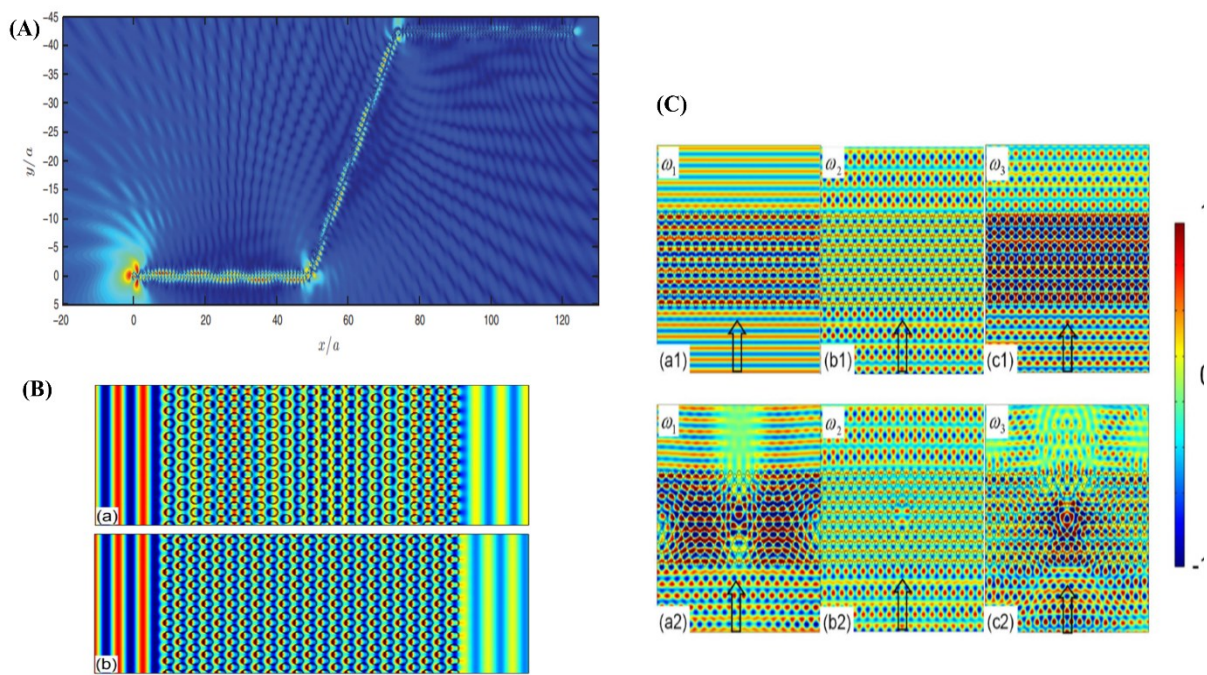


**Figure 5.7.** (A) Multiple scattering simulation of an edge state excited in a single-line zigzag ribbon. Note that although the state is guided along the ribbon, there are also leaky waves. Taken from [92]. (B) The pressure field distributions when a  $\Gamma M$ -direction plane wave is incident on a PhC slab. The PhC slab is put inside a straight waveguide with sound hard boundary conditions on the upper and lower walls of the waveguide. The frequency of the incident wave is  $0.5906 \left(\frac{2\pi c_0}{a}\right)$  on (a), which is below the double Dirac point frequency.

Substantial phase change can be observed inside the PhC slab. (b) The same as (a), except that the frequency of the incident wave is  $\omega = 0.6092 \left(\frac{2\pi c_0}{a}\right)$ , exactly at the double Dirac point frequency. Taken from [94] (C) Transmission patterns with cylindrical incidence source. Operation frequencies are set at (a)  $\omega_1$ , (b)  $\omega_2$ , (c)  $\omega_3$ . The suffix 1 or 2 represents the case of PhC without or with defect. (b1) and (c1) exhibit the Talbot effect. (b2) shows the defect-immune property. Taken from [95].

## 5.5 Surface Acoustic Wave dispersion relation

In contrast to ASWs, for the SAW grating of **Figure 5.8**, two standing waves are present in the non radiative regime because the  $\text{SiO}_2$  material (silicon oxide) shown in the top panel is not rigid. Hence, two modes can be present; one having nodes between the oxide bars and the other on the oxide bars. The term nodes refers to the  $z$ -component of the displacement field. These modes are zero-group velocity modes for wave vectors at the first BZ boundary and thus exhibit a non-propagating character. From the dispersion relation of the Rayleigh wave it can be observed that its phase velocity is lower than the velocities of the bulk waves and thus it propagates without radiating energy into the substrate.

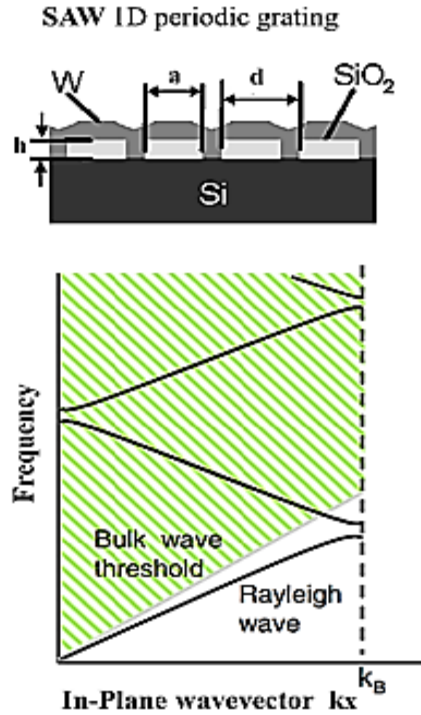


**Figure 5.8.** Top: Schematic of the cross section of the sample used in [96] for the generation and propagation of Rayleigh surface waves. Bars of amorphous SiO<sub>2</sub> of height  $h$ , and width  $a$ , are periodically arranged on a Si wafer. Bottom: Schematic representation of the Rayleigh surface wave dispersion for the structure shown in the upper right panel. The wavevector at the Brillouin zone border is denoted as  $k_B$ . In the dashed region above the bulk transverse threshold, the surface waves become leaky. Taken from [96].

It is worth mentioning at this point, that the reduced-zone scheme representation of the band structure shown on the dispersion plot of **Figure 5.8**, is different to the representation used in **Figure 2.7** of section 2.2.4.1. In the latter representation, every energy band is drawn within every Brillouin zone whereas in the reduced-zone scheme only the first Brillouin zone is included, but with every mode band folded back to  $k_x = 0$  via addition or subtraction of the grating wavevector  $\pm k_g$ . For simplicity, the band structure in each case. Hence, in **Figure 5.8**, the mode that crosses the bulk velocity threshold (grey solid line) becomes leaky through the radiation of bulk waves. The bandgaps arising at the boundary and the center of the BZ, are thus a result of zone-folding [97].

It can also be seen that the SAW mode moves away from the sound line as the magnitude of the wavenumber increases implying SAW's confinement to the surface. The same observation

was made for the ASW mode of **Figure 5.1**. It can therefore be deduced that the presence of a 1D periodic structure controls the confinement mechanism of ASWs and SAWs.

## 5.6 Dispersion relations for Rayleigh SAW waves interacting with meta-surfaces

In the dispersion relation of structures supporting ASWs (see **Figure 5.1**), the “sound line” is the dispersion of acoustic wave in the homogeneous background medium which lies above the impedance grating. As discussed in section 3.3.4, for the background medium being the air at room temperature, the sound velocity is  $c_a = 343 \text{ ms}^{-1}$ . In the dispersion relation of structures supporting SAWs, the sound line is the dispersion of the transverse wave propagating in the bulk. In the present section, the sound line will be denoted in the dispersion relation graphs as  $c_T$ . In the case where the bulk substrate is free (not metallized)  $128^\circ$  Y-X cut  $\text{LiNO}_3$ , the velocity of the Rayleigh wave  $c_R$  is 4000 m/s, as discussed in section 2.3.8. When a different substrate is used, as in the following example, a different value of  $c_R$  is expected.

The dispersion relation of a Rayleigh SAW interacting with silica microspheres, is shown in red solid lines in **Figure 5.9 (b)**. When the microspheres are not present, the Rayleigh SAW is dispersionless and its velocity  $c_R$  is shown in black solid line. A longitudinal and a transverse wave are also travelling in the substrate, with velocities  $c_L$  and  $c_T$  respectively (black dashed lines). It can be observed that the presence of the microspheres results in the hybridization of the Rayleigh SAW into two Rayleigh-like solutions with opposite phases [98]. The silica microspheres form a two-dimensional metasurface and the theoretical dispersion relation agrees with the dispersion relation measured by using a laser induced TG technique [99]. The Fourier transform of the signal acquired at an incident acoustic wave vector magnitude  $k = 2\pi/\lambda_s = 0.46 \text{ }\mu\text{m}^{-1}$  is shown in **Figure 5.9 (a)**.

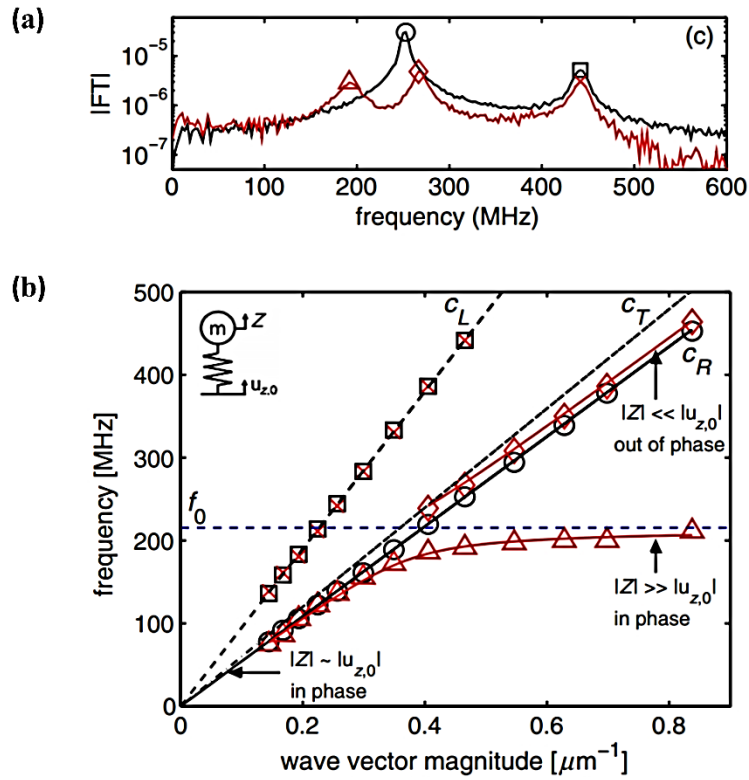


**Figure 5.9.** (a) Fourier transform (FT) magnitude corresponding to the signal acquired from a sample location without microspheres (black line) is plotted in log scale along with the FT magnitude for the on microspheres case (red line). The incident acoustic wave vector magnitude is  $k = 2\pi/\lambda_s = 0.46 \mu\text{m}^{-1}$  (b) Dispersion relations. Red and black markers are the measured frequency peaks for the on- and off spheres cases, respectively. The solid red line is the dispersion calculated using the theoretical model from [98]. Also shown are lines corresponding to longitudinal, transverse, and Rayleigh waves in fused silica, and a horizontal line corresponding to the microsphere contact resonance frequency. Taken from [98].

The black/red colour represents the Fourier transformed signal for the off/on microspheres cases respectively. For the off-microsphere case there are two peaks. The peak marked with the circle (low frequency peak) corresponds to the Rayleigh wave whereas the peak marked with square (high frequency peak) corresponds to the longitudinal wave. For the on-microsphere case three peaks can be observed from which only the peak corresponding to the longitudinal wave occurs at the same frequency as for the off-microspheres case. The peaks marked with a triangle/rhombus correspond to the Rayleigh-like solutions and they lie

below/above (respectively) the fitted resonance frequency, indicated in horizontal dashed line. The theoretical model assumes that the microspheres are masses connected to the substrate via springs.  $Z$  is the displacement of the oscillators relative to the surface and  $u_{z,0}$  is the displacement of the substrate surface. For the Rayleigh mode lying below the resonant frequency  $|Z| \gg |u_{z,0}|$  whereas for the upper branch  $|Z| \ll |u_{z,0}|$ . The upper branch is close to the Rayleigh wave at high wave vector magnitudes, and it gradually deviates from the Rayleigh line at lower wave vector magnitudes. When its phase velocity is equal to the transverse acoustic velocity of the substrate  $c_T$ , the mode reaches the threshold and terminates. The phase velocity must be smaller than  $c_T$ , otherwise at least one of the square root terms of the dispersion relation described in [98] becomes imaginary. In that study, the upper branch peak disappeared past the threshold in the experiment and hence the leaky wave solutions with complex  $\omega$  were not investigated. The Rayleigh wave velocity shown in solid black line was calculated by numerically solving the Rayleigh equation [100] and its value is  $c_R = 3409$  m/s . The aforementioned structure belongs to the class of “locally resonant metamaterials for which the avoiding crossing occurs at wavelengths much larger than the size of the unit cell. The frequency range around the avoided crossing is often referred to as bandgap. Bandgap formation for elastic waves in 2D systems consisting of two composite materials, the host and the periodic structure, is dependent on both the velocity ratio and the filling ratio between the constituent materials in the case of Bragg bandgaps [101]. Bragg gaps have centre frequencies corresponding to wavelengths up to two times the spatial period of the crystal. Recently investigated locally resonant band gaps, are typically centred at wavelengths at least two times larger than the spatial period of the crystal, and hence can achieve much lower frequency gaps compared to Bragg gap structures.

Different geometrical configurations of resonant structures have been employed to create low frequency band gaps, such as silicon cylindrical pillars [102] and annular holes [5] for SAWs, and cylinders with a split ring cross section [103] for photonic/phononic crystals. The dispersion relations of Rayleigh-like SAW modes propagating on an annular hole patterned  $128^\circ$  Y-X cut  $\text{LiNO}_3$  substrate are illustrated in **Figure 5.10**. The phase velocity of the Rayleigh wave (black dashed line) is lower than that of the transverse wave (blue solid line), as expected from the analysis of **Figure 5.9**. For the annular hole structure, the bandgap occurs at lower frequency i.e at 100 MHz compared to the silica microsphere structure which exhibits a bandgap around 200 MHz. Phononic crystal plates with periodic spiral resonators [104] have also been used to create low frequency bandgaps in the 100 Hz range. This type of interesting structure is used both by nature in the process of hearing (cochlea in human ear allows a certain

frequency range to pass through (200 Hz–20 000 Hz)), by humans to construct a metamaterial that acts as attenuator for chiral seismic waves [105], and as a broadband acoustic skin cloak [106]. Moreover, thanks to its structural degrees of a spiral resonator is a good candidate for allowing the tailoring of bandgap frequency and bandwidth. The dispersion relation analysis of a metasurface comprising spiral shaped local resonators interacting with SAWs will be given in Chapter 7.

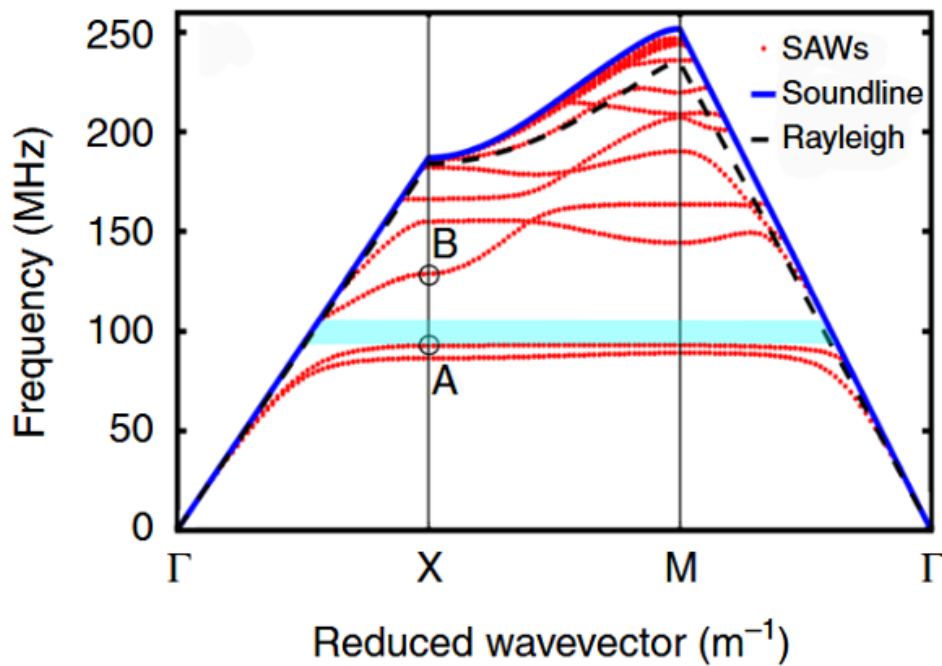


**Figure 5.10.** SAW band diagram generated through finite element method simulation of annular hole unit cell with pitch  $10.9 \mu\text{m}$ , inner radius  $3.1 \mu\text{m}$ , outer radius  $5.1 \mu\text{m}$  and hole depth  $6.4 \mu\text{m}$ . The blue line represents the soundline and the red lines represent propagating SAW bands within the 1st Brillouin zone. The teal bar represents the PnC complete bandgap. Taken from [5].

## 5.7 SAW applications

The interaction of SAWs with resonant structures patterned on a semi-infinite medium [102], [5] or on a slab [107], is very promising for various technological applications due to the ability to create bandgaps for SAW devices. Apart from the confinement of acoustic energy, which allows the realisation of wave-guides and cavities, SAW bandgaps can also be used in wireless communications [108] and sensor applications [109].

Specifically, the filter shown on **Figure 5.11 (A)** can be suitable for wireless communication applications such as duplexers [110]. The PnC consists of intrinsic ZnO pillars lying on a Si substrate. Locally resonant band-gaps are created prohibiting SAW propagation and a linear defect is introduced in order to achieve a SAW waveguiding behaviour. The defect guiding modes can be conducted into the local-resonance gap by adjusting the structural parameters of the defects. Conductivity ( $\sigma$ ) modulation, achieved by contactless UV illumination of the ZnO pillars, leads to tuning the defect frequency of the PnC or the guiding frequency of the filter owing to the acoustoelectric interaction. The inset schematically shows the frequency red shift of the filter's transmission peak because of the increased conductivity. The achieved maximum shift of the guiding frequency is about 100 MHz for a defect frequency of 4.18 GHz and a bandwidth of about 100 MHz.

A SAW biosensor is illustrated in **Figure 5.11 (B)**. The surface acoustic waves generated by the IDTs propagate along the surface of the substrate at a certain depth. Upon reaching the delay area, these waves will partially reflect. When target substances are immobilized and hybridized on the delay area, a thin superimposed molecular film is formed, which effectively alters the film thickness and density. This causes the velocity of the reflected signal to change, which in turn shifts the resonance frequency. The probe DNA's immobilization on the gold delay area surface is followed by hybridization of the target DNA with the probe DNA, as shown in the lower panels of **Figure 5.11 (B)**.

Elastic Bragg band gaps have also been exploited to create a shielding effect for Rayleigh waves propagating at 50 Hz through a soil structured with an array of boreholes [111] and the interest of controlling seismic waves has grown. The development of seismic metasurfaces capable of mode converting the destructive seismic Rayleigh waves into mainly harmless downward-propagating bulk shear waves, opened the door to the development of similar applications for other types of seismic waves such as Love waves [112].

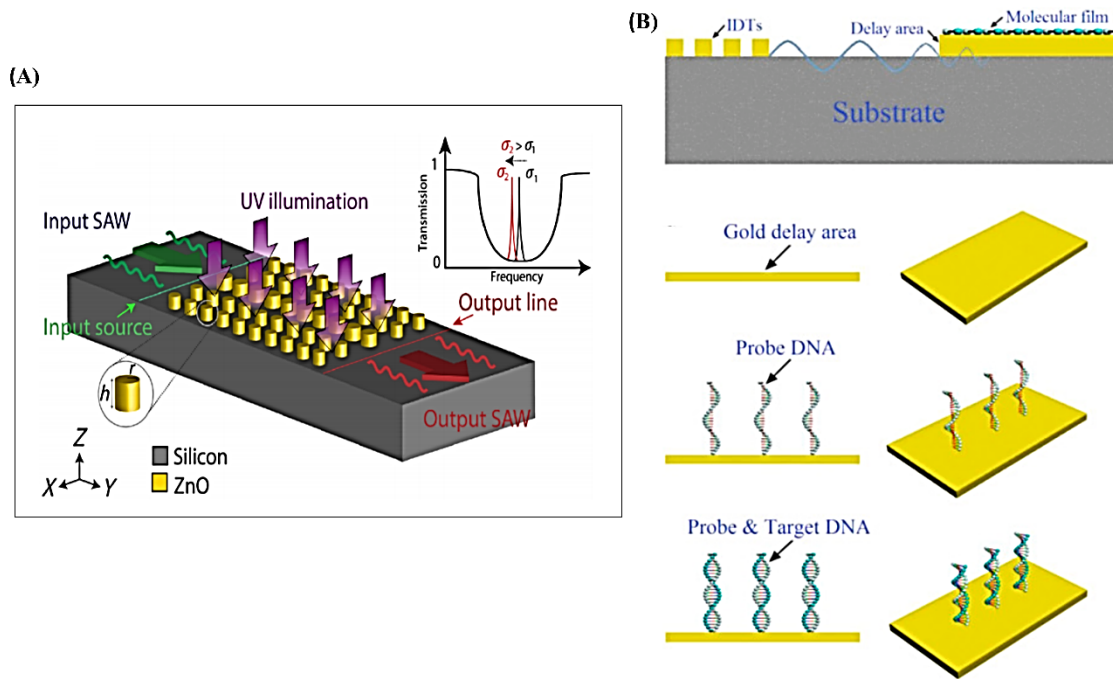


**Figure 5.11** (A) Schematic of the proposed SAW filter consisting of a ZnO-based PnC. The inset shows the transmission spectra of the filter, corresponding to two different conductivity values  $\sigma_1 > \sigma_2$ . Taken from [108]. (B) Upper panel: The effect of molecules' immobilisation on delay area and the sensing mechanism illustration of the biosensor. Lower panels: Process showing probe DNA immobilization on the gold delay area surface followed by hybridization of the target DNA with the probe DNA. Taken from [110].

## 5.8 Conclusions

On structures supporting ASWs, the pressure field profile decays exponentially in the direction normal to the surface, and the magnitude of momentum supported in the direction parallel to the surface significantly exceeds the momentum of sound in air. A trapped surface wave is formed at the proximity of an impedance mismatch boundary and the impedance discontinuity must be finite. Coupling between cavities allows the determination of the grating's effective impedance which affects waves' confinement to the surface and its value changes with frequency. For an ASW grating with one resonator per unit cell, there is only one standing wave at the Brillouin zone border because the rigid-wall approximation forbids the placing of the pressure fields inside the solid material. By contrast, for a SAW grating with one resonator

per unit cell, two standing waves are present because there is no sound hard boundary condition. From the explicit calculation of the Bloch wavefunctions it was deduced that at the Dirac frequency the ASW travels about 12 times slower than it does in free space. The existence of acoustic Dirac points allows for several interesting phenomena such as edge states, zero phase change propagation, defect immune property and the Talbot effect.

Interaction between a SAW and a metasurface induces a bandgap in the vicinity of the resonance frequency of a single resonator and gives rise to hybridised Rayleigh-like SAWs, lying below and above the resonant frequency. SAW bandgaps can be used in several applications such as waveguiding, wireless communications, sensing and seismic control related applications.

## CHAPTER 6

### **Experimental characterisation and numerical investigation of the bound ASWs supported by honeycomb and hexagonal hole arrays**

#### **6.1 Introduction**

As discussed in Chapter 5, Dirac cones have inspired many developments in the condensed-matter field over the last decade and the interesting physics of graphene has enabled the search for analogs in the realm of acoustics. In this chapter, using experimental techniques and numerical modelling, we will explore, in the vicinity of the deterministic Dirac points, the dispersion of acoustic surface waves supported by a solid plate patterned with a honeycomb array of ‘through’ holes, and compare with results from a hexagonal array of ‘through’ holes. The arrangement of holes in the honeycomb array is inspired by graphene, a two-dimensional (2D) allotrope of carbon in which three electrons form  $sp^2$  hybridized covalent bonds with the remaining electron held in the p-orbital perpendicular to the plane of the  $sp^2$ . The overlap of these p orbitals into a  $\pi$  band leads to the de-localization of charge carriers in graphene which dominates the electrical transport properties [113].

The experimental set up used to perform the acoustic measurements as well as the signal processing techniques used to deal with issues such as spectral leakage and background noise are described. The analysed experimental data are presented in different ways; an acoustic pulse propagating across the sample is shown at different time points, the pressure field distribution is shown at different frequencies, different intersections of the full dispersion relation with 2D planes in k-space are illustrated both in a 3D and 2D visualisations. Interesting features such as linear crossings and band gaps arising in the experimental dispersion relations are discussed and the results are compared with data derived from FEM calculations.

Since the attenuation of the acoustic surface modes is significant at the frequencies studied here, the analysis of acoustic surface losses are presented for the acoustic mode propagating in the  $\Gamma$  to K plane for honeycomb and hexagonal lattices.

## 6.2 Honeycomb and hexagonal arrays

The samples studied, shown in **Figure 6.1**, have holes milled through a plate with cylinder radius,  $r = 1.5$  mm, hexagonal lattice periodicity,  $a = 8.66$  mm, and plate thickness  $t = 8.0$  mm. The experimental samples were fabricated in aluminium alloy by milling each hole array geometry through plates of mean thickness  $t = 8.0 \pm 0.1$  mm. The hole array structures occupy a 400 mm by 490 mm area on the plate surface. As shown in the inset of **Figure 6.1** (b) the hole is located in the unit cell centre for the hexagonal array sample. By contrast, the honeycomb sample has two atoms per unit cell (**Figure 6.1** (a)), placed symmetrically with respect to the unit cell central point.

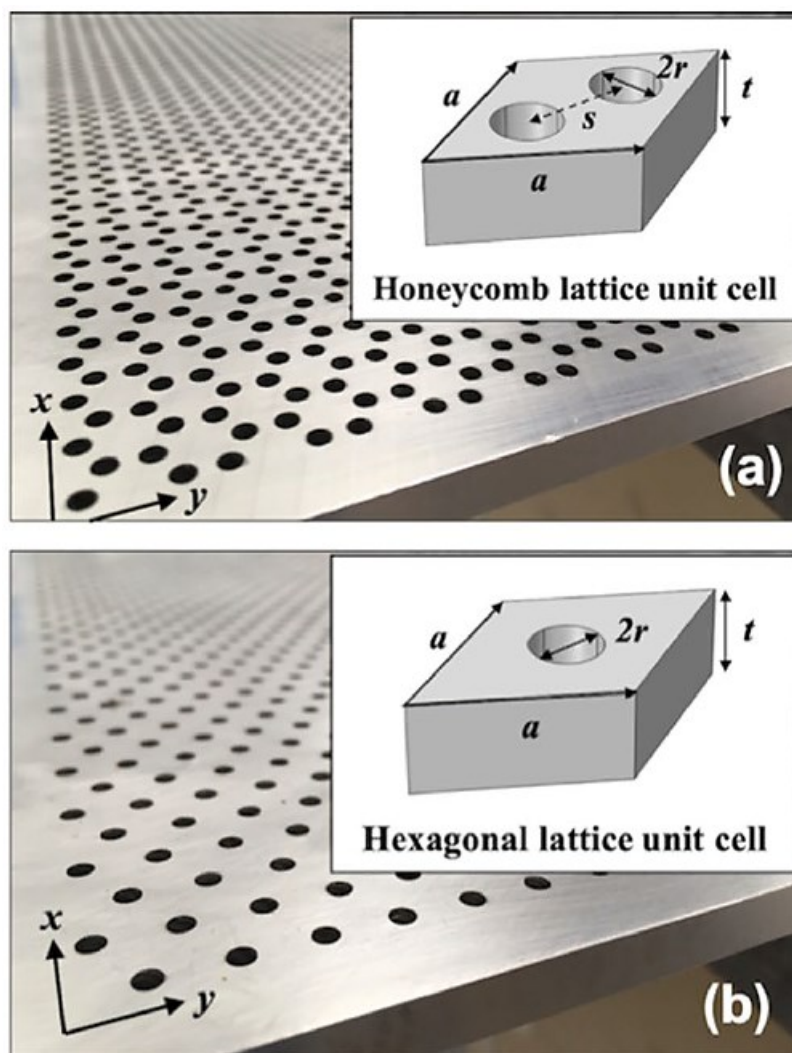


**Figure 6.1.** (a,b) Photographs of the aluminium samples and unit cell schematics (inset) for (a) the honeycomb array, and (b) the hexagonal array explored in the numerical modelling and

experiments. The nearest neighbour distance between holes for the honeycomb sample and the hexagonal sample is  $s = 5$  mm and 8.66 mm (not shown), respectively. The hole radius,  $r = 1.5$  mm, and the mean plate thickness (length of the open cavity),  $t = 8.0 \pm 0.1$  mm, are the same for both samples.

### 6.3 Experimental set up

Acoustic measurements of the surface wave pressure field used a fixed loudspeaker source and a detector on the opposite side of the sample on a xy translation stage. **Figure 6.2** displays a simple schematic of this experimental setup. Acoustic surface modes were excited using a modified Tucker-Davis Technologies MF1 near-field source positioned over a hole in the centre of the sample to diffractively couple sound to the surface modes. This source was excited with single cycle sine-Gaussian waveform with 16 kHz carrier frequency and the period of time over which the signal was recorded at each spatial point (also referred to as time window) was 32 ms. The sampling frequency was 312.5 kHz. The signal generator is capable of generating arbitrary waveforms and is connected to an amplifier which then powers the loudspeaker. The acoustic pulse type, its time window and the sampling step in time are controlled by a computer programmed with LabView.

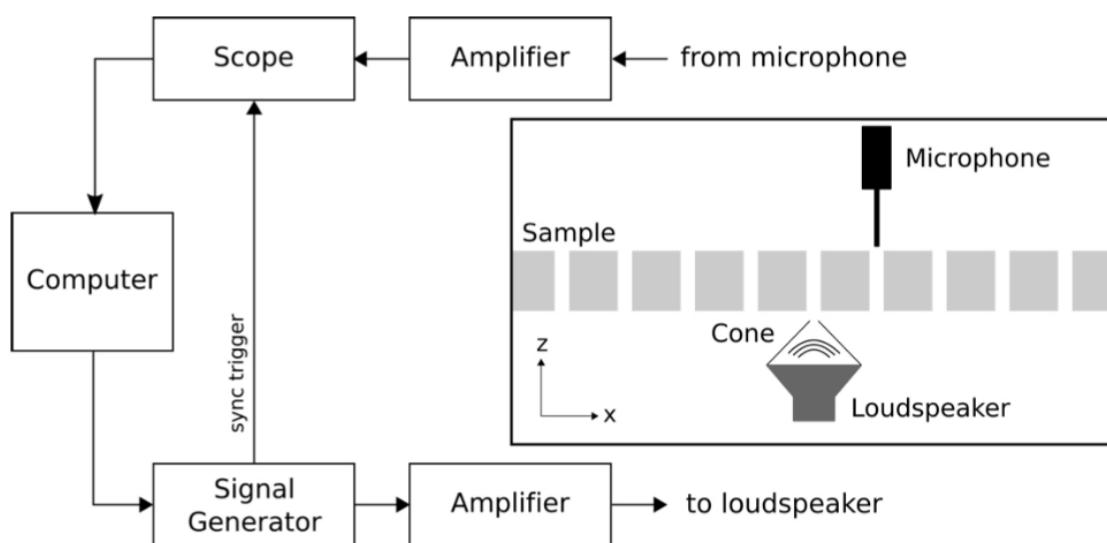


**Figure 6.2** A simple schematic diagram of the experimental method.

Surface wave propagation across the sample is measured with a Brüel & Kjær Type 4182 needle-tip probe microphone positioned on the opposite side of the sample and raster scanned in a plane approximately  $<0.4$  mm above sample surface using the translation stage. The detecting microphone was scanned in square grid with raster step size,  $\Delta x = \Delta y$ , of 1.5 mm, for a total scan length,  $x_{\max} = y_{\max}$ , of 400 mm. The microphone has a very small aperture protruding from a long metal tube so as to record near field signals without disrupting them significantly. The microphone is connected to an amplifier, allowing the user to adjust its sensitivity, which then sends the amplified pressure fluctuations to the connected digital oscilloscope (PicoScope) that can then split the signal into discrete points on the time axis, spaced  $\Delta T$  apart. The given discrete time signal must be converted from the time domain to the frequency domain, in order to see what frequency components make up the signal. To this end, the Fast-Fourier-Transform algorithm (FFT) is applied to the time signal. Commonly used signal processing techniques are described in section 6.4.

For the oscilloscope to start sampling in synchronisation with the pulse emission from the signal generator, the latter produces a rectangular “trigger” pulse that signals to the oscilloscope that the Gaussian pulse is about to be emitted. Both the loudspeaker source and the probe microphone are placed very close to the sample surface in order to achieve an evanescent excitation and detect the ASWs with as good signal-to-noise ratio as possible.

## **6.4 Signal processing and data analysis techniques**

### **6.4.1 Overview**

Several issues need to be considered when it comes to signal processing, such as background noise and reflections. As expected, when sound encounters a solid, impedance mismatch occurs and the acoustic wave is reflected. Hence, anything solid near the sample is likely to cause reflections interfering with the desired signal. This problem can be solved by using a relatively short duration pulse, allowing the desired time signal to be recorded before the reflected signal arrives at the detector. In order to reduce the effect of background noise, the average of multiple repetitions of the pulse is taken at each spatial point. For a typical scan with 5 repetitions per spatial point and commensurate step,  $\Delta x = 1.9\text{mm}$ , results were obtained after 24 hours.

The frequency spectrum resulting after applying the FFT function to the time signal has properties dependent on the time difference between two sampling points,  $\Delta T$ , the time window,  $T$ , the total number of sampling points,  $N$ , and the sample rate  $f_s$ , which is equal to  $\frac{N}{T}$  [114]. The frequency resolution of the resulting frequency spectrum is given by:

$$\Delta f = \frac{f_s}{N} = \frac{1}{T} \quad (6.1)$$

Hence, a selection of a short time window, which would solve the reflection problems gives rise to another issue; the low frequency resolution. A signal processing technique known as ‘zero padding’ is often used to solve this problem. According to (6.1), by increasing the time window, better frequency resolution can be achieved. Therefore, if time-points, spaced  $\Delta T$  apart, with no amplitude (zeros) are added at the original time signal, the time window is artificially increased without affecting the original time signal.  $\Delta f$  is also referred as frequency bin and if, for example, the original time signal is a 1 Hz sine wave, all of the Fourier amplitude must be contained in the 1 Hz frequency bin. However, in real-world signal analysis this is not always possible since the sampling rate may be such that  $\Delta f < 1$  Hz. Consequently, the Fourier amplitude could be distributed to more than one frequency bins, a phenomenon known as ‘spectral leakage’ [114]. It is worth noting that the frequency axis arising after applying FFT followed by FFT-shift function (which places the DC component in the centre of the signal) is dependent on the time samples,  $N$ . Significantly:

$$f = \begin{cases} -f_{max}, -f_{max} + \Delta f, \dots, 0, \dots, (f_{max} - \Delta f) & \text{if } N \text{ is even} \\ -\left(f_{max} - \frac{\Delta f}{2}\right), -\left(f_{max} - \frac{\Delta f}{2}\right) + \Delta f, \dots, 0, \dots, \left(f_{max} - \frac{\Delta f}{2}\right) & \text{if } N \text{ is odd} \end{cases} \quad (6.2)$$

The maximum frequency,  $f_{max}$ , that can be captured accurately in time signal analysis is dependent on the sample rate. For instance, if the 1 Hz sine wave is sampled at  $f_s=1$  Hz, the signal that one can capture is up to 0.5 Hz. By contrary, if the 1 Hz wave is sampled with 2 samples per cycle ( $f_s = 2$  Hz), the maximum frequency that can be captured is  $\frac{f_s}{2}$ , which is 1 Hz and the frequency of the original wave is captured accurately. The maximum frequency it is possible to capture from a discrete time signal is known as the Nyquist-Limit and it coincides

with either the positive or the negative maximum bin of the even sample, as shown in (6.2). On the contrary,  $f_{\max}$ , falls  $\frac{\Delta f}{2}$  off the maximum frequency bins of the odd sample. From (6.2) it is also deduced that the frequency space produced after the application of the FFT function to the time-domain data has a positive and a negative half. However, the negative half of the frequency space is always the mirror image of the positive half and hence, it is not shown in experimental 1D FFT results.

Spectral leakage can also occur if the recording window is not exactly commensurate with the wavelength of the signal. The FFT function treats the time signal as though it repeated infinitely in both positive and negative time around the start point and hence if the first and last points of the recorded signal have zero change in amplitude an artificial flat feature is produced leading to a broad feature in frequency. As a result, the frequency bins surrounding the real signal have non-zero amplitude.

Another method that has been developed to account for spectral leakage is the use of the most appropriate window function. Windowing reduces the amplitude of the discontinuities at the boundaries of each finite sequence acquired by the digitizer. The less commonly used function multiplying the original signal is the rectangular window function [115], which has a value of one for some defined width while being zero elsewhere. On the contrary, the ‘Hanning’ window [116], [117] which is used in this Thesis smooths the observed signal over the edges of measured time interval and gradually reduces it to zero, as it is demonstrated in **Figure 6.3**. The time domain is shown in the left panels and the time signal before and after the Hanning window is applied is shown in red and blue solid lines respectively.

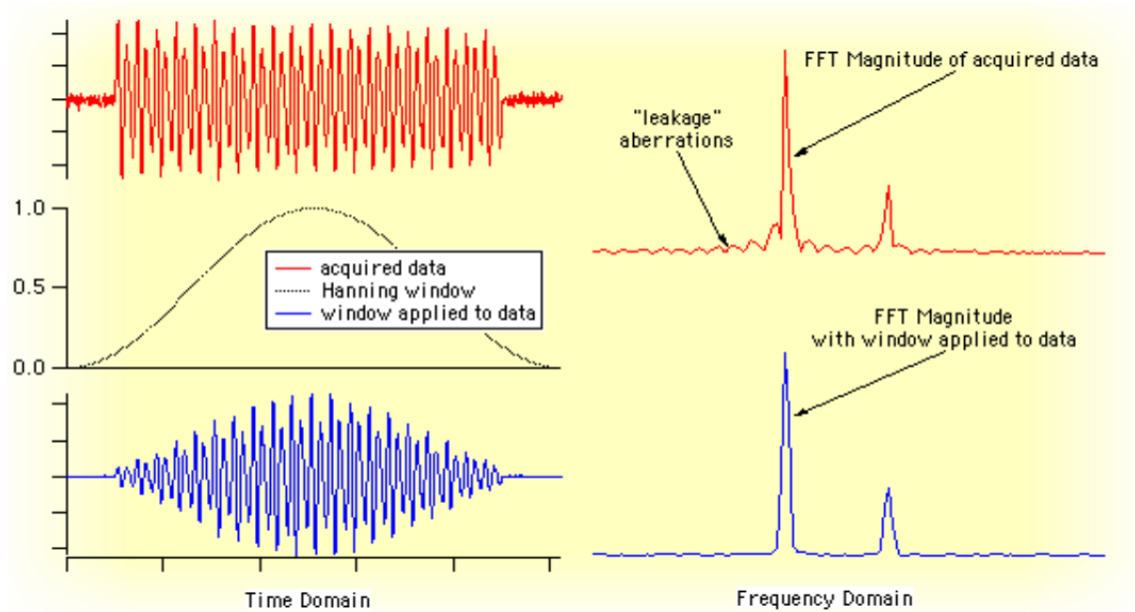


**Figure 6.3** Left: The effect of applying a Hanning window to time domain data. Right: FFT magnitude of the data shown on the right panels. Taken from [118].

The right upper panel shows the result of the FFT function applied to the acquired data and the leakage aberrations (also referred to as side lobes), appearing either side of the fundamental peak, are clearly seen. However, when the FFT function is applied to the windowed data, the spectral leakage is significantly reduced, as shown in the right lower panel.

Although the Hanning window has been used for the time series analysis in the present Thesis, it is worth mentioning that there are numerous other window functions, which may be more appropriate if the accuracy or the sharpness of the main peak is sought. A comprehensive catalogue of data windows along with their significant performance parameters are given in [119].

#### 6.4.2 Temporal Fourier analysis-2D pressure field maps

Pressure field maps are obtained after the temporal signals are Fourier transformed. First, the time domain data are sorted in ascending time and position and after the FFT function is applied, two-dimensional matrices of complex values are obtained at each frequency bin. The real part of the complex number is the instantaneous pressure field whereas the absolute value of the complex number is the absolute pressure field at the corresponding frequency bin. An example of the time-space map of an acoustic pulse propagating across the sample surface is

shown in **Figure 6.4** (a)-(c) and it is indicated that the time  $t$  it takes the pulse to travel from the centre of the sample to its edges is greater than 0.5ms. Examples of the instantaneous pressure field distribution at different frequencies are demonstrated in **Figure 6.4** (d)-(f) and the six-fold lattice symmetry can be observed.

### 6.4.3 Spatial Fourier analysis- Full dispersion relation

In order to derive the dispersion relation for the acoustic samples described in section 6.2 a 2D FFT is performed on a two-dimensional matrix of complex values (which is the result of the temporal FFT, described in the previous section). The k-space resolution  $\Delta k_x$  arising from the 2D FFT is dependent on the step size  $\Delta x$ , specifically  $\Delta k_x = \frac{2\pi}{N_x \Delta x}$ , where  $N_x$  is the total number of steps in the real space direction. The maximum wave vectors accessible are  $k_{x,max} = \frac{\pi}{\Delta x}$  and  $k_{y,max} = \frac{\pi}{\Delta y}$ . As with the 1D case the k-space axis are dependent on the number of samples and the FFT-shift function is again applied in order to place the low k components in the centre and the high k components on the edge. The k-axis in the x direction is:

$$k_x = \begin{cases} -k_{x,max}, -k_{x,max} + \Delta k_x, \dots, 0, \dots, (k_{x,max} - \Delta k_x) & \text{if } N_x \text{ is even} \\ -\left(k_{x,max} - \frac{\Delta k_x}{2}\right), -\left(k_{x,max} - \frac{\Delta k_x}{2}\right) + \Delta k_x, \dots, 0, \dots, \left(k_{x,max} - \frac{\Delta k_x}{2}\right) & \text{if } N_x \text{ is odd} \end{cases}$$

It should be noted that positive and negative halves of the resulting k-space do not necessarily mirror each other because the matrix obtained from the temporal Fourier transform is a matrix of complex values. The experimental results for a honeycomb sample comprised of cylindrical cavities, each of which is 7.4 mm in depth is shown in **Figure 6.5**. The nearest neighbour distance between the through holes is 5 mm. The Brillouin zone borders in k-space, are denoted with vertical solid white lines and the letters are used to discriminate the different planes in k-space. For instance, for  $k_x$  fixed at zero, the letter M is used whereas for  $k_y$  fixed at zero or 418.88 (1/m) the letters K and K'' are used respectively. The numbers in the parentheses describe the exact coordinates  $(k_x, k_y)$  of the Brillouin zone borders. It can be seen that the quadrant having negative  $k_x$  values and positive  $k_y$  values is not the mirror image of the quadrant having negative  $k_x$  and  $k_y$  values. Note that the full dispersion relation  $(k_x, k_y, f)$ , (produced by applying temporal and the 2D FFT) are not shown in **Figure 6.5** in order to allow

better visualisation of the dispersion on three planes; the  $\Gamma$ -K plane , the M-K plane and the  $\Gamma$ -M plane (which is orthogonal with respect to  $\Gamma$ -K and M-K planes). In the forthcoming sections dispersion relations on different planes will not be presented in a 3D visualisation (as in **Figure 6.5**) but in a 2D visualisation to allow simplicity. In other words, the intersections of the full dispersion relation with an appropriate 2D plane will be shown. The intersections of the  $k_x$ - $k_y$  plane at a fixed frequency will be referred to as isofrequency contour plots. One quadrant ( $k_x < 0, k_y > 0$ ) of an isofrequency contour plot at  $f=16$ kHz is shown in the upper panel of **Figure 6.5**. The dispersion of the surface mode(s) correspond to data that lie outside the sound line, explicitly data with larger magnitude of in-plane momentum,  $k_{||}$ , than that of a free-space grazing acoustic wave. At  $f=16$  KHz the surface mode (red colour) has larger FFT magnitude compared to the free-space wave (yellow colour) since the source was excited with 16 kHz carrier frequency and the overlap of frequency- and wavevector- spectra of source and surface mode is stronger around this frequency. For higher frequencies however, we observe that the surface mode's coupling to the source is less strong. Specifically, we observe that the upper frequency surface mode at M point ( $(k_x, k_y) = (0, 418.88)$  (1/m)) has smaller FFT amplitude (light blue colour) compared to the lower frequency surface frequency mode (red colour). A different set of planes intersecting the full dispersion relation can be seen in the lower panel of **Figure 6.5**. Specifically, two planes having the  $k_y$  fixed while the frequency is spanning over the range [16.5, 18.5] [kHz] and the  $k_x$  is spanning over the range [-600, 600] [1/m] are shown.

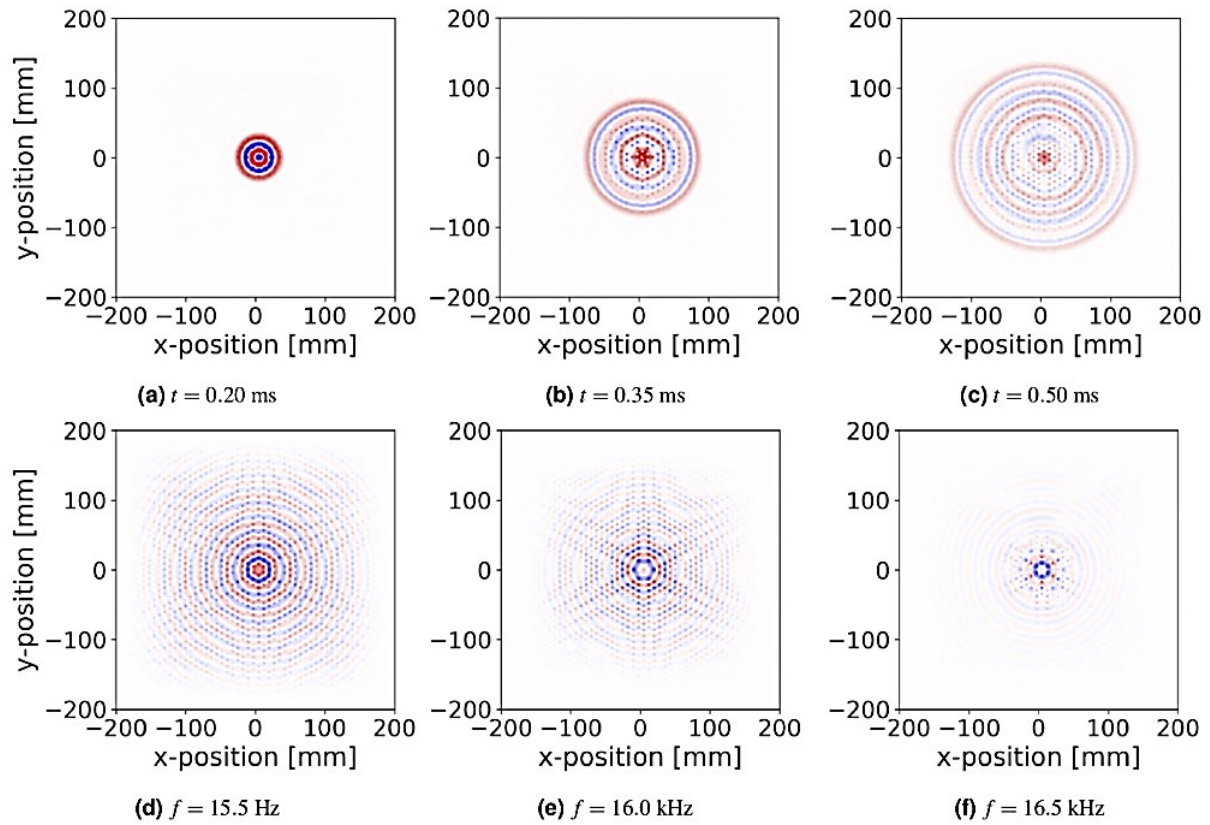


**Figure 6.4** Exemplar experimental data for the hexagonal lattice measurement: panels (a) - (c) display the signal (voltage) map of the acoustic pulse propagating across the hexagonal lattice at three times,  $t$ , after the pulse is triggered from a source at the centre of the sample. Panels (d) - (f) display the instantaneous pressure field for three different frequencies,  $f$ , which visually shows the 6-fold lattice symmetry.

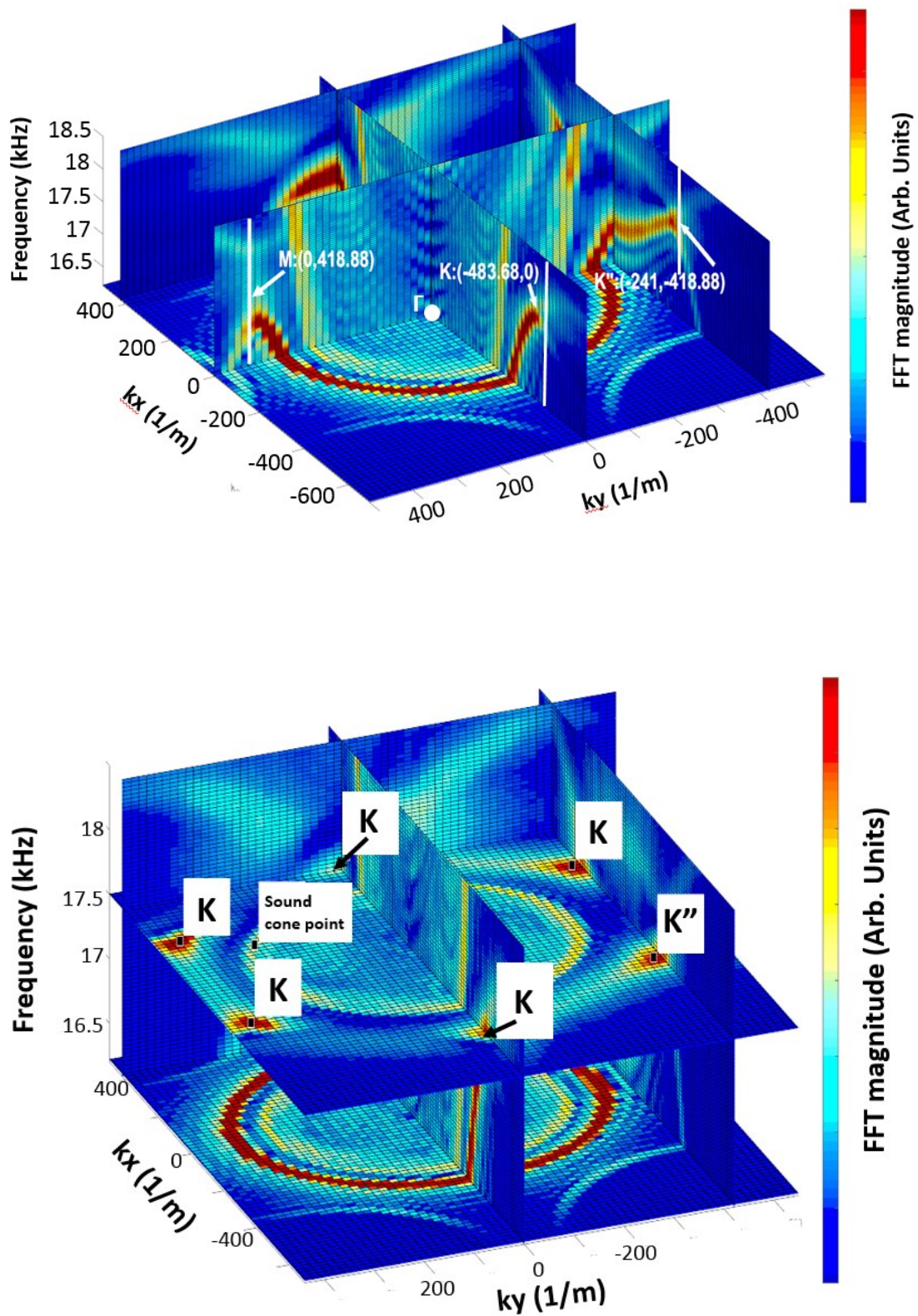


**Figure 6.5.** Five 2D planes intersecting the full dispersion relation ( $k_x$ ,  $k_y$ ,  $f$ ). Upper panel: Solid vertical lines indicate the first Brillouin zone borders. Letters K, M and K'' mark the high symmetry points and numbers in parentheses describe the  $k$ -space coordinates at each

high symmetry point, i.e  $(k_x, k_y)$  . Lower panel: Isofrequency contour plots intersecting the  $k_x$ - $k_y$  plane at a  $f = 16$  kHz and  $f = 17.5$  kHz. At  $f = 17.5$  kHz the surface modes are localised at K points. The magnitude of momentum at these points in both  $k_x$  and  $k_y$  directions significantly exceeds the momentum of the point lying in the sound cone.

The same planes have already been illustrated in the upper panel of **Figure 6.5**, (as expected by observing the K and K'' points in both figures) but this perspective allows us to demonstrate the symmetrical points with respect to  $k_x = 0$  axis. The isofrequency contour plot at  $f = 17.5$  kHz illustrates the surface modes localised at the K points although there is no such localisation at  $f = 16$  kHz. The K points are lying in the 1<sup>st</sup> Brillouin zone border. In the rest of the thesis the K'' point will also be referred to as K point to allow simplicity and the dispersion will be plotted to values beyond the first Brillouin zone , since the experiment allows for good resolution of modes far out in momentum space. A point lying in the sound cone is also shown. All data with momenta values smaller than the sound cone correspond to direct sound transmission between the source and microphone detector, or other unwanted noise, and are not discussed. When the sound cone is projected in a 2D plane the term sound line will be used to describe the border between the radiative and the non-radiative regime.

In the rest of this chapter dispersion curves are plotted with a greyscale indicating the Fourier intensity without normalisation to show the relative strength of features within the plots. All dispersion data presented has undergone real-space windowing of the complex pressure field using a symmetric tapered cosine-window with shape parameter,  $\alpha = 0.5$  before being Fourier transformed and zero-padded by a factor of 3. All data was processed using the SciPy and NumPy packages and plotted using Matplotlib in Python.

#### 6.4.4 Experimental data analysis- Curve fitting

To provide an indication of the surface mode loss, the momentum,  $k$ , and momentum width,  $\Delta k$  of the modes was found by fitting the asymmetric Lorentzian peaks [120]. Peaks were fit to the mode propagating in the positive and negative  $k$ -directions independently and results averaged.

## 6.5 Simulation results

Surface mode dispersion was calculated using the Finite Element Method (FEM) modelling package, COMSOL® (version 5.3a) [121]. The basic principles of FEM modelling have already been discussed in Chapter 4. The dispersion relations presented are the eigenmodes of rhombic unit cells with repeat Floquet-periodic boundary used to represent an infinite surface. These unit cells have been displayed in **Figure 6.1(a,b)**. The model assumes the holes are cylindrical cavities perforated through an acoustically-rigid plate of thickness,  $t$ . The acoustic loss that arises due to the no-slip and isothermal boundary condition at the fluid-solid interfaces are accounted for (implemented using the pressure acoustic and thermo-acoustic modules); for the geometries and frequencies studied here, loss causes a small (approx. 0.5 kHz) reduction in the frequency of the modes at the Brillouin zone when compared a loss-less system. The dispersion relations as a function of in-plane momentum  $k_{||} = \sqrt{k_x^2 + k_y^2}$  where  $k_{x|y}$  is the momentum in  $x|y$  direction), obtained using Finite Element Method (FEM) eigenvalue numerical simulations, between points of high symmetry ( $\Gamma$ ,  $K$ , and  $M$ ) are shown in **Figure 6.6**.

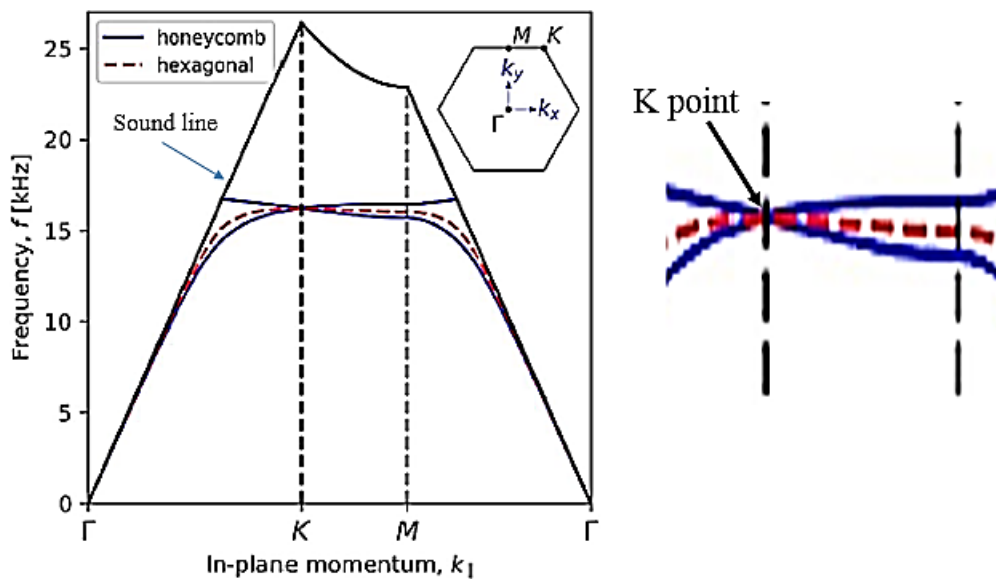


**Figure 6.6.** Numerically (FEM) calculated band structure of the acoustic surface waves for samples in **Figure 6.1 (a,b)**. The sound line, calculated for sound propagating with velocity,  $c = 342 \text{ m s}^{-1}$ , is shown as a solid black line, and the vertical dashed lines indicate the Brillouin zone edge at the  $K$  and  $M$  points. Inset: shows the points of high symmetry in momentum space for both lattices. On the right side a zoomed in section of the dispersion relation is shown so that the band crossing at  $K$  point is clearer.

These eigenvalue solutions show both honeycomb and hexagonal hole array structures support bound acoustic surface waves, as indicated by solutions that are bound within the sound line (black line), i.e. in the non-radiative regime. In the vicinity of each  $K$  symmetry point, the dispersion curve for the honeycomb structure is linear and exhibits a Dirac crossing of two surface modes, whilst at the  $M$  point a band gap exists. For the hexagonal array, the dispersion shows a different behaviour; only one surface mode crosses both the  $K$  and  $M$  symmetry points at frequencies close to the crossing point of the honeycomb array. Both arrays show relatively flat dispersion in the proximity of  $K$  point for the structure dimensions considered here.

## 6.6 Experimental results

**Figure 6.7** displays the measured dispersion curves in the  $\Gamma$ - $K$ ,  $M$ - $K$ , and  $\Gamma$ - $M$  directions in momentum space for both the honeycomb array and the hexagonal array. The lowest order surface modes are shown, for which there are two for the honeycomb and one for the hexagonal array, as determined by the available number of degrees of freedom of the unit cell (i.e. here this corresponds to the holes per unit cell). These surface modes are excited via diffraction through the hole at the centre of the scan area, the so called point-like acoustic excitation. The surface modes are associated with the diffraction between cavity resonances supported by quantisation of the pressure field in the cavity depth; here, the cavity resonances have the approximate character of a half-wavelength pipe modes ( $\lambda/2$  resonance) within the open holes, and are coupled by diffraction near their resonant frequency producing an eigenmode that is strongly localised to the top and bottom interface of the structured surface, which decays exponentially from the surface. Experimental data are compared to numerical simulations for the range of momenta lying beyond the sound line (as shown in **Figure 6.6**) and inside the first Brillouin zone (dashed lines). For the honeycomb array (see **Figure 6.7(a-c)**), experimental results (greyscale data) agree well with numerical simulations (open circles), with one exception; the upper branch of the Dirac cone in the  $\Gamma$ - $K$  direction (**Figure 6.7(a)**) is present in the model, but is not observed experimentally in the first Brillouin zone. Conversely, the existence of the upper branch is shown in the  $M$ - $K$  direction for the honeycomb sample (**Figure 6.7(b)**) beyond the  $K$  point towards  $\Gamma$  at higher momentum, where it meets the lower branch at the Dirac frequency,  $f_D = 16.5$  kHz. The absence of the upper branch in the  $\Gamma$ - $K$  direction within the first Brillouin zone is a consequence of the asymmetry of the mode pressure field with respect to its propagation direction. In an equivalent study of microwave honeycomb structures, Dautova *et al.* show that a non-zero valued reciprocal lattice vector,  $G$ , is necessary to observe

the upper branch of mode above the Dirac frequency [122], due to a vanishing integral in the Fourier intensity for a mode with an anti-symmetric field distribution. The data in **Figure 6.7**, confirms this analysis; the upper branch is never observed in the first Brillouin zone, but becomes present beyond the Brillouin zone boundary into the second zone (prominently shown in panel (b)).

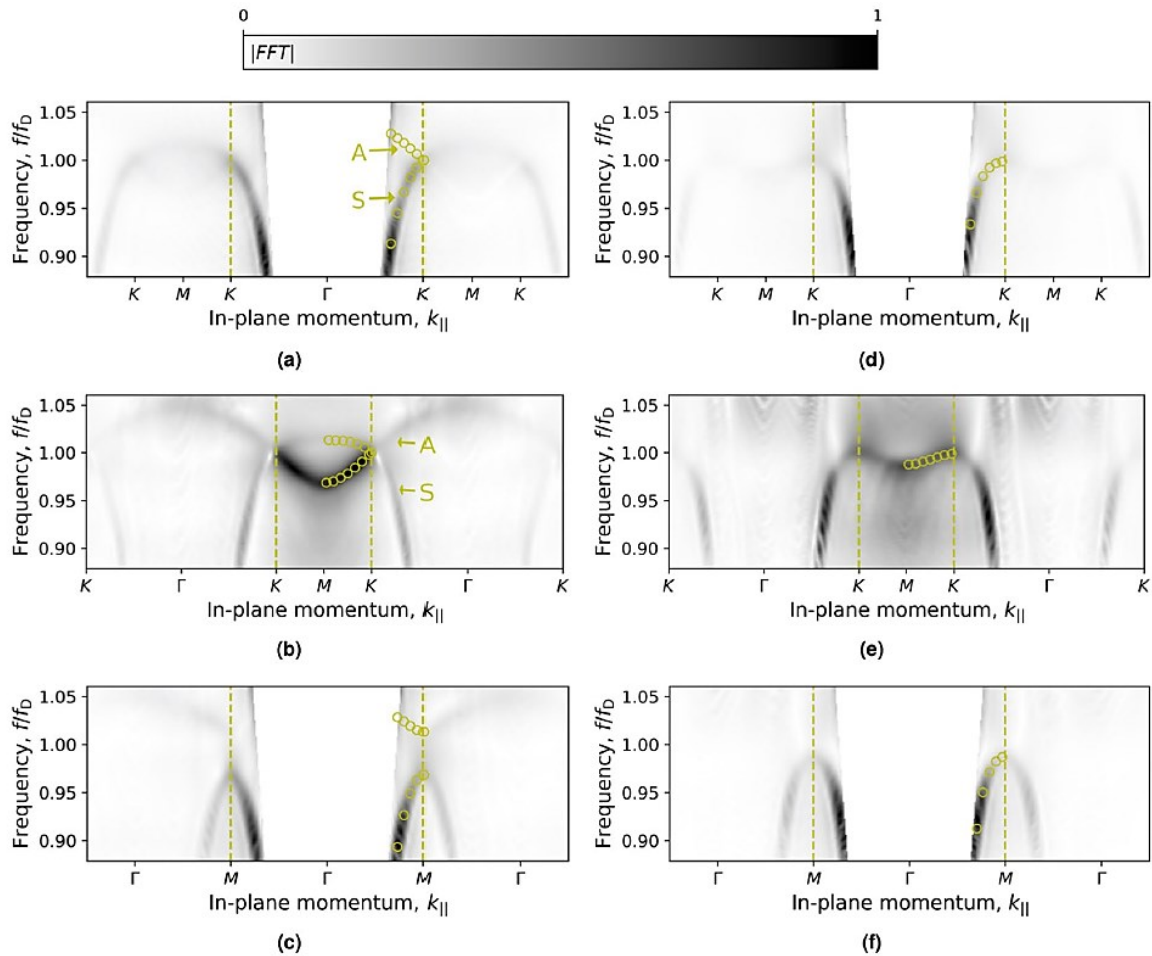


**Figure 6.7.** Dispersion measurements and numerical predictions for the honeycomb, left panels (a–c), and hexagonal structure, right panels (d–f). Measured data (greyscale) is shown as the Fourier intensity, and the simulated data (open circle points) is shown for positive momenta in the first Brillouin zone (indicated by the dashed lines). Top panels show dispersion on  $\Gamma$ - $K$  plane (with  $k_y = 0$  fixed, and  $k_x$  varying); middle panels show dispersion on  $M$ - $K$  plane (for  $k_y = -2\pi/a$ , and  $k_x$  varying); bottom panels show dispersion on the  $\Gamma$ - $M$  plane (with  $k_x = 0$  fixed, and  $k_y$  varying). White areas mask the radiative regime (i.e. from  $\Gamma$  to the sound line), and the labels  $A$  (anti-symmetric) and  $S$  (symmetric) on panels (a,b) denote the mode pressure field symmetry with respect to the mode propagation direction.

By plotting the dispersion data (honeycomb) beyond the first Brillouin zone, the modes coming from higher-order diffraction points are clearly seen, being particularly prominent in the  $M$ - $K$  and  $\Gamma$ - $M$  directions (**Figure 6.7** (b,c)) as the modes folded back from large positive and negative momentum states cross at the  $K$  and  $M$  points. From **Figure 6.7** (a,c) it is evident that the surface mode behaviour is quite different; the mode at  $K$  clearly has real group velocity (as expected at Dirac-like points), whilst the mode approaching the Brillouin zone at  $M$  from  $\Gamma$  has zero group velocity producing two standing wave states of different energy. The experimental results for the hexagonal sample (see **Figure 6.7** (d-f)), also show good agreement with the surface mode predicted by numerical simulations, but unlike the honeycomb, the hexagonal sample does not exhibit a Dirac point.

Further insight into the dispersion of these surface modes is obtained by imaging the dispersion on a momentum plane at a fixed frequency (an isofrequency map), providing information within the planes between points of high symmetry. **Figure 6.8** shows this data at frequency,  $f_b$ , corresponding to the Dirac point (in the honeycomb system) for both samples studied. In these graphs, the radiative components are masked by a white circle. At the edge of this circle, there is a dark ring that corresponds to the sound line, beyond which are the surface modes localised at the  $K$  points.



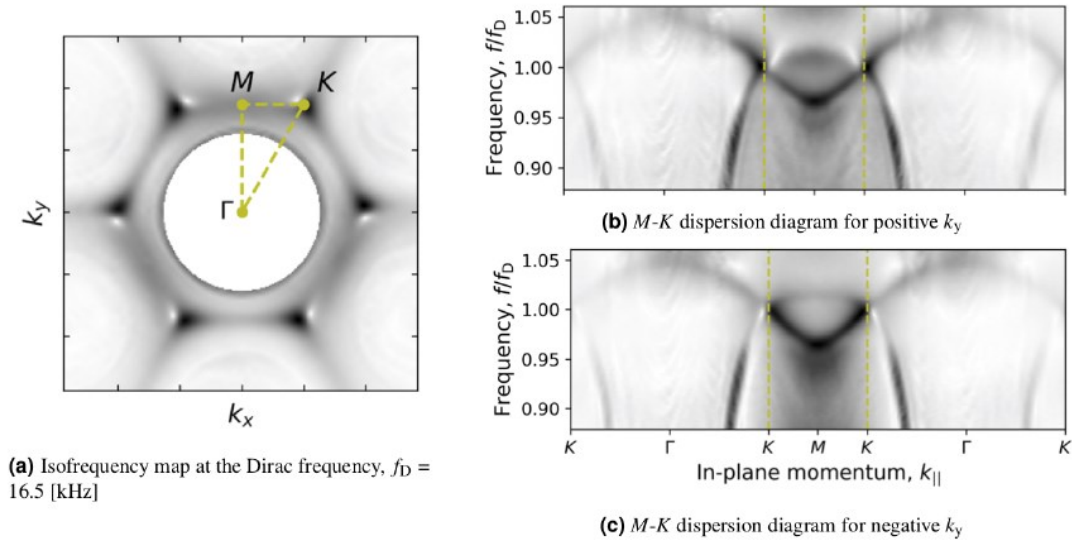


**Figure 6.9.** Dispersion data for honeycomb lattice demonstrating the 3-fold symmetry related to the coupling of the point source: (a) shows isofrequency map at the Dirac frequency, (b) and (c) displays dispersion diagrams for the  $M$ - $K$  lattice plane at the first Brillouin zone for positive and negative  $k_y$  respectively (as dictated by panel (a)).

Experimentally we have shown that both honeycomb and hexagonal arrays of holes in an acoustically rigid material support bound acoustic surface waves. Results show the existence of the Dirac point and the linear dispersion of acoustic surface waves supported by the honeycomb lattice, but not for the similar hexagonal lattice. The modes of the honeycomb lattice at the  $K$  and  $M$  high symmetry points are interesting because one exhibits a band gap and the other does not. To further interpret the nature of these modes, computed and measured real-space pressure fields are studied for the honeycomb sample. Such analysis can be used to understand whether a band gap or a crossing of the surface modes exists, and is an approach that has been used to describe dispersion relations in terms of the spatial symmetries of resonance states, for instance, in Sakoda [123] and in Li *et al.* [124].

To image the pressure field distributions for modes near the points of high-symmetry, small area (15 mm by 15 mm) high spatial resolution scans were made. The pressure field distributions are selected by frequency and propagation direction; the experimental data in **Figure 6.10** is obtained from small area scans and the Fourier analysis of the time domain data only. The small area scan and data analysis were carried out by Dr. Tim Starkey. The pressure field data is then presented at frequencies that correspond to the frequency of the mode at the  $K$  point and of the upper and lower branch at the  $M$  point. The small measured areas, measured

some distance from the source in either the  $x$ - or  $y$ - direction, allow the surface mode field profiles to be selected based on their propagation direction in real space (modes at  $K$  and  $M$  are present in real space at 90 degrees to one another). We note that because the modes are selected by frequency and propagation direction -not frequency and wavevector - all wavevectors of that frequency are present in the measured fields, the surface wave being dominant, due to the close proximity of the detector to the surface. The distance from the 2D scan area to the source was a critical factor in recording high quality data that can be usefully interpreted; close to the source the imaged fields are dominated by cylindrical spreading of wavefronts, whilst further away, the surface wave pressure amplitude suffers due to thermo-viscous losses at the sample surface. The  $K$  point (see **Figure 6.10**) scan was taken approximately 116 mm from the source in the  $x$ -direction, whilst field maps at the  $M$  point are taken at approximately half that distance in the orthogonal direction.

**Figure 6.10** compares the calculated and measured fields at  $K$  and  $M$  for the honeycomb lattice. Simulated pressure fields are the calculated eigenmodes when the in-plane momentum is equal to the momentum of the symmetry point (with appropriate boundary conditions on the unit cell). Measured pressure fields are presented at the frequency at which that mode meets the Brillouin zone. **Figure 6.10** (a,b) show the computed eigenmode solutions close ( $k_{\parallel} = 0.99k_K$ ) to the  $K$  point in order to break the degeneracy of the two solutions when  $k_{\parallel} = k_K$ . The pressure field distribution for the lower branch of mode is symmetric, whereas the pressure field for the upper branch is anti-symmetric with respect to the  $\Gamma$ - $K$  vector (the direction of propagation in real space). Commonly in the literature, the fields (pressure or otherwise) of larger scale systems are compared to electron wavefunctions in atomic systems. Here we note these pressure field distributions show great similarity to the so-called  $p_x$  and  $p_y$  ‘photonic orbitals’ of ref. [125] and are referred to as acoustic pseudo-spin dipolar states in analogous acoustic systems [126]. Apart from visible attenuation of the measure pressure field, from left to right of the figure (**Figure 6.10** (c)), data for the lower branch of the mode agree well with simulations. There is no experimental pressure field configuration for the upper frequency mode since we have not been able to detect this experimentally due to attenuation and the mode group velocity.

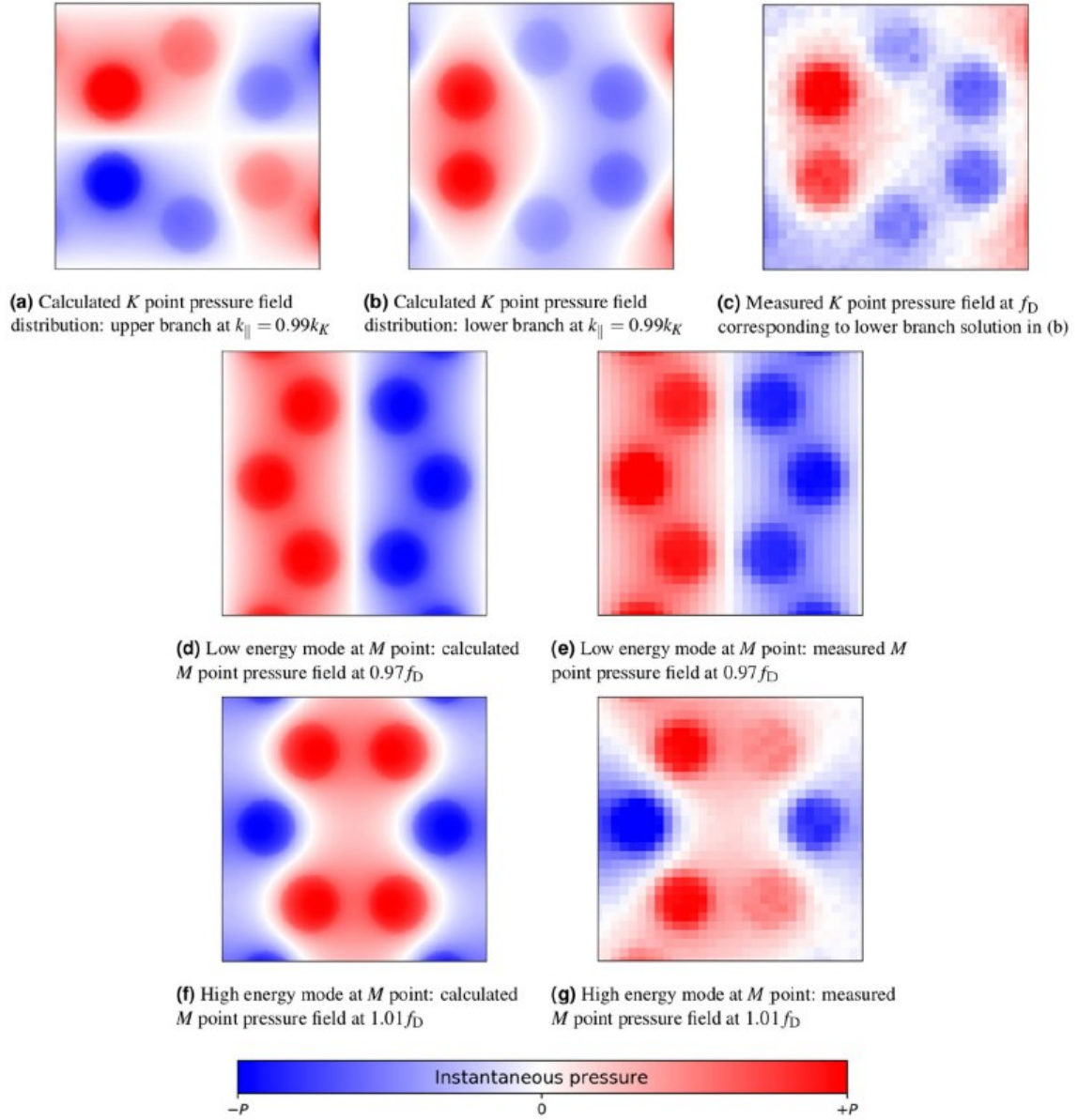


**Figure 6.10.** Calculated (frequency- and wavevector-selected) and measured (spatially- and frequency-selected) acoustic pressure fields for the honeycomb structure for modes at  $K$  and  $M$  points: (a–c) show field distributions at the Dirac frequency for the surface mode propagating along the  $\Gamma$ - $K$  direction at the Dirac frequency  $f_D$  (experiment) and  $K$  point,  $k_K = 4\pi/3a$  (model). (d, e) Show field distributions for the lowest energy mode at frequency  $f = 0.97f_D$  (experiment) and  $M$  point,  $k_M = 2\pi/a \sqrt{3}$  (model). (f, g) Show equivalent plots the upper mode at  $f = 1.01f_D$ . Red and blue indicate the maximum positive and negative pressure respectively. Model data is obtained by numerically evaluating the pressure field on the sample surface at the appropriate in-plane wavevector and frequency. The experimental pressure field is by obtained from the Fourier transform of the temporal field measured with the microphone tip approximately  $100 \mu\text{m}$  above the surface over a  $15 \text{ mm}$  by  $15 \text{ mm}$  area scan, and selecting the required frequency.

The centre coordinates of each measured field map (**c**, **e**, **g**) are  $(x \text{ [mm]}, y \text{ [mm]}) = (116.5, -2.5)$ ,  $(5, 62.5)$  and  $(0, 55)$  respectively, relative to the source. Note: figures are orientated so that surface modes would be travelling from left to right on the page. **Figures (c), (e) and (g)** were extracted by Dr. Tim Starkey.

The calculated pressure fields at the  $M$  point band gap in **Figure 6.10** (d,f) for the lower and upper band. These are two standing wave solutions, as expected for a mode at the Brillouin zone with zero group velocity, and have symmetric pressure field distribution with respect to the propagation direction. As before, the experimental pressure field distributions (**Figure 6.10** (e,g)) show good agreement with those predicted by the model. The symmetry of the crystal lattice causes a pair of symmetric Bloch states at the  $M$  point that result in a band gap, not a Dirac point. Whilst the asymmetry of two degenerate modes at the  $K$  point are characteristic of the deterministic degeneracy of Bloch states imposed by the symmetry of the crystal lattice, and have been studied in related acoustic systems [127].

As alluded to above, in the experimental field maps and in **Figure 6.9**, the attenuation of these acoustic surface modes is significant at the frequencies studied here. For instance, the pressure field distribution in **Figure 6.9** (c) clearly shows that the surface mode is highly localised to the source, as the mode approaches the Dirac frequency where the mode group velocity approaches zero and loss is significant. Recent studies have explored such losses by implementing Laplace transform techniques in order to retrieve the imaginary component of the wavevector [128]. Here, the attenuation of the modes approaching or travelling through the  $K$  point is quantified through the width of the mode in momentum. Data is fit at each frequency by a skewed Lorentzian distribution for modes propagating with positive and negative momentum and the full-width at half-maximum (FWHM) is estimated.

The FWHMs for a fixed frequency/ fixed momentum are shown in the left/right panels of **Figure 6.11** respectively. The Dirac frequency as well as the momentum at the Brillouin zone boundary are denoted with horizontal and vertical black dashed lines. The regions near the dashed lines are the regions of interest (ROF) since simulation results have predicted slow sound propagation for both honeycomb and hexagonal arrays at the Dirac point. We observe monotonic increase of the losses (widths) at the ROF for both honeycomb (blue dots) and hexagonal (red dots) arrays. However, away from ROF, the increase of width is not monotonic; at certain frequency regions losses increase whereas a decrease in loss can be seen at other frequency regions. As explained in [128],[129] losses prevent the effective propagation of slow

sound as the dispersion curve approaches the Bragg limit. Our experimental results show that losses decrease at very narrow frequency regions close to the ROF. Obviously, maximum value of slowness (minimum value of group velocity) does not occur at these regions but the dispersion of the hexagonal array is almost flat over a significant frequency range close to the ROF, as shown in the right panel of **Figure 6.6**. Hence, it could be possible to use the hexagonal array for guiding slow sound ASWs at those specific frequencies ( $f \sim 0.99f_D$ ) where loss is decreased, whilst group velocity is quite low. The honeycomb lattice can also be used for similar applications, since at frequency around  $0.98f_D$  losses decrease whilst being much lower than the those of the hexagonal sample. However, group velocity is larger at those frequencies for the honeycomb sample, implying that there is difficulty in simultaneously achieving slowness and low losses.

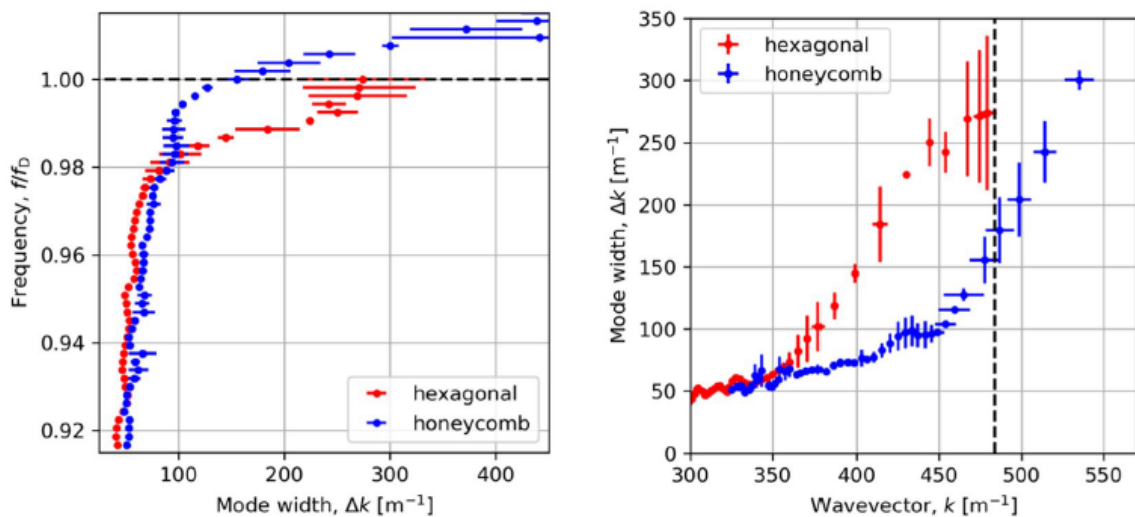


**Figure 6.11.** Analysis of acoustic surface wave loss as a function of frequency (left) and wavevector (right) for mode propagating in the  $\Gamma$  to  $K$  plane for honeycomb and hexagonal lattices. Data points are the mean values from the fit of forward and backward travel modes; error bars span the difference in fit values.

## 6.7 Conclusions

In summary, Fourier analysis of the acoustic signals in time ( $t$ ) and space ( $x, y$ ) was used to obtain the full dispersion relation ( $k_x, k_y, f$ ) and pressure field of the surface waves measured close to the surface of a honeycomb and hexagonal hole array. A short length acoustic pulse was used to account for reflections and a Hanning window with shape parameter  $a=0.5$  was

used to account for spectral leakage. However, a short length pulse gives rise to low frequency resolution and the “zero padding” signal processing technique was used to solve this problem. The maximum frequency that can be captured accurately in time signal analysis is dependent on the sampling rate, the maximum wavevector is dependent on the scan step size and the momentum-space resolution of the experiment is limited by the scan length.

For the honeycomb array, experimental results show that (for the lowest order cavity resonance) two acoustic surface modes exist, where at the  $K$  point they exhibit a Dirac point, and at the  $M$  point a band gap is seen. Numerical simulations were performed that show close agreement with the data obtained experimentally, confirming the Dirac point at  $K$  and a band gap at the  $M$  point. Moreover, it is shown that for the honeycomb sample the losses increase with increasing momentum along the  $\Gamma$ - $K$  direction, reflecting the propagation of acoustic surface waves with diminishing group velocity. The measured dispersion relation in the  $\Gamma$ - $K$  direction and in the isofrequency data, shows the excitation and detection of surface modes is dependent on the source conditions and that the mode symmetry can determine whether it is observable in the first Brillouin zone; in our measurement this manifested itself in the absence of the upper branch in the  $\Gamma$ - $K$  direction in the first Brillouin zone, and may be the reason for partial resolution of the same mode in the previously reported measurements of acoustic graphene [7]. These results demonstrate that the acoustic metamaterials provide an exciting platform for the exploration of fundamental physical phenomenon, such as Dirac dispersions. In addition, the numerical and experimental techniques could also be used to design acoustic metamaterials for slow sound related applications, as discussed in Chapter 5.

## CHAPTER 7

### Numerical investigation of metasurfaces comprising spiral shaped local resonators for SAWs

#### 7.1 Introduction

In Chapter 6, modes termed as acoustic surface waves (ASWs), were observed in the air above perforated aluminium samples. These modes are trapped because they have too much momentum to radiate into free space. Similarly, the surface acoustic waves (SAWs) discussed in the present chapter are also trapped but the medium in which this phenomenon occurs is lithium niobate, a hard crystalline solid, not air. Lithium niobate is one of the most important, and common, materials used in SAW devices due to its very strong piezoelectricity as already discussed in section 2.2.2 of Chapter 2. The interaction of an incoming Rayleigh SAW with resonant structures patterned on the lithium niobate substrate will be explored in the present chapter. The trapped SAW decays exponentially with depth into lithium niobate and the decay of the displacement amplitude will be referred to as confinement of acoustic energy. The confinement of acoustic energy has attracted much attention in the recent years since it allows the realisation of waveguides and cavities .

Apart from the confinement of acoustic energy, the interaction of a Rayleigh wave with resonant structures patterned on a semi-infinite medium [5], [102] is very promising for various technological applications due to the ability to create bandgaps, prohibiting propagation at specific frequencies, for SAW devices. In this Chapter, we computationally investigate the dispersion relation of a metasurface structure, designed to control SAWs, consisting of a void/lithium niobate phononic crystal atop a lithium niobate substrate. Attention is drawn at specific frequency regions where SAW modes are absent, the so called bandgap regions. A distinction between Bragg bandgaps and locally resonant bandgaps is given in the first section, where both types of bandgaps are defined. Next, the geometry of the void wall is described via the illustration of the unit cell used in the FEM model. The details of the numerical model are also given. Next, a thorough dispersion and transmission analysis is presented followed by a comparison between dispersion and transmission results. Dispersion relations and displacement fields for a novel structure are compared to the results of a previously reported

annular hole structure [5]. Specifically, the effect of changing the resonator's volume and shape on the confinement of acoustic energy, on the creation of bandgaps, and on the bandwidth of existing bandgaps are discussed. Finally, it is shown that an interesting feature; negative group velocity, appears in the dispersion curve for the novel structure which arises simply by increasing the resonator's depth.

## 7.2 Bragg gaps and locally resonant band gaps

Bandgap formation for elastic waves in 2D systems consisting of two composite materials, the host and the periodic structure, is dependent on both the velocity ratio and the filling ratio between the constituent materials in the case of Bragg bandgaps [101]. These Bragg gaps have centre frequencies corresponding to wavelengths up to two times the spatial period of the crystal. Recently investigated locally resonant band gaps, on the other hand, are typically centred at wavelengths at least two times larger than the spatial period of the crystal, and hence can achieve much lower frequency gaps compared to Bragg gap structures. The lattice constant used in the present chapter is  $a = 10.9 \mu\text{m}$  and we observe bandgaps at SAW wavelengths down to  $\lambda_{SAW} = 49.5 \mu\text{m}$ , meaning  $\lambda_{SAW} \gg 2a$ , which is made possible by the locally resonant bandgap. Realizations of such subwavelength bandgaps include SAW devices constituted of cylindrical dots deposited on a thin homogeneous plate [130], pillars [131] steel cubes, [132], or conical voids in lithium niobate [5], a structure which is referred to as annular hole structure and its dispersion relation has been illustrated in Figure 5.10, Chapter 5.

## 7.3 Void wall geometry

The void wall is of an Archimedean spiral shape and the spiral microgrooves shown in **Figure 7.1(a)** will be referred to as spiral resonators. A finite element (FE) model of the unit cell of width  $10.9 \mu\text{m}$  and depth  $10.9 \mu\text{m}$ , as shown in **Figure 7.1 (a)**, was developed in COMSOL® with a perfectly matched layer (PML) placed at the bottom region to avoid wave reflection. The top face of the unit cell is stress-free to allow bulk shear and longitudinal modes to couple and generate Rayleigh waves. The bottom face of the unit cell is constrained with a boundary

condition imposing zero displacement. The spiral-like resonator, whose details are shown in **Figure 7.1(b)**, is a  $6.4 \mu\text{m}$  thickness void, atop a lithium niobate substrate. The triangular cross section with the  $xz$  plane is shown in **Figure 7.1(d)**. Bloch–Floquet periodic boundary conditions are imposed at opposite sides of the square unit cell and a parametric sweep of wavevectors allows for the dispersion relation along the irreducible Brillouin zone shown in **Figure 7.1(c)**. Note that the model assumes that there is no loss within the lithium niobate.

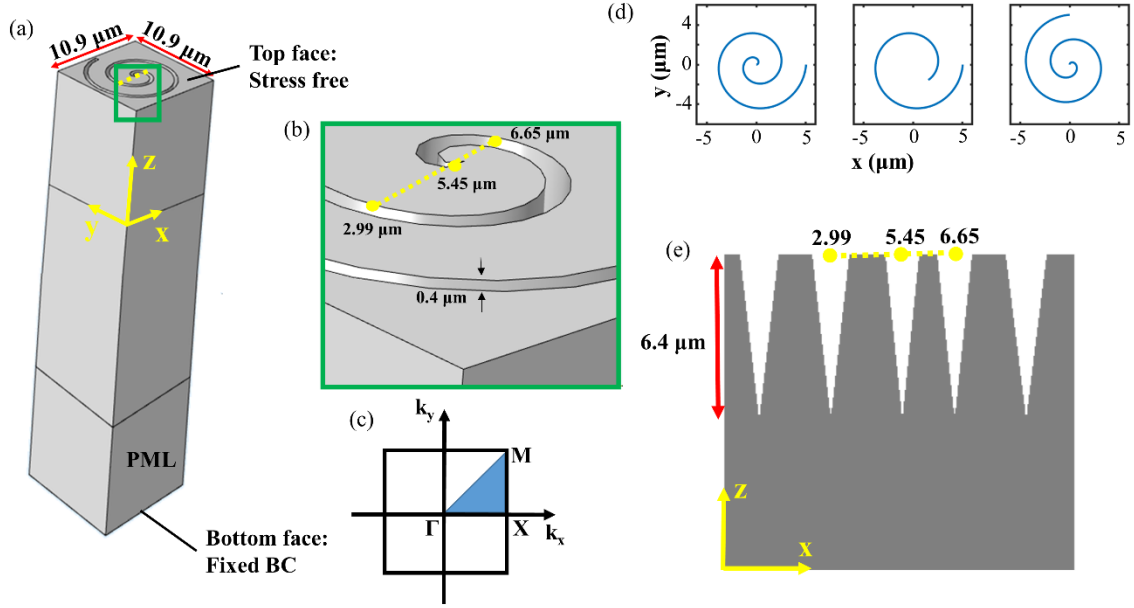


**Figure 7.1.** (a) Schematic of the unit cell model. (b) Magnification in green frame shows details of the top face of the unit cell. Yellow dashed lines are parallel to the  $x$ -axis connecting the centres of the voids. The central void's coordinates are  $(x_c, y_c) = (5.45 \mu\text{m}, 5.45 \mu\text{m})$ . (c) Blue triangle denotes the irreducible Brillouin zone of the square lattice.  $\Gamma X = XM = \frac{\pi}{\alpha}$ .  $\Gamma M = \sqrt{2} \frac{\pi}{\alpha}$ , where  $\alpha = 10.9 \mu\text{m}$ , is the lattice constant. (d) (d) Left panel: Spiral-I appearing in Figure 4 in the manuscript. Its parametric equation is  $x(t) = 0.4t \cos t [\mu\text{m}]$ ,  $y(t) = 0.4t \sin t [\mu\text{m}]$ ,  $0 \leq t \leq 4\pi$ . Middle panel: Spiral-II appearing in Figure 2, Figure 4 and Figure 5. Its parametric equation is  $x(t) = 0.4t \cos t [\mu\text{m}]$ ,  $y(t) = 0.4t \sin t [\mu\text{m}]$ ,  $\frac{7\pi}{4} \leq t \leq 4\pi$ . Right panel: Spiral-I with an inversed direction sweep, appearing in Figure 1, Figure 2 and Figure 6 in the manuscript. Its parametric equation is  $x(t) = 0.4t \cos t [\mu\text{m}]$ ,  $y(t) = 0.4t \sin t [\mu\text{m}]$ ,  $x'(t) = y(t)$ ,  $y'(t) = x(t)$ ,  $0 \leq t \leq 4\pi$ . (e) Projection of  $xz$ -plane with the  $y$ -coordinate fixed at  $y = 5.45 \mu\text{m}$  (i.e. in the middle of the unit cell), on the  $xz$ -plane at  $y = 0 \mu\text{m}$ . The voids are depicted

in white and the lithium niobate substrate is shown in grey colour. The yellow dots mark the centre of the voids, also shown in (b).

#### 7.4 Dispersion analysis

**Figure 7.2** contains the dispersion relations and displacement profiles of three different metasurfaces, previously investigated annular holes and two types of spiral resonators, Spiral-I (as shown in figure 1) and Spiral-II which has fewer spiral turns. In **Figure 7.2(a)** the dispersion relation for the spiral-like structure Spiral-I, blue dots, indicates that the number of guided modes is increased compared to the guided modes supported in the previously investigated annular hole structure, red dots. Both structures are of the same height and in-plane width, as shown in the first column of **Figure 7.2(b)**, where the cross section of each within the xz plane is shown. Although there are three high symmetry directions in the reciprocal space, note that **Figure 7.2(a)** shows only the  $\Gamma X$  direction, as propagation in this direction is widely used in practice for lithium niobate devices.

The increase of guided modes is associated with the number of spiral turns as confirmed by the dispersion relation of a second structure, Spiral-II, the dispersion curve for which is shown in green dots in **Figure 7.2(a)**. In the selected frequency region (70 MHz - 130 MHz), the annular hole structure and the Spiral-II structure both exhibit 3 modes, whereas the Spiral-I structure, in which the number of spiral turns is increased, exhibits 5 modes. The rms displacement fields for the three structures at the three faces of the unit cell are shown in **Figures 7.2(b)**, (c) and (d). The rms displacement field is defined as  $\frac{1}{\sqrt{2}}\sqrt{A_x^2 + A_y^2 + A_z^2}$ , where  $A_x, A_y, A_z$  is the amplitude of the displacement field in the x,y,z direction respectively. Displacement fields are shown at frequencies in which the third higher mode intersects the Brillouin zone boundary in the  $\Gamma X$  direction (annotated in blue, red and green triangles in dispersion curves). It can be seen that surface displacement is more pronounced at the upper half of the Spiral-I resonator whereas the whole height of the annular holes resonator experiences significant displacement (**Figure 7.2(b)**). In other words, large dissipation of rms displacement fields takes place in the Spiral-I structure, as it is shown in **Figure 7.2(c)**. Dissipation of rms displacement fields is even larger for the Spiral-II structure, as shown in **Figure 7.2(d)**. We note that the dissipation of rms displacement fields is not associated with damping into other forms of energy and is significant for all the guided modes supported by the Spiral-II structure (results not shown here). Acoustic energy is confined to the upper half of the resonator height for Spiral-II, but

the displacement field intensity is decreased compared to the denser spiral since the interface area between the Rayleigh wave and the resonator is decreased. Therefore, coupling is weaker and the energy needed to guide the mode 3 is higher, hence the frequency of the third higher mode at the Brillouin zone border is 126 MHz.

Dissipation results from the geometric chirality which is the main structural difference between annular holes and Spiral-I / Spiral-II structures. It has been shown [105] that there is analogy between chiral electromagnetism and acoustic seismic waves introducing an imaginary component to the phase velocity of acoustic waves. Hence, the evanescent displacement field of the SAWs in the Spiral-I/Spiral-II structures is associated with the imaginary wavevector induced by chirality. Apart from reference [105], which describes the effect of the chiral factor on attenuation, the chiral factor has been associated with negative refractive index in [133], [134].

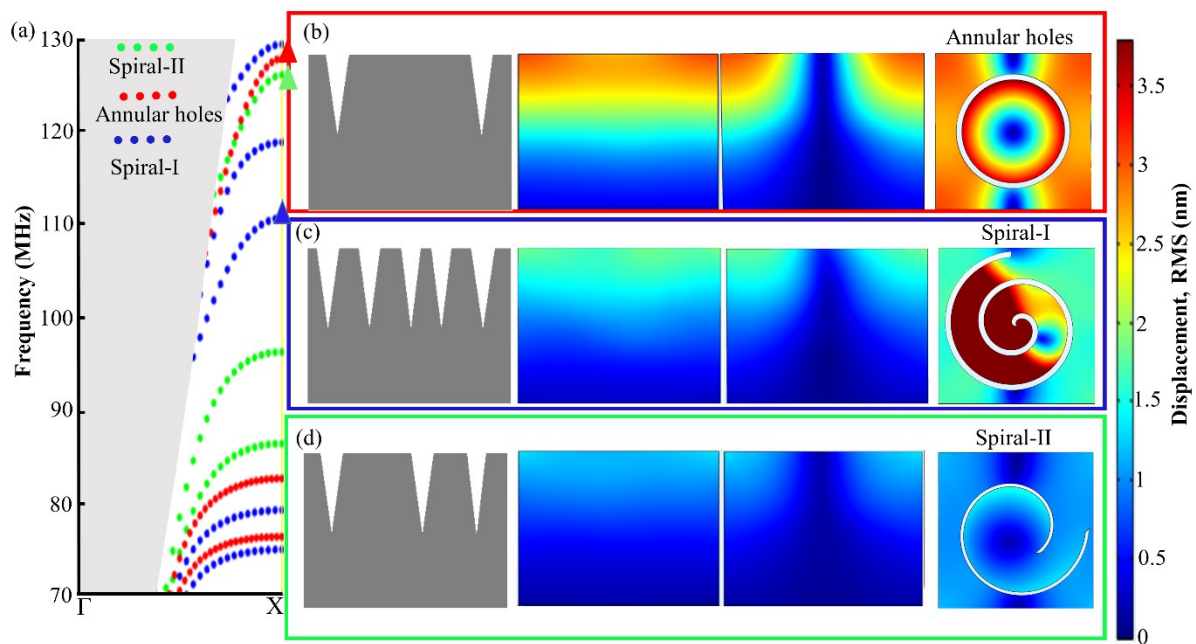


**Figure 7.2.** (a) Dispersion relations in the  $\Gamma X$  direction for the Spiral-II (green dots), annular holes (red dots) and Spiral-I (blue dots) structures. The area beyond the sound line is shaded in light grey. (b) From left to right : Projection of the annular hole structures to the  $xz$ -plane, displacement field profiles at X point and at  $f = 127.8$  MHz (denoted in red triangle), in the  $yz$ ,  $xz$  and  $xy$  planes. (c) From left to right: Projection of the Spiral-I structure to the  $xz$ -plane, displacement field profiles at X point and at  $f = 110.6$  MHz (denoted in blue triangle), in the  $yz$ ,  $xz$  and  $xy$  planes. (d) From left to right: Projection of the Spiral-II structure to the  $xz$ -plane,

displacement field profiles at X point and at  $f = 125.9$  MHz (denoted in green triangle), in the  $yz$ ,  $xz$  and  $xy$  planes.

It is worth noting that the third higher mode of the annular hole structure almost coincides with the third higher mode of the Spiral-II structure for small magnitude wavevectors. However, for larger wavevector magnitudes the third higher mode for the Spiral-II structure diverges towards lower frequencies. The rms displacement fields showing the top face of the unit cell (right panels in **Figures 7.2** (b), (c) and (d)) reveal that displacement fields in the centre of the unit cell are smaller compared to the displacement field at the unit cell edges for all three structures. This third higher mode in frequency is referred to as anti-resonant mode. Except for bringing the frequency of the anti-resonant mode down, chirality also affects the group velocity of the anti-resonant modes as shown in **Figure 7.3**. The group velocity of the anti-resonant modes for the annular hole, Spiral-I and Spiral-II structures is shown by the red, blue and green solid lines respectively. The group velocities of the Spiral-II and Spiral-I structures are clearly lower than the group velocity of the annular hole structure for wavevectors in the range  $(2.1 \times 10^5 \text{ m}^{-1} - 2.75 \times 10^5 \text{ m}^{-1})$ . At  $k = 2.1 \times 10^5 \text{ m}^{-1}$ , the group velocities of the Spiral-I structure (1000m/s) and the Spiral-II structure (1200 m/s) are 43% and 32% lower than the annular hole structure group velocity (1780 m/s) respectively. . At wavevectors approaching the first Brillouin zone border, the anti-resonant mode of the Spiral-I structure has a very slow group velocity (95 m/s) compared to the Spiral-II and annular hole modes (230 m/s).

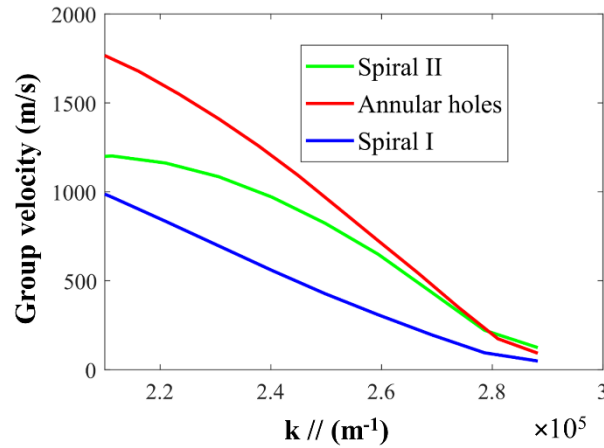


**Figure 7.3.** Group velocity versus wavevector for the anti-resonant mode of i) the Spiral-II structure (green solid line), ii) the annular holes structure (red solid line) and iii) the Spiral-I structure (blue solid line).

### 7.5 Transmission analysis

Transmission spectrums were obtained using the COMSOL® frequency domain model, as shown schematically in **Figure 7.4(a)**. An interdigital transducer (IDT) defined on the surface of the lithium niobate substrate is used to excite SAWs. The displacement field profile of the IDT source is minimal in the light blue regions. The substrate is surrounded by perfectly matched layers (PMLs). Zoomed inserts of the 3 different metasurface structures investigated in separate computational models are highlighted in dashed boxes. The substrate length,  $L$ , is scaled so that the distances between the metasurface and the other domain features are always the same integer values of  $\lambda_{SAW}$ . This was done to maximise computational resources for any given frequency.

In **Figure 7.4(b)** the calculated transmission spectrum of the Spiral-I and Spiral-II structures is shown by blue and green solid lines respectively. For comparison, the transmission spectrum of the previously reported annular hole structure of width  $2 \mu m$  is also shown by the red solid line. The structural parameter width is denoted in black arrows in **Figure 7.1(b)**. The  $0.4 \mu m$  wide Spiral-I structure exhibits a transmission minimum at about 80 MHz whereas the annular

hole structure exhibits a transmission minimum at 90 MHz. This demonstrates that the bandgap can be shifted to lower frequencies without the need to increase the size of the unit cell, making the realisation of RF based PnC filters and other components, easier and more cost-effective. The corresponding acoustic wavelength at the transmission minimum is  $4.5\alpha$  for the Spiral-I, and  $4\alpha$  for the annular hole, where  $\alpha=10.9\mu\text{m}$  is the lattice constant, meaning that the Spiral-I structure is deeply subwavelength at the bandgap frequency region. Moreover, a second transmission minimum is shown at a frequency of 130 MHz for the Spiral-I structure which corresponds to a wavelength of  $2.7\alpha$ . This is of interest in the realisation of stop band filters. The maximum bandgap attenuation for the Spiral-II structures occurs at 83MHz, and the bandgap attenuation in this case is significant for a wider frequency range compared to the other structures. The attenuation bandwidth can be tuned by controlling the eigenmodes's coupling to the Rayleigh wave (see section 3.3).

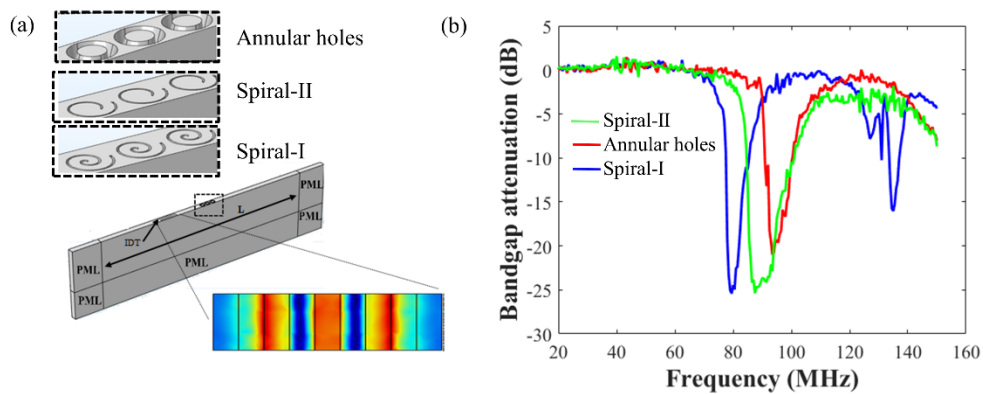


**Figure 7.4.** (a) Frequency domain geometry schematic showing the SAW excitation source and the metasurface on top of lithium niobate substrate surrounded by perfectly matched layers. Bottom inset shows the displacement profile field in the area of the IDT transducer. Dashed boxes zoom in the area occupied by the local resonators. Note that 3 spiral/annular hole elements were used (b) Transmission spectrum for annular holes (red), Spiral-I (blue) and Spiral-II (green) structures.

## 7.6 Dispersion/Transmission comparison

It is well known that acoustic waves incident on PnCs cannot excite all the modes predicted in theory or in computational models due to the modes' field profiles [135]. In order to understand which of the modes can be excited using the IDT SAW source shown in section 3.2, band diagrams are plotted alongside calculated transmission on a common frequency axis in **Figure 7.5**. It is clear that for the annular hole structure, mode B is highly attenuated since at that frequency the bandgap attenuation is -20 dB whereas for the spiral-II structure, mode A is highly attenuated, with the bandgap attenuation reaching the value of -25 dB. Observation of the above-mentioned modes displacement fields, shown in the middle panel of **Figure 7.5** and comparison to the source's displacement field, shown in **Figure 7.4** reveals that there is no correlation between the displacements field patterns of the source and the eigenmodes of the resonators. However, modes B and C in the Spiral-II structure and modes A and C in the annular holes structure show one common feature in their rms displacement fields; small rms displacement fields in the centre of the unit cell and in the area outside the resonator, and large displacement fields at the unit cell edges. The smaller bandgap attenuation values for these modes can be explained by considering again the stripe-like displacement field pattern of the source, the larger the area of the unit cell that the eigenmode's displacement field matches the source's displacement field, the larger the coupling of the eigenmode to the incident Rayleigh wave, and hence the smaller the bandgap attenuation. This is confirmed by observing that bandgap attenuation for anti-resonant modes (C modes) is around 0dB, whereas for mode B in the Spiral-II structure, the attenuation is significantly larger, around -15 dB. Comparison of the C eigenmodes's fields to the source indicates higher spatial correlation compared to that between the displacement field of Spiral-II B mode and the source. Moreover, comparison of the displacement fields for mode A in the Spiral-II and annular holes structure indicate that the wider bandgap shown in the transmission spectrum for Spiral-II structure results from chirality. There are multiple phase changes due to multiple reflections of the incident wave at the spiral resonator and the emergent displacement field decouples from the source, which results in increased bandgap attenuation at that frequency.

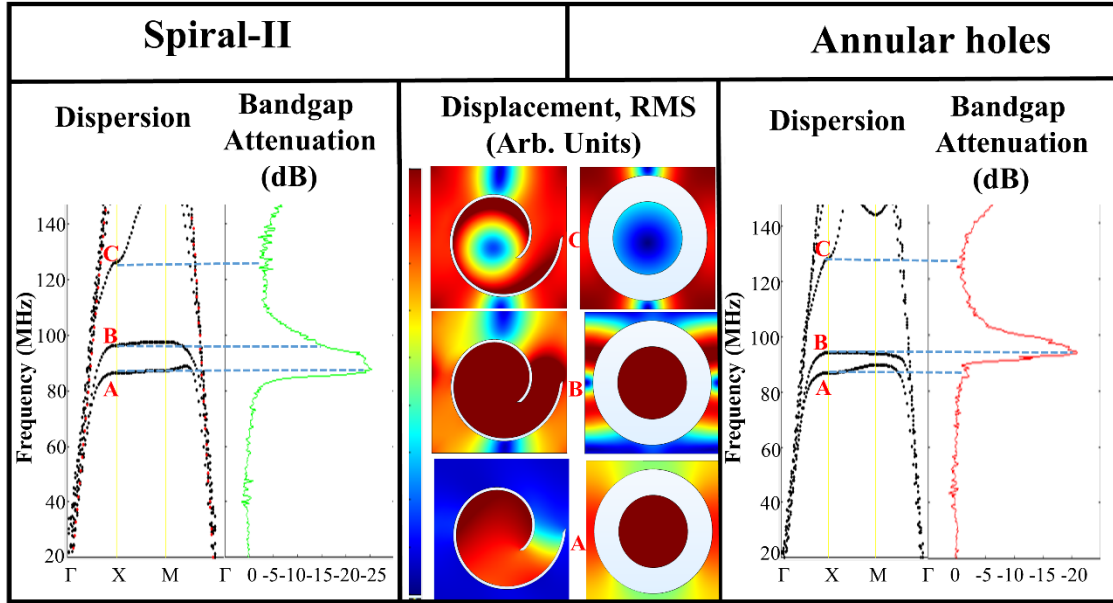


**Figure 7.5.** From left to right: Dispersion curve, bandgap attenuation and rms displacement fields for the Spiral-II structure. Rms displacement fields, dispersion curve and bandgap attenuation for the annular holes structure. A, B, and C annotate the frequency for which displacement rms fields are plotted. The magnitude of momentum in the  $\Gamma X$  direction at A, B and C points equals  $2.88 \times 10^5 m^{-1}$ .

### 7.7 Negative group velocity

**Figure 7.6(a)** shows the calculated dispersion curve for the Spiral-I structure, where the height of the spiral has been increased from  $6.4 \mu m$  to  $7.8 \mu m$ , with all remaining structural characteristics unchanged. Apart from one additional mode appearing in the frequency range [0 - 140 MHz] compared to the shallower Spiral-I structure, two negative group velocity modes emerge, marked with solid green lines in **Figure 7.6 (a)**. These modes are also shown magnified in the inset of **Figure 7.6 (c)**. The metasurface can therefore convey Rayleigh waves with group velocity anti-parallel to phase advancement. To our knowledge this phenomenon has not been reported for square arrays of chiral metasurfaces supporting SAWs, although the existence of negative group velocity SAW modes in thin film structures has been reported in [136]. The points at which the negative group velocity modes intersect the first Brillouin zone at the  $\Gamma X$  direction are denoted by letters A and B. The calculated rms displacement for these modes is shown in **Figure 7.6(b)**. As discussed previously, increased coupling of the source's

displacement field profiles to the eigenmodes's fields profiles results in small bandgap attenuation and hence large transmission. It follows that in order to increase transmission of the predicted negative group velocity SAWs, the incident Rayleigh wave displacement field should match the fields shown in **Figure 7.6(b)**. This may be achievable using a more sophisticated design for the IDT. Different arrangements of IDTs on  $128^\circ$  rotated Y-cut LiNbO<sub>3</sub> substrate have been shown to generate different patterns of travelling SAWs [137]. Modes A and B have also comparable displacement field profiles, meaning that by appropriate mode matching, negative group velocity modes around 118MHz and 153MHz, could be excited. Mode B is significantly slower compared to mode A at wavevector range ( $2.5 \times 10^5 m^{-1} - 2.88 \times 10^5 m^{-1}$ ) along  $\Gamma X$  direction, as shown in **Figure 7.6(c)**, indicating that a slow negative group velocity SAW mode could be realized at excitation frequency around 150 MHz.

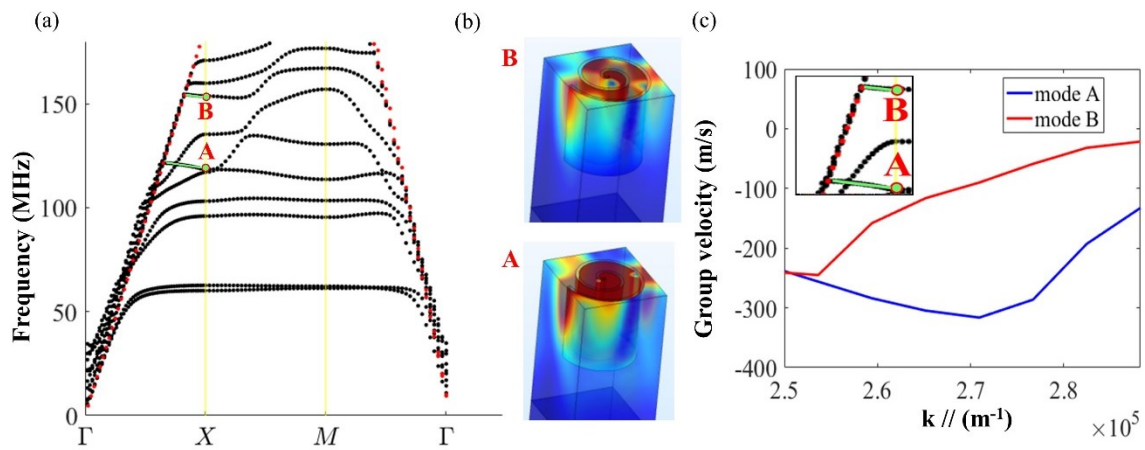


**Figure 7.6.** (a) Dispersion relation for a spiral structure of depth  $h=7.8 \mu m$  and width  $w=0.4 \mu m$ . A and B denote the intersection of negative group velocity modes (green solid lines) with the first Brillouin zone. Red dotted lines indicate the sound line.(b) Displacement, rms fields for modes A and B in a fraction of the unit cell volume. (c) Group velocity versus wavevector in the interval ( $2.5 \times 10^5 m^{-1} - 2.88 \times 10^5 m^{-1}$ ) along  $\Gamma X$  direction The inset shows a magnified part of the dispersion curve which includes the negative slope modes.Momentum for the  $\Gamma$  and X points in reciprocal space is  $0(m^{-1})$  and  $2.88 \times 10^5 (m^{-1})$  respectively.

## 7.8 Conclusions

In conclusion, the interaction of Rayleigh waves with novel spiral resonators has been investigated computationally. Enhanced acoustic energy confinement is demonstrated by the resonators volume being reduced. The dispersion relationships for arrays of such resonators were calculated and showed that they can be used to produce bandgaps for Rayleigh waves, but at lower frequencies than those can be achieved for other phononic crystals with the same unit cell size. The value of the attenuation at the bandgap frequency was extracted from simulations of the transmission through the resonators and was found to be extremely large (-25 dB), even for 3 spiral/annular hole elements used in COMSOL<sup>®</sup> simulations. The low-frequency bandgap was also to even lower frequency by changing the spiral density, suggesting that optimization of the structural parameters can lead to the design and fabrication of low-frequency stop band filters. We have shown that in the case that certain eigenmodes decouple from the source (see displacement field profile for Spiral II resonator, **Figure 7.5** and compare to displacement field profile of the source (**Figure 7.4**)), higher bandwidth gaps can be induced, hence a step towards controlling both bandgap central frequency and bandwidth has been made. In addition, negative slopes in the dispersion curve of the spiral structure indicate that a square array of spiral resonators, supports negative group velocity SAW modes, meaning that SAWs can propagate in an unconventional way throughout the device. The use of spiral structures therefore opens an exciting new pathway for the control and manipulation of surface acoustic waves.

## CHAPTER 8

### Conclusions and future directions

The characteristics of architected acoustic lattices have been studied in order to control the propagation of pressure waves in air, whereas architected elastic lattices were studied in order to control the propagation of elastic Rayleigh waves in a solid material, lithium niobate.

#### 8.1 Six-fold Symmetric Acoustic Surface Wave Metasurface

For the case of acoustic lattices, we compared dispersion relations between two different resonator configurations; a hexagonal and honeycomb configuration. The standing wave formation throughout the height of the resonators, which are in fact, rigid-walled cylindrical cavities and the end corrections to the resonant frequency were discussed, and related to an impedance mismatch between the inside of the resonator and the region just outside the resonator. Furthermore, another change in each cavity's resonance condition is induced by the periodicity of the lattice. There was good agreement between dispersion relations obtained from experiments and numerical analysis, with small discrepancies attributed to thermoviscous losses. Dirac cones are features that are usually observed in the context of solid state physics and imply many unconventional wave transports such as bulk insulation but edge conduction. The existence of Dirac cones in the simulated dispersion relations for the honeycomb lattice, but not the hexagonal, indicates that Dirac cones are the consequence of the specific honeycomb spatial patterning rather than a purely quantum phenomenon. The equations describing the acoustic honeycomb system (Bloch wave functions) can be cast into the exact form of Dirac Hamiltonian describing a spin one-half relativistic particle with zero mass. The dispersion relation for such a Hamiltonian is linear and the observation of linear dispersion relations in the honeycomb acoustic lattice is hence explained.

The experimental realisation of artificial acoustic graphene has many exciting perspectives, if the difficulty of coupling the source to the anti-symmetrical upper branch of the Dirac cone can be overcome. The anti-symmetrical acoustic pressure profile of the air unit cell has been confirmed by simulations, and hence appropriate manipulation of the pressure field profiles generated by a loudspeaker could lead to the experimental observation of the upper branch.

Another critical factor in detecting the upper frequency mode experimentally is the estimation of losses in the range of frequencies close to the Dirac frequency, i.e 16.5 kHz. We have shown that the attenuation of ASWs in that frequency range is significant by plotting the instantaneous pressure field for three different frequencies, close to the Dirac frequency. Additionally, the losses have been quantified by estimating the mode width and it has been confirmed that the losses increase as frequency approaches the Dirac frequency and as the wavevector approaches the Dirac point. Hence, it would be useful to re-design the experiment so that the operating frequency range is centred on a different frequency; in the ideal frequency regime there would be a weak dependence of loss on frequency. As a result, both the honeycomb and the hexagonal structures could be used for slow sound related applications.

Once the experimental observation of both Dirac branches touching one another is achieved, the next step would be to create a bandgap centred at the Dirac frequency which would allow the realization of new insulating phases of matter for the proposed acoustic system. At the interfaces between trivial and non-trivial topological insulators edge states could emerge as in references [138], [139]. However, the proposed acoustic system of hole resonators is easier to fabricate compared to the acoustic systems discussed on those references. Topological edge states are an important steppingstone to the experimental realization of topologically protected wave guides and thereby open up a new path for the design of metamaterials.

In contrast to artificial acoustic graphene, which is a two-band system, the hexagonal lattice is a one band system. The different number of states per momentum in the first Brillouin zone can be explained by considering the acoustic system's electronic counterpart, graphene. Graphene has 2 orbitals per unit cell (one  $p_z$  orbital per atom and two atoms in the unit cell), and hence two species of massless Dirac fermions, one for each valley, sharing the same energy. Interestingly, the honeycomb lattice's pressure field profiles have shown great similarity to the so called  $p_x$  and  $p_y$  orbitals of atomic systems, confirming the aforementioned analogy. Extension of this study into more complex configurations comprising of more than two resonators per unit cell, whilst maintaining the honeycomb lattice geometry, could lead to the enhancement of the aforementioned interesting phenomena. An example of a metasurface comprising of six resonators per unit cell, is shown in **Figure 8.1**. It can be observed that the metasurface can be constructed by superposition of either hexagonal or rhombic unit cells. We expect that experimental measurements will reveal linearities and Dirac cones (degenerate states) in dispersion relations and that the Fourier amplitude will be enhanced compared to the honeycomb structure due to stronger coupling between resonators. An enhanced Fourier

intensity would lead to more efficient wave transport throughout the waveguide and the evanescent wave fields could be employed to carry the subwavelength features of an object. Hence, the device could be used in imaging and lensing applications. If degeneracy is lifted, and phase distributions or averaged energy fluxes (of the lifted degeneracy states) reveal that these states can be regarded as valley pseudospin states, a practical topological insulator could be fabricated for its efficacy to be compared to the pre-existing academic work on topological insulators [140], [141], [142]. The amplified Fourier intensity of the upper branch of the Dirac cone would also enhance negative refraction and cloaking phenomena. However, the trade-off between increased Fourier intensity and losses should also be investigated and cross compared to the original honeycomb metasurface.

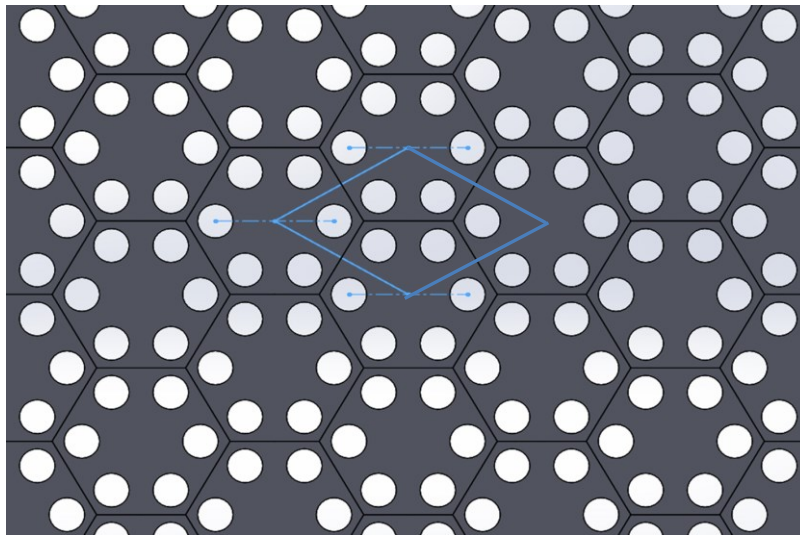


**Figure 8.1** Schematic of a metasurface comprising of six resonators per unit cell. The rhombic unit cell is marked in blue.

## 8.2 Novel Spiral Annular Hole Elastic Wave Metasurface

For the control of the propagation of Rayleigh waves, a type of surface acoustic wave (SAW), in a piezoelectric solid material a metamaterial consisted of spiral resonators was designed and characterized lithium niobate was chosen as the substrate material because it is characterised by a large piezoelectric coupling coefficient, which provides an efficient way to do the electro-acoustic transduction. Hence, the mechanical SAW is coupled to the electrical excitation of the IDT. For the SAW to propagate in a straight line (without curving) a  $128^\circ$  YX-  $\text{LiNbO}_3$  cut

has been selected in the COMSOL® simulations. Fascinating phenomena, such as sound confinement and negative group velocity were observed. To visualize the vibrational mode shapes of the solid square unit cell, the displacement profiles were superimposed as a heat map over its geometry for different frequencies and we have observed radial displacement field patterns extending over a shorter area in the solid compared to that of the annular hole structure. Furthermore, dispersion relation has shown that the guided modes of the spiral structure can be increased simply by increasing the number of spiral turns. These features could be exploited in applications where manipulation of the mechanical vibrations in micron scale phononic devices is desired. To achieve the desired bandgap centred around 80 MHz, a resonator array with 10.9  $\mu\text{m}$  pitch was used.

This new device of SAW metasurface outperforms a previously reported annular hole architecture in terms of the bandgap attenuation achieved at low frequencies. In acoustics, the improvement of low frequency sound absorption constitutes a real scientific challenge for the major issue of noise reduction. The attenuation has been achieved without increasing the size of the unit cell; it is the structural geometry of the system that induces the superior attenuation profile for Rayleigh waves. The realisation of radio frequency (RF) based PnC filters and other components is hence more cost-effective.

Unfortunately, due to the Covid-19 pandemic, devices containing the metasurface could not be fabricated or experimentally tested. Nevertheless, the high level of integratability of the device into complex electromechanical platforms makes the proposed device an excellent candidate for our future experimental endeavours. Specifically, apart from RF filters the phononic band gap structures can be easily integrated into wireless communication systems, acoustic signal processing devices and acousto-optical signal processing devices. It is well known that photonic crystals have been demonstrated in lithium niobate [143], [144], implying that if a structure exhibits both phononic and photonic bandgaps, simultaneous confinement of acoustic and optical waves could be achieved. It has been shown that confinement of acoustic waves is more intense for the case of the denser spiral since the interface area between the Rayleigh wave and the resonator is increased. The interface area could be perceived as the spring that conveys the travelling Rayleigh SAW wave through the area occupied by the voids, hence the lithium niobate substrate would act as mass. The excitation of the resonator is reflected on the displacement field intensity, which is increased for the case of dense spirals, since there are more “springs” to convey the energy. However, this is only a phenomenological approach and there are many unexplored mechanisms induced by the interaction of spiral resonators,

travelling Rayleigh SAW wave and the substrate. Therefore, a future perspective would be to compare the dispersion relation obtained from a mathematical spring mass model to the FEM calculated dispersion relations.

In lithium niobate, the speed of the Rayleigh SAW is of the order of 4000 m/s, which is five orders of magnitude slower than for light in vacuum. This means that there is ample time to manipulate a Rayleigh SAW signal, but it would be exceedingly difficult to do something similar with photon. The low speed of sound offers long delay times which makes it easier to record the IDT signal during its propagation to the acoustic channel, facilitating signal processing. An interesting research direction to pursue would be to record the IDT signal whilst placing diverse types of resonators in the acoustic channel. This would allow us to observe in near real time the resonator absorbing and emitting phonons and compare its coupling rate with theoretical predictions or experimental studies which use substrates other than lithium niobate. The comparison between different resonator geometries would lead to an optimized SAW device, exhibiting an increased coupling bandwidth with the Rayleigh SAW and hence a wide band gap.

A first step towards this direction has been made by building a non-periodic model, using COMSOL® software. Periodic boundary conditions, which were applied in the models described so far, are not relevant since we are only interested in investigating the excitation of a single or a small number of resonators; not an array of resonators. The excitation signal, or in other words the voltage applied to the metallic fingers of the IDT transducer, is a function of time and has been described in section 2.2.4.2. The simulation domain where the source is located is surrounded by PML and has already been shown in Chapter 4 (see Figure 4.7). The time step,  $dt = 0.1 \text{ ns}$ , satisfies the condition  $dt < dx/c$ , where  $dx = 15.5 \text{ }\mu\text{m}$  is the maximum mesh element size and  $c \sim 4000 \text{ m/s}$  is the speed of sound in lithium niobate. The future objective is to place resonators in the blank device of Figure 4.7 and explore the SAW coupling with the resonant system. The time domain model will allow us to measure the duration of the coupling which will be the first step towards device optimisation.

Except for mechanical resonators, SAWs can also interact with superconducting qubits at the quantum level and SAW phonons are proposed as a universal medium to couple remote quantum systems. A recent study by Bienfait et al. published in 2019 in Science [145] shows a way to entangle two superconducting qubits using sound which could allow researchers to transmit information instantly to space or make unhackable networks. In order to fabricate a

SAW device, similar to the one described in the present thesis, to operate in the quantum regime, the first step would be to increase the frequency of the IDT transducer to the order of GHz, which can be simply achieved by decreasing the spacing between the metallic fingers of the IDT.

Another interesting research direction could be the design of a piezoelectric topological insulator by exploring the Dirac-like feature observed in the dispersion relation of the SAW device in Chapter 7. Topological insulators have attracted wide interest in the community of acoustics owing to a variety of important applications, including acoustic-noise reduction, one-way sound propagation and acoustic communications. As already discussed (sections 8.1 and 5.4) topological edge states have been realised in acoustic metamaterials exhibiting Dirac-like features in their dispersion relations. However, up to date there are no studies (to our knowledge) showing topological edge states realised in metasurfaces lying on a piezoelectric substrate, similar to those described in Chapter 7. Dirac-like features have been observed in dispersion relations for square lattices of spiral resonators. The spiral metasurface could be re-designed with the aim of realising a piezoelectric topological waveguide. The small scale of such a device would be acceptable to mobile phone manufactures and if combined with sound attenuation properties it would open new opportunities for the design of advanced multifunctional metamaterials.

### **8.3 Outlook**

Acoustic metasurfaces not only provide an exciting test-bed for the study of fascinating fundamental physical phenomena, such as the realisation of graphene-like bandstructures, but have the potential to find application in a wide range of technological advances. In addition, although acoustic surface waves in air, and surface acoustic waves in a solid, have different characteristics, it is clear that metamaterial concepts developed for one can inspire new designs and approaches for the other.

## References

- [1] Veselago, Viktor G. "Electrodynamics of substances with simultaneously negative  $\epsilon$  and  $\mu$ ." *Usp. Fiz. Nauk* 92 (1967): 517.
- [2] Oudich, Mourad, et al. "Negative effective mass density of acoustic metamaterial plate decorated with low frequency resonant pillars." *Journal of Applied Physics* 116.18 (2014): 184504.
- [3] Zeighami, Farhad, Antonio Palermo, and Alessandro Marzani. "Rayleigh waves in locally resonant metamaterials." *International Journal of Mechanical Sciences* (2020): 106250.
- [4] Li, Pei, et al. "Effective medium theory of thin-plate acoustic metamaterials." *The Journal of the Acoustical Society of America* 135.4 (2014): 1844-1852.
- [5] Ash, B. J., et al. "A highly attenuating and frequency tailorable annular hole phononic crystal for surface acoustic waves." *Nature communications* 8.1 (2017): 1-7.
- [6] Lu, Jiuyang, et al. "Dirac cones in two-dimensional artificial crystals for classical waves." *Physical Review B* 89.13 (2014): 134302.
- [7] Torrent, Daniel, and José Sánchez-Dehesa. "Acoustic analogue of graphene: observation of Dirac cones in acoustic surface waves." *Physical review letters* 108.17 (2012): 174301.
- [8] COMSOL Multiphysics® v. 5.3a, www.comsol.com. COMSOL AB, Stockholm, Sweden.
- [9] Rayleigh, Lord. "On waves propagated along the plane surface of an elastic solid." *Proceedings of the London Mathematical Society* 1.1 (1885): 4-11.
- [10] LIDDELL, Henry George, and Robert SCOTT. "A Greek-English Lexicon. Henry Stuart Jones, rev." (2005).
- [11] Curie, Jacques, and Pierre Curie. "Développement par compression de l'électricité polaire dans les cristaux hémihédres à faces inclinées." *Bulletin de minéralogie* 3.4 (1880): 90-93.
- [12] Matthias, B. T., and J. P. Remeika. "Ferroelectricity in the ilmenite structure." *Physical Review* 76.12 (1949): 1886.
- [13] Weis, R. S., and T. K. Gaylord. "Lithium niobate: summary of physical properties and crystal structure." *Applied Physics A* 37.4 (1985): 191-203.

- [14] Sanna, Simone, and Wolf Gero Schmidt. "LiNbO<sub>3</sub> surfaces from a microscopic perspective." *Journal of Physics: Condensed Matter* 29.41 (2017): 413001.
- [15] Brits L. "Euler angles" [Online]. Available: [https://en.wikipedia.org/wiki/Euler\\_angle](https://en.wikipedia.org/wiki/Euler_angle) (2008) , accessed on February 2021
- [16] Slobodnik Jr, A. J., E. D. Conway, and R. T. Delmonico. "Microwave acoustics handbook, Vol. 1A, Surface wave velocities." *The Journal of the Acoustical Society of America* 56.4 (1974): 1307-1308.
- [17] White, R. M., and F. W. Voltmer. "Direct piezoelectric coupling to surface elastic waves." *Applied physics letters* 7.12 (1965): 314-316
- [18] Song, F., G. L. Huang, and G. K. Hu. "Online guided wave-based debonding detection in honeycomb sandwich structures." *Aiaa Journal* 50.2 (2012): 284-293.
- [19] Lim, C. W., and J. N. Reddy. "Built-up structural steel sections as seismic metamaterials for surface wave attenuation with low frequency wide bandgap in layered soil medium." *Engineering Structures* 188 (2019): 440-451.
- [20] Timoshenko, S., and J. N. Goodier. "Axially symmetrical stress distribution." *Theory of Elasticity* (1934): 372-384.
- [21] Langley, Philip. *Numerical modelling of the deformation of elastic material by the TLM method*. Diss. University of Hull, 1997.
- [22] Wang, Chi-Teh. "Applied Elasticity, McGraw-HillBook Company." (1953).
- [23] Lekhnitskii, S. G. "Theory of Elasticity of an Anisotropic Body [Translated from Russian]." (1981): 67-72
- [24] Royer, Daniel, and Eugene Dieulesaint. *Elastic waves in solids I: Free and guided propagation*. Springer Science & Business Media, 1999.
- [25] Salah, I. Ben, and MH Ben Ghazlen. "Rayleigh waves in piezoelectric material." *Physica Procedia* 2.3 (2009): 1377-1383.
- [26] Adler, Eric L. "SAW and pseudo-SAW properties using matrix methods." *IEEE transactions on ultrasonics, ferroelectrics, and frequency control* 41.6 (1994): 876-882.
- [27] Adler, Eric L. "Matrix methods applied to acoustic waves in multilayers." *IEEE Transactions on Ultrasonics, Ferroelectrics, and Frequency Control* 37.6 (1990): 485-490.

- [28] Ro, Ruyen, et al. "Propagation characteristics of surface acoustic waves in AlN/128° Y–X LiNbO<sub>3</sub> structures." *Japanese Journal of Applied Physics* 48.4R (2009): 041406.
- [29] Lemmon, Eric W., et al. "Thermodynamic properties of air and mixtures of nitrogen, argon, and oxygen from 60 to 2000 K at pressures to 2000 MPa." *Journal of physical and chemical reference data* 29.3 (2000): 331-385.
- [30] Pedlosky, Joseph. *Geophysical fluid dynamics*. Springer Science & Business Media, 2013.
- [31] Morse, Philip McCord, and K. Uno Ingard. *Theoretical acoustics*. Princeton university press, 1986.
- [32] Raichel, Daniel R. *The science and applications of acoustics*. Springer Science & Business Media, 2006.
- [33] Strutt, John William, and Baron Rayleigh. *The theory of sound*. Dover, 1945.
- [34] Cramer, Owen. "The variation of the specific heat ratio and the speed of sound in air with temperature, pressure, humidity, and CO<sub>2</sub> concentration." *The Journal of the Acoustical Society of America* 93.5 (1993): 2510-2516.
- [35] Cramer, Mark S. "Numerical estimates for the bulk viscosity of ideal gases." *Physics of fluids* 24.6 (2012): 066102.
- [36] Dukhin, Andrei S., and Philip J. Goetz. "Bulk viscosity and compressibility measurement using acoustic spectroscopy." *The Journal of chemical physics* 130.12 (2009): 124519.
- [37] Weston, D. E. "The theory of the propagation of plane sound waves in tubes." *Proceedings of the Physical Society. Section B* 66.8 (1953): 695.
- [38] Tijdeman, H. "On the propagation of sound waves in cylindrical tubes." *Journal of Sound and Vibration* 39.1 (1975): 1-33.
- [39] Kinsler, Lawrence E., et al. "Fundamentals of acoustics." *Fundamentals of Acoustics*, 4th Edition, by Lawrence E. Kinsler, Austin R. Frey, Alan B. Coppens, James V. Sanders, pp. 560. ISBN 0-471-84789-5. Wiley-VCH, December 1999. (1999): 560
- [40] Lighthill, Michael J., and James Lighthill. *Waves in fluids*. Cambridge university press, 2001.
- [41] <https://www.comsol.com/blogs/theory-of-thermoviscous-acoustics-thermal-and-viscous-losses/>, accessed on February 2021

- [42] Dickens, Paul, John Smith, and Joe Wolfe. "Improved precision in measurements of acoustic impedance spectra using resonance-free calibration loads and controlled error distribution." *The Journal of the Acoustical Society of America* 121.3 (2007): 1471-1481.
- [43] Chen, Jer-Ming, John Smith, and Joe Wolfe. "Saxophone acoustics: introducing a compendium of impedance and sound spectra." *Acoustics Australia* 37.1-19 (2009).
- [44] J. Wolfe (1999) 'Pipes and harmonics', at <http://www.phys.unsw.edu.au/jw/pipes.html>, accessed on February 2021
- [45] Wolfe, Joe, and John Smith. "Cutoff frequencies and cross fingerings in baroque, classical, and modern flutes." *The Journal of the Acoustical Society of America* 114.4 (2003): 2263-2272.
- [46] Benade, A. H. "Fundamentals of Musical Acoustics Oxford University Press." New York (1976).
- [47] Hernández, Gonzalo. Fabry-perot interferometers. No. 3. Cambridge University Press, 1988.
- [48] Kim, Youngmin, and Dean P. Neikirk. "Micromachined Fabry-Perot cavity pressure transducer." *IEEE Photonics Technology Letters* 7.12 (1995): 1471-1473.
- [49] Gardelli, Renato, Matteo Albani, and Filippo Capolino. "Array thinning by using antennas in a Fabry-Perot cavity for gain enhancement." *IEEE Transactions on Antennas and Propagation* 54.7 (2006): 1979-1990.
- [50] Santos, J. L., A. P. Leite, and David A. Jackson. "Optical fiber sensing with a low-finesse Fabry-Perot cavity." *Applied optics* 31.34 (1992): 7361-7366.
- [51] Meriwether, John W., and Andrew J. Gerrard. "Mesosphere inversion layers and stratosphere temperature enhancements." *Reviews of Geophysics* 42.3 (2004).
- [52] Allen, Monica T., et al. "Observation of electron coherence and Fabry-Perot standing waves at a graphene edge." *Nano letters* 17.12 (2017): 7380-7386.
- [53] <https://www.comsol.de/blogs/discretizing-the-weak-form-equations>
- [54] Lu, Y. Y., T. Belytschko, and Lu Gu. "A new implementation of the element free Galerkin method." *Computer methods in applied mechanics and engineering* 113.3-4 (1994): 397-414
- [55] COMSOL® Multiphysics User's Guide. 2012.

- [56] Taflove, Allen, and Susan C. Hagness. *Computational electrodynamics: the finite-difference time-domain method*. Artech house, 2005.
- [57] Chung, Jintai, and GM1223971 Hulbert. "A time integration algorithm for structural dynamics with improved numerical dissipation: the generalized- $\alpha$  method." (1993): 371-375.
- [58] Ash, B. "Locally Resonant Metamaterials for Surface acoustic Waves." Thesis submitted to the University of Exeter, 2018
- [59] Badreddine Assouar, M., and Mourad Oudich. "Dispersion curves of surface acoustic waves in a two-dimensional phononic crystal." *Applied Physics Letters* 99.12 (2011): 123505.
- [60] Lemoult, Fabrice, Mathias Fink, and Geoffroy Lerosey. "Acoustic resonators for far-field control of sound on a subwavelength scale." *Physical Review Letters* 107.6 (2011): 064301.
- [61] Zhu, Jie, et al. "A holey-structured metamaterial for acoustic deep-subwavelength imaging." *Nature physics* 7.1 (2011): 52-55.
- [62] Colombi, Andrea, et al. "Enhanced sensing and conversion of ultrasonic Rayleigh waves by elastic metasurfaces." *Scientific reports* 7.1 (2017): 1-9.
- [63] Colombi, Andrea, et al. "A seismic metamaterial: The resonant metawedge." *Scientific reports* 6.1 (2016): 1-6.
- [64] Palermo, Antonio, et al. "Engineered metabarrier as shield from seismic surface waves." *Scientific reports* 6.1 (2016): 1-10.
- [65] Donato, R. J. "Model experiments on surface waves." *The Journal of the Acoustical Society of America* 63.3 (1978): 700-703.
- [66] Stinson, Michael R., and Gilles A. Daigle. "Surface wave formation at an impedance discontinuity." *The Journal of the Acoustical Society of America* 102.6 (1997): 3269-3275.
- [67] Rienstra, Sjoerd W., and Avraham Hirschberg. "An introduction to acoustics." Eindhoven University of Technology 18 (2004): 19.
- [68] Ivanov-Shits, K. M., and F. V. Rozhin. "Investigation of surface waves in air." *Sov. Phys. Acoust* 5 (1959): 510-512
- [69] Feng, Shechao, and David Linton Johnson. "High-frequency acoustic properties of a fluid/porous solid interface. I. New surface mode." *The Journal of the Acoustical Society of America* 74.3 (1983): 906-914.

- [70] Attenborough, Keith, and Trevor L. Richards. "Solid particle motion induced by a point source above a poroelastic half-space." *The Journal of the Acoustical Society of America* 86.3 (1989): 1085-1092.
- [71] Wang, Xinlong. "Acoustical mechanism for the extraordinary sound transmission through subwavelength apertures." *Applied Physics Letters* 96.13 (2010): 134104.
- [72] Daigle, Gilles A., Michael R. Stinson, and David I. Havelock. "Experiments on surface waves over a model impedance plane using acoustical pulses." *The Journal of the Acoustical Society of America* 99.4 (1996): 1993-2005.
- [73] Christensen, Johan, et al. "Collimation of sound assisted by acoustic surface waves." *Nature Physics* 3.12 (2007): 851-852.
- [74] <https://ore.exeter.ac.uk/repository/handle/10871/29774>, accessed on February 2021
- [75] Zhang, Ze, and Sashi Satpathy. "Electromagnetic wave propagation in periodic structures: Bloch wave solution of Maxwell's equations." *Physical review letters* 65.21 (1990): 2650.
- [76] Zhang, Xiangdong, and Zhengyou Liu. "Extremal transmission and beating effect of acoustic waves in two-dimensional sonic crystals." *Physical review letters* 101.26 (2008): 264303.
- [77] Schrodinger, E. "Über die kraftefreie bewegung in der relativistischen quantenmechanik." *Sitzung Phys.-Math.* 31 (1930): 418.
- [78] Cserti, József, and Gyula Dávid. "Unified description of Zitterbewegung for spintronic, graphene, and superconducting systems." *Physical Review B* 74.17 (2006): 172305.
- [79] Weyl, Hermann. "Elektron und gravitation. I." *Zeitschrift für Physik* 56.5-6 (1929): 330-352.
- [80] Dirac, Paul Adrien Maurice. "The quantum theory of the electron." *Proceedings of the Royal Society of London. Series A, Containing Papers of a Mathematical and Physical Character* 117.778 (1928): 610-624.
- [81] Dirac, Paul Adrien Maurice. "A theory of electrons and protons." *Proceedings of the Royal Society of London. Series A, Containing papers of a mathematical and physical character* 126.801 (1930): 360-365.

- [82] Zhang, Yuanbo, et al. "Experimental observation of the quantum Hall effect and Berry's phase in graphene." *Nature* 438.7065 (2005): 201-204.
- [83] Collin, Robert E. *Field theory of guided waves*. Vol. 5. John Wiley & Sons, 1990.
- [84] Richoux, Olivier, V. Tournat, and T. Le Van Suu. "Acoustic wave dispersion in a one-dimensional lattice of nonlinear resonant scatterers." *Physical Review E* 75.2 (2007): 026615.
- [85] Yu, Gaokun, and Xinlong Wang. "Acoustical "transparency" induced by local resonance in Bragg bandgaps." *Journal of Applied Physics* 115.4 (2014): 044913.
- [86] Zhu, Jie, et al. "Acoustic rainbow trapping." *Scientific reports* 3.1 (2013): 1-6.
- [87] Romero-García, Vicente, et al. "Enhancement of sound in chirped sonic crystals." *Applied Physics Letters* 102.9 (2013): 091906.
- [88] Jacqmin, Thibaut, et al. "Direct observation of Dirac cones and a flatband in a honeycomb lattice for polaritons." *Physical review letters* 112.11 (2014): 116402.
- [89] Han, Dezhuang, et al. "Dirac spectra and edge states in honeycomb plasmonic lattices." *Physical review letters* 102.12 (2009): 123904.
- [90] Yannopapas, Vassilios, and Alexandros Vanakaras. "Dirac point in the photon dispersion relation of a negative/zero/positive-index plasmonic metamaterial." *Physical Review B* 84.4 (2011): 045128.
- [91] Weick, Guillaume, et al. "Dirac-like plasmons in honeycomb lattices of metallic nanoparticles." *Physical review letters* 110.10 (2013): 106801.
- [92] Torrent, Daniel, Didier Mayou, and José Sánchez-Dehesa. "Elastic analog of graphene: Dirac cones and edge states for flexural waves in thin plates." *Physical Review B* 87.11 (2013): 115143.
- [93] Zhong, Wei, and Xiangdong Zhang. "Acoustic analog of monolayer graphene and edge states." *Physics Letters A* 375.40 (2011): 3533-3536.
- [94] Dubois, Marc, et al. "Observation of acoustic Dirac-like cone and double zero refractive index." *Nature communications* 8.1 (2017): 1-6.
- [95] Chen, Ze-Guo, et al. "Accidental degeneracy of double Dirac cones in a phononic crystal." *Scientific reports* 4.1 (2014): 1-7.

- [96] Maznev, A. A., and O. B. Wright. "Optical generation of long-lived surface vibrations in a periodic microstructure." *Journal of Applied Physics* 105.12 (2009): 123530.
- [97] Brekhovskikh, L. M. "Propagation of surface Rayleigh waves along the uneven boundary of an elastic body." *Sov. Phys. Acoust* 5 (1960): 288.
- [98] Boechler, N., et al. "Interaction of a contact resonance of microspheres with surface acoustic waves." *Physical review letters* 111.3 (2013): 036103.
- [99] Johnson, Jeremy A., et al. "Phase-controlled, heterodyne laser-induced transient grating measurements of thermal transport properties in opaque material." *Journal of Applied Physics* 111.2 (2012): 023503.
- [100] Ewing WM, Jardetzky WS, and F. Press. "Elastic waves in layered media." (1957).
- [101] Sigalas, Michael, and Eleftherios N. Economou. "Band structure of elastic waves in two dimensional systems." *Solid state communications* 86.3 (1993): 141-143.
- [102] Khelif, Abdelkrim, et al. "Locally resonant surface acoustic wave band gaps in a two-dimensional phononic crystal of pillars on a surface." *Physical Review B* 81.21 (2010): 214303.
- [103] Movchan, A. B., and S. Guenneau. "Split-ring resonators and localized modes." *Physical Review B* 70.12 (2004): 125116.
- [104] Zhang, Siwen, Jiu Hui Wu, and Zhiping Hu. "Low-frequency locally resonant band-gaps in phononic crystal plates with periodic spiral resonators." *Journal of Applied Physics* 113.16 (2013): 163511.
- [105] Torres-Silva, Hector, and Diego Torres Cabezas. "Chiral seismic attenuation with acoustic metamaterials." (2013).
- [106] Wang, Xu, Dongxing Mao, and Yong Li. "Broadband acoustic skin cloak based on spiral metasurfaces." *Scientific reports* 7.1 (2017): 1-7.
- [107] Wu, Tsung-Tsong, et al. "Evidence of complete band gap and resonances in a plate with periodic stubbed surface." *Applied Physics Letters* 93.11 (2008): 111902.
- [108] Taleb, F., and S. Darbari. "Tunable Locally Resonant Surface-Acoustic-Waveguiding Behavior by Acoustoelectric Interaction in Zn O-Based Phononic Crystal." *Physical Review Applied* 11.2 (2019): 024030

- [109] Bo, Liu, et al. "Surface acoustic wave devices for sensor applications." *Journal of Semiconductors* 37.2 (2016): 021001.
- [110] Cai, Hua-Lin, et al. "A third-order mode high frequency biosensor with atomic resolution." *Biosensors and Bioelectronics* 71 (2015): 261-268.
- [111] Brûlé, Stéphane, et al. "Experiments on seismic metamaterials: molding surface waves." *Physical review letters* 112.13 (2014): 133901.
- [112] Maurel, Agnes, et al. "Conversion of Love waves in a forest of trees." *Physical Review B* 98.13 (2018): 134311.
- [113] Katsnelson, M. I. "Zitterbewegung, chirality, and minimal conductivity in graphene." *The European Physical Journal B-Condensed Matter and Complex Systems* 51.2 (2006): 157-160.
- [114] Diniz, Paulo SR, Marcello LR de Campos, and Andreas Antoniou. "Analysis of LMS-Newton adaptive filtering algorithms with variable convergence factor." *IEEE Transactions on Signal Processing* 43.3 (1995): 617-627.
- [115] Parker, Michael. *Digital Signal Processing 101: Everything you need to know to get started*. Newnes, 2017
- [116] Heinzl, Gerhard, Albrecht Rüdiger, and Roland Schilling. "Spectrum and spectral density estimation by the Discrete Fourier transform (DFT), including a comprehensive list of window functions and some new at-top windows." (2002).
- [117] Testa, Alfredo, Daniele Gallo, and Roberto Langella. "On the processing of harmonics and interharmonics: Using Hanning window in standard framework." *IEEE Transactions on Power Delivery* 19.1 (2004): 28-34.
- [118] <https://www.wavemetrics.com>, accessed on February 2021
- [119] Harris, Fredric J. "On the use of windows for harmonic analysis with the discrete Fourier transform." *Proceedings of the IEEE* 66.1 (1978): 51-83.
- [120] Stancik, Aaron L., and Eric B. Brauns. "A simple asymmetric lineshape for fitting infrared absorption spectra." *Vibrational Spectroscopy* 47.1 (2008): 66-69.
- [121] COMSOL Multiphysics<sup>®</sup> v. 5.3a, [www.comsol.com](http://www.comsol.com). COMSOL AB, Stockholm, Sweden.

- [122] Dautova, Yulia N., et al. "Gapless states in microwave artificial graphene." *Applied Physics Letters* 110.26 (2017): 261605.
- [123] Sakoda, Kazuaki. "Double Dirac cones in triangular-lattice metamaterials." *Optics express* 20.9 (2012): 9925-9939.
- [124] Li, Yan, et al. "Selection rule for Dirac-like points in two-dimensional dielectric photonic crystals." *Optics Express* 21.6 (2013): 7699-7711.
- [125] Wu, Long-Hua, and Xiao Hu. "Scheme for achieving a topological photonic crystal by using dielectric material." *Physical review letters* 114.22 (2015): 223901.
- [126] Zhang, Zhiwang, et al. "Topological creation of acoustic pseudospin multipoles in a flow-free symmetry-broken metamaterial lattice." *Physical review letters* 118.8 (2017): 084303.
- [127] Mei, Jun, et al. "First-principles study of Dirac and Dirac-like cones in phononic and photonic crystals." *Physical Review B* 86.3 (2012): 035141.
- [128] Schwan, Logan, et al. "Complex dispersion relation of surface acoustic waves at a lossy metasurface." *Applied Physics Letters* 110.5 (2017): 051902.
- [129] Theocharis, G., et al. "Limits of slow sound propagation and transparency in lossy, locally resonant periodic structures." *New Journal of Physics* 16.9 (2014): 093017.
- [130] Pennec, Yan, et al. "Low-frequency gaps in a phononic crystal constituted of cylindrical dots deposited on a thin homogeneous plate." *Physical Review B* 78.10 (2008): 104105.
- [131] Wu, Tsung-Tsong, et al. "Evidence of complete band gap and resonances in a plate with periodic stubbed surface." *Applied Physics Letters* 93.11 (2008): 111902.
- [132] Matlack, Kathryn H., et al. "Composite 3D-printed metastructures for low-frequency and broadband vibration absorption." *Proceedings of the National Academy of Sciences* 113.30 (2016): 8386-8390.
- [133] Plum, E., et al. "Metamaterial with negative index due to chirality." *Physical Review B* 79.3 (2009): 035407.
- [134] Zhou, Jiangfeng, et al. "Negative refractive index due to chirality." *Physical Review B* 79.12 (2009): 121104.
- [135] Sánchez-Pérez, Juan V., et al. "Sound attenuation by a two-dimensional array of rigid cylinders." *Physical Review Letters* 80.24 (1998): 5325.

- [136] Maznev, A. A., and A. G. Every. "Surface acoustic waves with negative group velocity in a thin film structure on silicon." *Applied Physics Letters* 95.1 (2009): 011903.
- [137] Weser, R., et al. "The complexity of surface acoustic wave fields used for microfluidic applications." *Ultrasonics* 106 (2020): 106160.
- [138] He, Cheng, et al. "Acoustic topological insulator and robust one-way sound transport." *Nature physics* 12.12 (2016): 1124-1129.
- [139] Yves, Simon, et al. "Topological acoustic polaritons: robust sound manipulation at the subwavelength scale." *New Journal of Physics* 19.7 (2017): 075003.
- [140] Xue, Haoran, et al. "Acoustic higher-order topological insulator on a kagome lattice." *Nature materials* 18.2 (2019): 108-112.
- [141] Ni, Xiang, et al. "Demonstration of a quantized acoustic octupole topological insulator." *Nature communications* 11.1 (2020): 1-7.
- [142] Chen, Yafeng, Fei Meng, and Xiaodong Huang. "Creating acoustic topological insulators through topology optimization." *Mechanical Systems and Signal Processing* 146 (2021): 107054.
- [143] Li, Mingxiao, et al. "Lithium niobate photonic-crystal electro-optic modulator." *Nature Communications* 11.1 (2020): 1-8.
- [144] Broderick, N. G. R., et al. "Hexagonally poled lithium niobate: a two-dimensional nonlinear photonic crystal." *Physical review letters* 84.19 (2000): 4345.
- [145] Bienfait, Audrey, et al. "Phonon-mediated quantum state transfer and remote qubit entanglement." *Science* 364.6438 (2019): 368-371.

